UTS UNIVERSITY OF TECHNOLOGY SYDNEY

An efficient PU-based approach to model quasi-brittle fracture and interfaces

by Seyedamir Latifaghili

Thesis submitted in fulfilment of the requirements for the degree of

Doctor of Philosophy

Under the supervision of Dr Nadarajah Gowripalan
Dr Mina Mortazavi
Dr Emre Erkmen
A/Professor Daniel Dias-da-Costa

University of Technology Sydney
Faculty of Engineering and Information Technology

December 2020

This page was intentionally left blank

Certificate of Original Authorship

I, Seyedamir Latifaghili declare that this thesis, is submitted in fulfilment of the requirements for the award of Doctor of Philosophy, in the Faculty of Engineering and Information Technology at the University of Technology Sydney.

This thesis is wholly my own work unless otherwise referenced or acknowledged. In addition, I certify that all information sources and literature used are indicated in the thesis.

This document has not been submitted for qualifications at any other academic institution.

This research is supported by the Australian Government Research Training Program.

Signature: Production Note:
Signature removed prior to publication.

Date: 7 December 2020

This page was intentionally left blank

To *Nazanin*

This page was intentionally left blank

Abstract

Partition of Unity (PU)-based approaches in Nonlinear Fracture Mechanics facilitated and improved the modelling of the fracture behaviour of quasi-brittle materials, such as mortar, concrete, masonry and rock. To this end, the discrete crack approach is assumed to localise the microcracks into the discontinuity surface represented by fictitious crack. The eXtended Finite Element Method (XFEM), as an advantageous modelling technique in the PU context, has been introduced and noticed in recent decades; however, its advantages have accompanied a number of difficulties such as ill-conditioned system, significant growth in the bandwidth of global matrix and inaccurate local solution around the crack path. Furthermore, the designation of reliable criterion, providing information about the strain localisation (i.e. crack initiation) and its orientation, can be considered another difficulty in using the discrete crack approaches.

Recently, various attempts have been made to overcome the difficulties in PU-based approaches. Regardless of all efforts, almost related to the improvement of convergence rate, numerical integration scheme and PU satisfaction, the difficulties of increasing additional degrees of freedom and inaccurate local solution at a discontinuity tip have gained little attention, and no efficient treatments have been presented.

In this study, a comparison between conventional cracking criteria and modified ones is drawn to obtain the appropriate criterion for different fracture modes. In addition, two innovative formulations are proposed: the XFEM with multi-layered Heaviside enrichment

and a polygonal enriched Partition of Unity Method. The main advantages are *i*) the cracking criterion can be employed in tensile and compressive states without any special consideration, *ii*) the bandwidth of global matrix and condition number decrease, and *iii*) the displacement jump and stress field are captured accurately.

The capability of the presented formulations is assessed by comparing them with standard XFEM. It is found that the formulation of XFEM with multi-layered Heaviside enrichment shows a remarkable agreement with standard XFEM locally and globally. The proposed formulation with polygonal enrichment overcomes the spurious behaviour of PU-based elements utilised in standard XFEM and opens the possibility of interface problems analysis. Furthermore, several benchmark tests concerning mode-I, mode-II and mixed-mode fracture are simulated, and the numerical results indicate remarkable similarities with the corresponding experimental data.

As a final result of this study, a robust and efficient numerical tool has been introduced to model the crack propagation and interfaces of quasi-brittle materials.

Acknowledgements

I would like to thank the people whose helps, supports and encouragement allowed me to accomplish the work presented in this thesis.

First, I would like to express Dr Nadarajah Gowripalan my deep sense of gratitude for comprehending my severe condition during this journey, supporting me wholeheartedly, believing in me and letting me follow my passion. I would also like to thank him for sharing his wide and invaluable experience with me generously. Without his substantial help, nothing could have been possible.

I appreciate the support of Dr Mina Mortazavi to allow me to meet my official commitment to the University of Technology Sydney.

I would like to thank Dr Emre Erkmen for helping me to take my initial and essential steps in this research field successfully. I am also grateful to him for implementing the Fortran code, helping me a lot since I started my study.

And Professor Daniel Dias-da-Costa, whose presence has profoundly influenced every second of this long journey. My sincere gratitude to him for giving me the chance to work with and learn from him. I have always admired his incredible generosity in sharing his knowledge; however, he kept mentioning, "There is no need to thank me!". He has always been there to help and guide me through various complications arisen, leading to the implementation of several innovative approaches. His passion, competence, care and professionalism have taught me how to avoid being just a knowledgeable person acting strictly with people, and

provide them with professional insight instead. I am proud of our friendship and collaboration in the last two years.

I am grateful for having had the chance of consulting with Professor M.E. Warkiani and Dr M. Asadnia. Their advice during this project changed the entire path of this study.

I appreciate the contribution of Milad Bybordiani to produce marvellous and brilliant ideas. Without our stimulating conversation during the process of writing, this work could not have been strong enough to be proud of.

To Habib Rasouli, Faraz Sadeghi, Mina Ghanbari, Mohsen Ranjbar, Atila Sarikaya, Ralf Gonzales, Sloan Trad, Zhiyu Luo and all colleagues that directly or indirectly provided a warm social environment, our friendly chats will never be forgotten.

Ali Paknahad has always been there for me from the very beginning while starting at UTS. His deep concern has helped me to overcome the most difficult moments in my life. I would like to stress his valuable advice and strong friendship that we have built throughout these years.

I owe a special thanks to Mehdi Aghayarzadeh for all early mornings that I met him in the silent room, giving me indefatigable energy that I am not alone at the school. For all serious talks during lunch, my enduring gratitude.

To my siblings, Payam for giving me the most special gift in the whole world; Pegah for introducing me to beautiful mind; and Poone for being there to help and support me however tough it has been, my eternal and heartfelt gratitude.

My parents, Maryam and Esa, have encouraged me all along the way to not give up at the awkward moments. My mother, with her patience and smile, made me feel true love. My

father, whose endurance and perseverance have taught me the courage to pursue my dreams until they come true. To them, my deepest gratitude.

Words are not enough to thank Nazanin, star of my life, who has always stood by me all the way, encouraged me to go beyond my limits. For comforting me in all disappointing moments, my profoundest gratitude. I thank her for bearing my little availability, her wholehearted and boundless support. Nothing could have ever been possible without her love. We have had a chance to grow up together and find the meaning of life, Love and only Love.

Amir Latif Aghili

This page was intentionally left blank

Contents

This page was intentionally left blank

List of Figures

List of Tables

This page was intentionally left blank

List of Algorithms

This page was intentionally left blank

List of Symbols

Latin symbols

$\mathbf{u}$	total displacement vector
$[\![\mathbf{u}]\!]$	jump vector
$\mathbb{R}$	Real Number
$\mathscr{H}$	Heaviside function
$\mathscr{P}^{(m)}$	polynomial of degree m
$\mathbf{A}$	standard assembly operator
b	width
c	cohesion
d	scalar damage
E	Young's modulus
f	function
h	characteristic element size
h	parameter defining the jump transmission to Ω^+ and Ω^-
i, j	finite element node
l	measure of significant distance around the tip
n	number of the finite element nodes
r	distance between the integration point and the tip

$\hat{\mathbf{u}}$	regular displacement field vector
τ	tangential stress vector
$\mathbf{a}$	total displacement vector at the nodes
$\mathbf{B}$	strain-nodal displacement matrix
$\mathbf{D}$	constitutive matrix
$\mathbf{f}$	vector of global nodal forces
$\mathbf{L}$	differential operator matrix
$\mathbf{L}$	differential operator matrix
$\mathbf{N}$	shape function matrix
$\mathbf{n}$	unit vector normal to a boundary
$\mathbf{P}$	external load
$\mathbf{R}$	transformation matrix
$\mathbf{s}$, $\mathbf{n}$	unit vectors tangent and orthogonal to the discontinuity composing the local frame
$\mathbf{T}$	discontinuity constitutive matrix
$\mathbf{t}$	traction vector
$\mathbf{w}$	nodal jump vector
$\mathbf{x}$	global coordinates of a material point
D_{sk}	shear stiffness for an advanced state of damage
f_c	compressive strength
f_t	tensile strength
G_F	fracture energy
G_{F_c}	compressive fracture energy
h_j	distance

h_s parameter defined by: $-\ln(D_{s\kappa}/D_{s\kappa_0})$

k_n, k_s normal and shear penalty parameters

l_a active length scale parameter

l_{ch} Hillerborg's characteristic length

s_j length

u_v vertical displacement

$\bar{\mathbf{b}}$ body forces vector

$\bar{\mathbf{N}}$ shape function matrix

$\bar{\mathbf{t}}$ natural forces vector

$\bar{\mathbf{u}}$ essential boundary conditions vector

$\hat{\mathbf{a}}$ regular displacement vector at the nodes

$\hat{\mathbf{f}}$ regular external vector force at the regular nodes

$\tilde{\mathbf{a}}$ enhanced displacement vector at the nodes

$\tilde{\mathbf{f}}$ enhanced external vector force at the regular nodes

$\mathbf{d}_i$ vector connecting discontinuity tip to integration points

$\mathbf{f}_{cond}$ condensed vector force at the nodes

$\mathbf{H}_{\Gamma_d}$ diagonal matrix containing the Heaviside function evaluated at each degree of freedom

$\mathbf{K}_d$ discontinuity stiffness matrix

$\mathbf{K}_{\hat{a}\hat{a}}$ bulk stiffness matrix

$\mathbf{K}_{\tilde{a}\hat{a}}, \mathbf{K}_{\hat{a}\tilde{a}}, \mathbf{K}_{\tilde{a}\tilde{a}}$ enhanced bulk stiffness matrices for the XFEM

$\mathbf{K}_{aa}$ stiffness matrix for the interface elements

$\mathbf{K}_{cond}$ condensed stiffness matrix

$\mathbf{T}^d$ damage stiffness matrix

$\mathbf{T}^e$ initial isotropic stiffness matrix

$\mathbf{x}_{dis}$ location of the discontinuity

Greek symbols

α history variable

$\bar{\lambda}$ offset ratio

β shear contribution parameter

$\delta(.)$ admissible or virtual variation of $(.)$

$\Delta(\cdot)$ change of $(\cdot)$

Γ boundary

κ scalar variable

λ active length

$\nabla(.)$ gradient of $(.)$

ν Poisson ratio

Ω elastic domain

ω weight coefficient

ϕ internal friction angle

$\Psi(\mathbf{x})$ function

ρ dead-weight

θ angle

α_i weight function

$\hat{\varepsilon}$ regular strain tensor

σ stress tensor

ε total strain tensor

δ_a Dirac's delta function at point a

δ_{Γ_d} Dirac's delta function along the surface Γ_d

η_L circle diameter

Γ_d discontinuity surface

Γ_t boundary with natural forces

Γ_u boundary with essential conditions

κ_0 scalar parameter denoting the beginning of the softening

$\delta(.)$ admissible or virtual variation of $(.)$

σ_{I} first principal stress

δ_i angle

γ_i angle

φ_i function

Indices

$(\cdot)^+$,$(\cdot)^-$ $(\cdot)$ at the Ω^+ and Ω^-

$(\cdot)^{\cdot}$ rate form of $(\cdot)$

$(\cdot)^s$ symmetric part of $(\cdot)^s$

$(\cdot)^T$ transpose of $(\cdot)$

$(\cdot)^{-1}$ inverse of $(\cdot)$

$(\cdot)_0$ initial value of $(\cdot)$

$(\cdot)_L$ L^{th} enrichment layer of $(\cdot)$

$(\cdot)_n$, $(\cdot)_s$ normal and shear components of $(\cdot)$

$(\cdot)_n$, $(\cdot)_s$, $(\cdot)_e q$ normal, tangential and equivalent components of $(\cdot)$

$(\cdot)_{el}$ elastic $(\cdot)$

$(.)^{elsL}$ $(.)$ belonging to the layer L

$(.)_{cond}$ Schur complement of $(.)$

Acronyms

BVP Boundary Value Problem

CMOD Crack Mouth Opening Displacement

CMSD Crack Mouth Sliding Displacement

DSDA Discrete Strong Discontinuity Approach

GFEM Generalised Finite Element Method

GSDA Generalised Strong Discontinuity Approach

LEFM Linear Elastic Finite Element

MLF Moving Least-Squares

NR Newton-Raphson

PU Partition of Unity

PUM Partition of Unity Method

SDA Strong Discontinuity Approach

XFEM eXtended Finite Element Method

CHAPTER 1

Introduction

The significance of the fracture behaviour of quasi-brittle materials such as concrete, mortar, rock and masonry lies in their widespread use in engineering. In recent decades, the failure of those materials has been studied extensively by means of computational mechanics. Fracture mechanics explains the discrete crack approach by lumping additional deformation into the displacement field to model the crack propagation. The non-linear behaviour before failure due to microcracking eventually leads to coalescence into a large fracture zone at the crack tip which violates the assumptions of traction-free crack borders in Linear Elastic Fracture Mechanics (Griffith, 1921; Irwin, 1997), and requires Nonlinear Fracture Mechanics considering a relationship between the traction and crack opening (Barenblatt, 1959; Dugdale, 1960).

The numerical simulations can be broadly grouped into two different approaches in terms of crack modelling in quasi-brittle materials: the smeared and the discrete approaches, which are introduced by Rashid (1968) and Ngo and Scordelis (1967), respectively. The smeared crack model where a cracked solid is assumed to be a continuum (Cervenka, 1985; Dias-da-Costa et al., 2018; Jendele et al., 2001; Rots et al., 1985), can be categorised into the rotating and fixed smeared crack models, has been shown to suffer some drawbacks including

the sensitivity of crack propagation to mesh edges directions (Alfaiate et al., 1997; Borst et al., 2004). Moreover, inappropriate explanation of the kinematics of the discontinuous displacement field in traditional smeared crack models leads to the spurious stress transferring across the cracks, resulting in stress locking (Arrea, 1981).

In the discrete approach, also known as the cohesive approach, the discontinuity is considered as a geometric entity localised in the displacement field and designated by fictitious crack. This approach simulates the initiation and propagation of dominant cracks based on basic assumptions, namely that: microcracking develops when the stress at the crack tip exceeds the tensile strength; microcracking localises in a zero surface of the discontinuity, assigned the role of strong discontinuity; the discontinuity evolves according to the traction-separation relationship; the bulk unloads because of the traction continuity condition (Dias-da-Costa et al., 2009). When a linear elastic relationship is adopted for the bulk, the discrete material law can be defined independently of the continuum (Alfaiate et al., 2003), which means that all non-linear behaviour is lumped at the discontinuity. In this case, no information can be retrieved about the process of strain localisation directly from the constitutive model of the bulk. In this stage, a crack initiation criterion assumes particular importance given that it needs to be introduced explicitly and, ideally, should also provide the direction of propagation, although it may not always be the case.

Mesh dependency is observed in the original form of the discrete approach because discontinuities are forced to propagate along the boundary of the elements. Some approaches proposed to reduce this dependency are *i*) remeshing algorithms, improving the results considerably by enabling the element boundaries to approximate the crack path (Arrea, 1981; Ingraffea

and Saouma, 1985; Ingraffea et al., 1984), however, other problems such as distorted finite elements and an increase of stiffness matrix bandwidth are raised; *ii*) meshless methods, where the cracks propagate arbitrarily without the need for mesh support (Belytschko et al., 1994, 1995; Lucy, 1977; Nguyen et al., 2008; Rabczuk et al., 2007a,b; Rabczuk and Belytschko, 2004; Wu and Fang, 2009). Nonetheless, the rational shape functions utilised in meshless methods, leading to costly integration and unsatisfied Kronecker delta property, render the computational cost of these approaches heavy and restrict their usage (Nguyen et al., 2008).

To embed the discontinuities within finite elements, two formulations have been explored: *i*) weak discontinuity, characterised by bounded, but discontinuous strain field with corresponding continuous displacement field (Jin et al., 2019; Ortiz et al., 1987; Sluys and Berends, 1998); and *ii*) strong discontinuity characterised by an unbounded strain field with corresponding discontinuous displacement field (Alfaiate et al., 2002; Dias-da-Costa et al., 2009; Dvorkin et al., 1990; Jirásek and Zimmermann, 2001; Larsson and Runesson, 1996; Linder and Armero, 2007b; Lotfi and Shing, 1995; Ohlsson and Olofsson, 1997; Oliver et al., 2004; Oliver, 1996; Oliver et al., 2003, 2012; Wells and Sluys, 2001b,c). Ortiz et al. (1987) presented a method to improve the performance of general classes of elements in problems with strain localisation. The information of the process of localisation obtained from the element level is used to prepare appropriate shape functions utilised in element interpolation, which reproduces localised deformation modes. Dvorkin et al. (1990) proposed a formulation covering the progressive localisation zone without remeshing. Wells and Sluys (2001a) introduced a formulation including continuous displacement jump across the element boundaries unlike the previous studies (Armero and Garikipati, 1996; Dvorkin et al., 1990; Klisinski

et al., 1991; Simo et al., 1993) and without any restriction on the type of finite element. Oliver et al. (2014) proposed a strain-injection and crack-path-field techniques to capture the crack propagation. Raina and Linder (2015) developed a framework for non-woven materials by homogenising the bulk response and Nikolić et al. (2018) proposed two different models for crack propagation in dynamic based on embedded strong discontinuities.

The eXtended Finite Element Method (XFEM), also known as the Generalised Finite Element Method (GFEM), is one of the methods utilised to model strong discontinuities (Jirásek and Belytschko, 2002). Conceptually, XFEM, as a special case of the Partition of Unity Method (PUM) (Babuška and Melenk, 1997; Chen et al., 2012; Duarte et al., 2000; Duarte and Oden, 1996a,b; Melenk and Babuška, 1996; Moës et al., 1999; Oden et al., 1998; Wells and Sluys, 2001a), utilises the partition of unity to define enrichment functions to better approximate the solution of the problems involving discontinuities (Aquino et al., 2009; Duarte and Kim, 2008). XFEM naturally resolves stress locking issues and non-continuous jumps across element boundaries. To this end, the total displacement field are decomposed into a regular continuous field and a discontinuous counterpart associated with the extra degrees of freedom. The additional degrees of freedom added globally to the system of equations assure a continuous jump along the discontinuity and the conformity of the solution.

It is noteworthy that the above-mentioned advantages are accompanied by a series of numerical issues. In the XFEM framework, the incorporation of enrichment functions into finite element basis renders the stiffness matrix ill-conditioned (Babuška and Banerjee, 2012; Fix et al., 1973; Menk and Bordas, 2011). However, significant effort has been devoted in the past decades to overcome the issues of ill-conditioned systems (Agathos et al., 2016; Béchet

et al., 2005; Loehnert, 2014; Zhang et al., 2020). On the other hand, XFEM cannot explicitly interpret the physical meaning of the additional degrees of freedom located at the standard element nodes instead of the crack ends (Dias-da-Costa et al., 2010). As a consequence, a straight discontinuity could become curved after mapping for integration purposes (Ventura, 2006). Simone (2004) related the spurious traction oscillation to the pathological couplings between degrees of freedom in widely-used elements in XFEM (Moës et al., 1999; Remmers et al., 2001; Simone et al., 2003; Wells and Sluys, 2001a), also called PU-based discontinuous elements, whereas unsatisfied moment equilibrium occurring at the interface of the element was considered as the main reason behind this phenomenon by Ahmed and Sluys (2013). Furthermore, the second layer of additional degrees of freedom added to the standard finite element doubles degrees of freedom of the parent element supporting a discontinuity, which leads to an increase of the total nodal unknowns during the crack propagation analysis. As a remedy, a two-scale solution procedure was developed in (Duarte and Kim, 2008; Kim et al., 2010; Pereira et al., 2012) considering a coarse mesh to discretise the global boundary value problem and a finer one for the region around the discontinuity (i.e. the local boundary value problem). The solution of the global problem is used to identify the Dirichlet boundary condition required for the smaller scale. Subsequently, the fine-scale solution is utilised to enrich the global space. Although the dimensions of the global problem remain constant in this approach, the small scale analysis is still subject to the progressive increase in size with crack propagation.

In the framework of XFEM, the possibility of including multiple cracks in one element was addressed in (Remmers et al., 2003), which could also be applied to complex phenomenon

such as crack branching in dynamic fracture (Remmers et al., 2008). Fries (2008) proposed a corrected XFEM addressing the problems caused by the elements whose nodes partially enriched. Zhu (2012) improved the enrichment functions used in conventional XFEM. Pourmodheji and Mashayekhi (2012) added continuum damage mechanics to XFEM to provide a model covering ductile crack growth. Chen et al. (2012) and Surendran et al. (2017) presented a strain smoothing procedure to obtain the ultra-accurate solution. Lagrange multiplier space has been adopted on the assembly of subdomains discretised by XFEM to solve the linear elasticity problems (Csati et al., 2020). Despite the fact that all of the previous studies improved different aspects of XFEM, two main difficulties have not been addressed: *i*) the increasing number of degrees of freedom; *ii*) the spurious behaviour in PU-based discontinuous elements (e.g. oscillations in the traction profile and displacement jump). In the former case, XFEM formulations require an additional computational cost as a result of increasing system dimension associated with crack propagation. This is solely related to the number of enhanced degrees of freedom that need to be added to the analysis with propagation. In the latter case, PU-based discontinuous elements show anomalous behaviours, leading to inaccurate calculation of displacement jump and consequent nodal values in interface problems, which deteriorate even further by using higher stiffness for their interfaces.

1.1 Objectives

The main focus of this thesis is the development of a robust numerical tool to improve the XFEM by alleviating three critical difficulties of this approach. To this end, the objectives of this work can be categorised as below:

- Develop a reliable approach for crack initiation and propagation in:
  - a robust strategy to predict crack propagation in quasi-brittle material in tensile and compressive states;
  - crack tracking criterion which is independent to adopted mesh, and parameter predefined by the user.
- Propose an efficient XFEM for fracture propagation by reducing:
  - enhanced degrees of freedom;
  - the condition number of the stiffness matrix;
  - computational cost in problems involving discontinuities.
- Present a revised XFEM formulation surmounting spurious behaviours of PU-based discontinuous elements to:
  - capture accurate displacement jump and stress field;
  - open the opportunity to analyse quasi-brittle interfaces;
  - assign the straight physical meaning to the additional degrees of freedom.

In order to obtain a robust approach for capturing the mixed-mode and compressive fractures of quasi-brittle materials, advantages and disadvantages of different cracking criteria should be taken into account. A formulation with multi-layered enrichment can decrease the enhanced degrees of freedom and consequent computational cost. The straight physical interpretation of additional degrees of freedom in proposed polygonal enriched Partition of Unity method develops a remarkable ability to be used for quasi-brittle material interfaces problems.

Validation is obtained from the comparison of numerical results with experimental data, utilising several benchmark tests in mode-I, mode-II and mixed-mode fracture. In order to emphasise the robustness of the developed formulation, four cracking criteria are chosen for comparison. Moreover, the results of the new formulation are compared to results obtained from standard XFEM, and the differences are explored.

1.2 Outline

This thesis is organised into six chapters. The first chapter presents a brief review of the research field, the objectives and the outline of the thesis. Chapter 2 presents the general framework of XFEM, including the kinematics of strong discontinuity, the variational formulation, discretisation and material models implemented in this study. In addition, the enrichment strategy and the performance of the partition of unity-based discontinuous elements, which are widely adopted in XFEM, are reviewed. In chapter 3, a thorough assessment of cracking criteria is conducted by means of several examples to reveal the particularities of each. Recommendations are made to select the appropriate crack initiation and propagation

criterion in mode I, mixed-mode and uniaxial compression state. Chapter 4 is devoted to the development of an efficient XFEM based on a local Heaviside function enrichment. Several examples, including experimental results, are computed and compared to standard XFEM to assess the accuracy of the proposed formulation. In chapter 5, the special enrichment function is introduced to avoid spurious oscillation in the PU-based discontinuous elements. The formulation and justification for utilising this class of enrichment function are discussed, and the robustness of the formulation is validated using benchmarks. Finally, in Chapter 6, the relevant conclusion of each chapter are summarised, and the final conclusions are drawn.

As a result of this thesis, a paper has been submitted in the journal cited in ISI Web Knowledge as:

Latifaghili, A., Gowripalan, N., Erkmen, E., Dias-da-Costa, D., 2020. A comparative study on simplified crack propagation criteria for quasi-brittle materials (*submitted*)

This page was intentionally left blank

CHAPTER 2

Literature review

In this chapter, a review of strong discontinuities and corresponding solution approach by XFEM as a robust framework is presented. First, in section 2.1, the kinematics of the strong discontinuity, the boundary-value problem in the strong form, and the corresponding weak form defined by variational formulations are addressed. Next, in section 2.2, a survey on discrete crack approach is presented. The necessity of crack initiation and propagation criterion is justified, where the link between bulk and discontinuities is clarified. Also, four damaged models are introduced. An overview of XFEM utilising the concept of the PU is given in section 2.3. The variational formulation and the discretisation adopted in the XFEM are summarised. Both numerical integration issues and nodal enrichment technique are briefly discussed, which clarifies the main drawbacks of XFEM. In section 2.4, PU-based discontinuous elements as the widely-used elements in XFEM are introduced. The computational issue concerning spurious behaviour of corresponding elements is addressed, and two treatments proposed in the literature are reviewed, and their effectiveness is also discussed.

2.1 Strong discontinuity approach

To embed a discontinuity within finite elements, two possibilities can be found in the literature: *i*) the Weak, and *ii*) Strong Discontinuity Approach (SDA). Strong discontinuities exhibit jumps in the displacement field across the discontinuity surface. The corresponding strain field, involving the gradients of the displacements, is unbounded at the discontinuity surface but bounded in the body (see – Figure 2.1). The strong discontinuity can be considered as a limit case of weak discontinuities studied in last four decades intensively (Aragón and Simone, 2017; Borst et al., 1993; Ortiz and Quigley Iv, 1991; Ortiz et al., 1987; Rots et al., 1985; Soghrati and Liang, 2016), where a discontinuity is characterised by continuous displacement field with corresponding bounded strains concentrating at a finite width band (h) of localisation (see – Figure 2.2). While the band with of localisation tends to zero, the strain jump value leads to infinity. From this moment on, the concept of strong discontinuity is found, where a singular strain field along the band is produced.

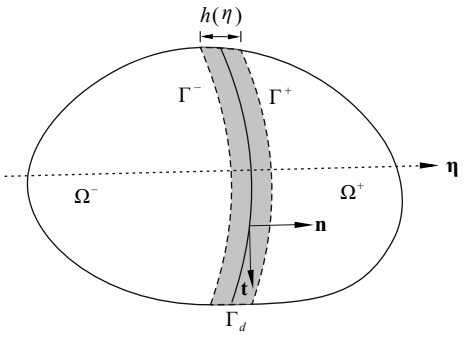

Figure 2.1: Domain Ω crossed by a strong and a weak discontinuity Γ_d.

The strong discontinuity concept is identical to 'removing' the highly deformed region from discontinuity propagation model and introducing a discontinuity in the displacement field.

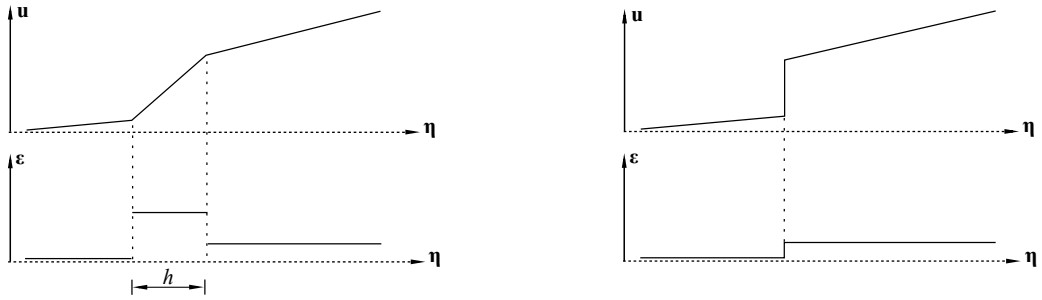

Figure 2.2: Representation of displacement and strain fields: (a) weak discontinuity (b) strong discontinuity

Although the concept of the band with finite thickness in a weak discontinuity is useful to describe some physical aspects, the definition of band thickness is not required in the strong discontinuity approach.

From the viewpoint of localisation, the weak discontinuity approach manifests initiation of localisation in the loss of ellipticity of the equilibrium equations, where material stability is lost. The softening response of the material is represented by negative tangent modulus, and the bandwidth of strain-softening tends to zero while localisation occurs. Consequently, the energy dissipation of the localisation band disappears, and the solution loses the physical meaning. As a remedy, SDA disregards the localisation region and employs cohesive traction on the two faces of a discontinuity. The dissipation work associated with the cohesive traction is considered as the plastic dissipative mechanism of the localisation band utilised in the weak discontinuity.

Since a strong discontinuity is defined as a jump in the displacement field of solids during deformation process, cracks, fractures and shear bands occurring in quasi-brittle materials

(e.g. concretes and rocks) can be considered as different types of the strong discontinuities (Oliver et al., 2004). In the following section, the main elements of the SDA are described.

2.1.1 Kinematics of a strong discontinuity

The kinematics, i.e. the strain-displacement equations of a strong discontinuity (Rabczuk et al., 2019), are described in this section.

Let us consider an elastic domain, Ω, with a smooth boundary $\partial\Omega$, crossed by a discontinuity Γ_d defining two sub-domains, Ω^+ and Ω^-. Note that the normal vector to the discontinuity surface points at the sub-domain Ω^+, as depicted in Figure 2.3.

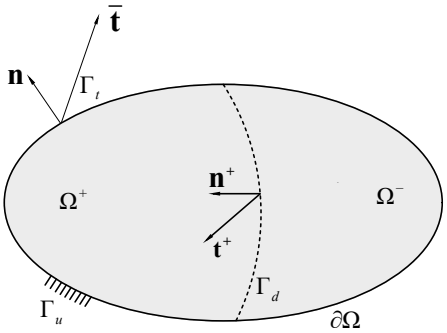

Figure 2.3: Domain Ω crossed by a discontinuity surface Γ_d.

Under these assumptions, the displacement field can be written as the sum of the continuous regular part on domain Ω, $\hat{\mathbf{u}}$, and a discontinuous part, $\tilde{\mathbf{u}}$, associated to the displacement jump (or opening), $[\![\mathbf{u}]\!]$, localised at the discontinuity Γ_d as:

$$\mathbf{u}(\mathbf{x}) = \hat{\mathbf{u}}(\mathbf{x}) + \mathrm{H}_{\Gamma_d}\tilde{\mathbf{u}}(\mathbf{x}), \tag{2.1}$$

where $\mathbf{H}_{\Gamma_d} = \mathscr{H}_{\Gamma_d}\mathbf{I}$ and $\mathscr{H}_{\Gamma_d}$ indicates the Heaviside function centred on discontinuity Γ_d defined as:

$$\mathscr{H}_{\Gamma_d} = \begin{cases} 1 \ \ if \ \mathrm{x} \in \Omega^+ \\ \\ 0 \ \ \text{otherwise} \end{cases}, \tag{2.2}$$

In Equation (2.1), the discontinuous displacement field $[\![\mathbf{u}]\!]$ is given by:

$$\tilde{\mathbf{u}}|_{\Gamma_d} = \mathbf{u}^+ - \mathbf{u}^- = [\![\mathbf{u}]\!] \tag{2.3}$$

In order to obtain the strain field whose symmetric part considered only, due to the assumption of infinitely small stains, the symmetric gradient of Equation (2.1) is taken. The corresponding infinitesimal strain field is written:

$$\nabla^s \mathbf{u} = \boldsymbol{\varepsilon} = \underbrace{\nabla^s \hat{\mathbf{u}} + \mathrm{H}_{\Gamma_d}(\nabla^s [\![\mathbf{u}]\!])}_{\text{bounded}} + \underbrace{\delta_{\Gamma_d}([\![\mathbf{u}]\!] \otimes \mathbf{n})^s}_{\text{unbounded}}, \tag{2.4}$$

where the symmetric part of $(.)$ is indicated by $(.)^s$, δ_{Γ_d} is the gradient of H_{Γ_d} in the distributional sense, known as Dirac's delta function placed at Γ_d, and $\otimes$ denotes a dyadic product. Note that, since the unbounded part of Equation (2.4) vanishes in $\Omega \backslash \Gamma_d = \Omega^+ \cup \Omega^-$, the displacement and strain fields are continuous in subdomains Ω^+ and Ω^-.

2.1.2 Boundary-value problem

As represented in Figure 2.3, a domain $\Omega \subset \mathbb{R}^2$ is split into two sub-domains (i.e. $\Omega = \Omega^+ \cup \Omega^- \cup \Gamma_d$). As a result, the displacement and strain fields are discontinuous at the discontinuity Γ_d.

A quasi-static loading is applied to the domain subjected to the body force $\mathbf{b} : \Omega \to \mathbb{R}^2$ distributed in the domain Ω. The prescribed traction $\bar{\mathbf{t}} : \Gamma_t \to \mathbb{R}^2$ is imposed on the portion of the boundary $\Gamma_t \subset \Gamma$. The prescribed displacement $\bar{\mathbf{u}} : \Gamma_u \to \mathbb{R}^2$ is applied on the complementary boundary $\Gamma_u \subset \Gamma$. It is noteworthy that Γ_t and Γ_u are disjointed boundaries (i.e. $\Gamma_t \cap \Gamma_u = \Gamma$ and $\Gamma_t \cup \Gamma_u = \emptyset$), such that the Boundary Value Problem (BVP) is well-posed (Cervera and Wu, 2015). Consequently, the governing equations are written as (Oliver et al., 2003):

$$\nabla.\boldsymbol{\sigma} + \mathbf{b} = \mathbf{0} \quad \text{in } \Omega \backslash \Gamma_d, \tag{2.5}$$

$$\boldsymbol{\varepsilon} = \nabla^s \mathbf{u} \quad \text{in } \Omega \backslash \Gamma_d, \tag{2.6}$$

$$\boldsymbol{\sigma} = \boldsymbol{\sigma}(\boldsymbol{\varepsilon}) \quad \text{in } \Omega \backslash \Gamma_d, \tag{2.7}$$

$$\mathbf{u} = \bar{\mathbf{u}} \quad \text{at } \Gamma_u, \tag{2.8}$$

$$\boldsymbol{\sigma}.\mathbf{n} = \bar{\mathbf{t}} \quad \text{at } \Gamma_t, \tag{2.9}$$

$$\boldsymbol{\sigma}^+.\mathbf{n}^+ = \mathbf{t}^+ \quad \text{at } \Gamma_d, \tag{2.10}$$

$$\boldsymbol{\sigma}^-.\mathbf{n}^- = \mathbf{t}^- \quad \text{at } \Gamma_d, \tag{2.11}$$

$$\mathbf{t}^+ = -\mathbf{t}^- \quad \text{at } \Gamma_d, \tag{2.12}$$

where the tensor $\boldsymbol{\sigma} : \Omega \backslash \Gamma_d \to \mathbb{R}^{2\times 2}$ indicates the stress field in the bulk with $\boldsymbol{\sigma}^+$ and $\boldsymbol{\sigma}^-$ denoting the bulk stresses on the two sides of the discontinuity surface, as depicted in Figure 2.3; and the cohesive traction transferred between two faces of the discontinuity is denoted by vector $\mathbf{t}$. Equation (2.5) represents the internal equilibrium, while the external equilibrium derived by essential (also called Dirichlet) and natural (also called Neumann) boundary conditions, represented by Equations (2.8) and (2.9) respectively. Equations (2.6) and (2.7)

represent kinematic and constitutive compatibility relations respectively, and Equations (2.10), (2.11) and (2.12) form the traction continuity condition at the discontinuity Γ_d (Dias-da-Costa et al., 2009).

2.1.3 Variational formulation

In this section, a brief description of the variational formulation of the strong discontinuity approach is taken into consideration. Regarding this topic, the reader is referred to the study conducted by Alfaiate et al. (2003), where the variational formulation is investigated for various discrete approaches. Simo et al. (1993) reported a non-symmetric formulation resulted from the traction continuity imposed in a strong form of the formulation. On the other hand, Lotfi and Shing (1995) introduced a consistent symmetric weak formulation with the traction continuity enforced in the weak sense, which is the formulation utilised in the XFEM and PUM (Duarte and Oden, 1996a; Melenk and Babuška, 1996; Moës et al., 1999).

The most general assumption is the extension of the three-field Hu-Washizu variational statements proposed by Washizu (1975), where $\mathbf{u}$, $\boldsymbol{\varepsilon}$, $\boldsymbol{\sigma}$, $[\![\mathbf{u}]\!]$ may be considered as independent unknown fields. Later, Lotfi and Shing (1995) explored this possibility and proposed mixed finite elements, which can be used in order to approximate the independent unknown fields. In this approach, a consistent symmetric weak form is adopted, where Equation (2.6) is automatically satisfied according to Equation (2.4), which is usually considered in the XFEM approach. For example, the discontinuity is considered as an internal boundary in (Simone, 2004) and the principal of virtual work is separately imposed on Ω and Ω^+, while Wells and

Sluys (2001a) inserts the Dirac-delta function into the virtual work equation over the body Ω to eliminate the unbounded term $[\![\mathbf{u}]\!]$ and satisfy the traction continuity.

Here, the variational formulation represented is identical to the discrete-interface approach (Dias-da-Costa et al., 2009) to clearly identify the terms required in the discrete strong discontinuity approach, which is the main aim of the chapter 3. The virtual work equation reads:

$$-\int_{\Omega\setminus\Gamma_d}(\nabla^s\delta\mathbf{u}):\sigma\,d\Omega+\int_{\Omega\setminus\Gamma_d}\delta\mathbf{u}.\mathbf{b}\,d\Omega+\int_{\Gamma_t}\delta\mathbf{u}.\bar{\mathbf{t}}\,d\Gamma+\int_{\Gamma_d}\delta\,[\![\mathbf{u}]\!].\mathbf{t}^+\,d\Gamma=0, \tag{2.13}$$

where (.) and (:) represent single and double contractions; $\int_{\Omega\setminus\Gamma_d}(\nabla^s\delta\mathbf{u}):\sigma\,d\Omega+\int_{\Omega\setminus\Gamma_d}\delta\mathbf{u}.\mathbf{b}\,d\Omega$ and $\int_{\Omega\setminus\Gamma_d}\delta\mathbf{u}.\mathbf{b}\,d\Omega+\int_{\Gamma_t}\delta\mathbf{u}.\bar{\mathbf{t}}\,d\Gamma$ denote the strain energy and the external work respectively, which are the terms used in continuum approach; and $\int_{\Gamma_d}\delta\,[\![\mathbf{u}]\!].\mathbf{t}^+\,d\Gamma$ is added as the work done in the discontinuity Γ_d (Malvern, 1969).

According to Equation (2.1), $\delta\mathbf{u}=\delta\hat{\mathbf{u}}+\mathbf{H}_{\Gamma_d}\delta\tilde{\mathbf{u}}$. Since the variations of $\delta\hat{\mathbf{u}}$ and $\delta\tilde{\mathbf{u}}$ are nonzero, $\delta\tilde{\mathbf{u}}_{|\Gamma_d}=\delta\,[\![\mathbf{u}]\!]$, and the field stress in the continuum depends upon regular strain $\hat{\varepsilon}$, the two variational statements are written as:

$$-\int_{\Omega\setminus\Gamma_d}(\nabla^s\delta\hat{\mathbf{u}}):\sigma\,(\hat{\varepsilon})\,d\Omega+\int_{\Omega\setminus\Gamma_d}\delta\hat{\mathbf{u}}.\mathbf{b}\,d\Omega+\int_{\Gamma_t}\delta\hat{\mathbf{u}}.\bar{\mathbf{t}}\,d\Gamma=0, \tag{2.14}$$

$$-\int_{\Omega}\mathrm{H}_{\Gamma_d}(\nabla^s\delta\,[\![\mathbf{u}]\!]):\sigma(\hat{\varepsilon})\,d\Omega+\int_{\Omega}\mathrm{H}_{\Gamma_d}\delta\,[\![\mathbf{u}]\!].\mathbf{b}\,d\Omega+\int_{\Gamma_t}\mathrm{H}_{\Gamma_d}\delta\,[\![\mathbf{u}]\!].\bar{\mathbf{t}}\,d\Gamma+\int_{\Gamma_d}\delta\,[\![\mathbf{u}]\!].\mathbf{t}^+\,d\Gamma=0. \tag{2.15}$$

It is worth mentioning that Equation (2.14) results from Virtual Work Principle applied for a bulk, which is the same as one utilised in the PUM (Simone et al., 2003; Wells and Sluys,

2001a). Accordingly, Equation (2.15) may be interpreted as the Virtual Work Principle applied to subdomain Ω^+.

2.2 Discrete constitutive models

The fracture behaviour of quasi-brittle materials is simulated by numerical models based on the finite element method (FEM), traditionally classified into two main groups: smeared and discrete crack approaches (Gálvez et al., 2002).

The smeared crack approach states that many microcracks with infinitely small opening are distributed (smeared) within the finite element region. The propagation of these cracks is simulated by stiffness reduction or strength degradation of the material. The fixed (Rashid, 1968) and rotating crack (Gupta and Akbar, 1984) models are the first models proposed in this approach (De Borst and Nauta, 1985; Rots, 1988).

The discrete crack approach is preferred when a finite number of cracks dominate the fracture behaviour in a structure. The cohesive model, also known as fictitious crack model, developed by Hillerborg et al. (1976), has had considerable success in fracture of quasi-brittle materials. The softening function, ($\sigma = f(\llbracket \mathbf{u} \rrbracket)$), defined as a main ingredient of this approach, relates the stress σ transferring between the two face of the crack to the corresponding crack opening $\llbracket \mathbf{u} \rrbracket$ (see – Figure 2.4).

The main parameters of softening functions measured experimentally are the tensile strength f_t and fracture energy, which is the energy required for breaking a unit surface area and equals

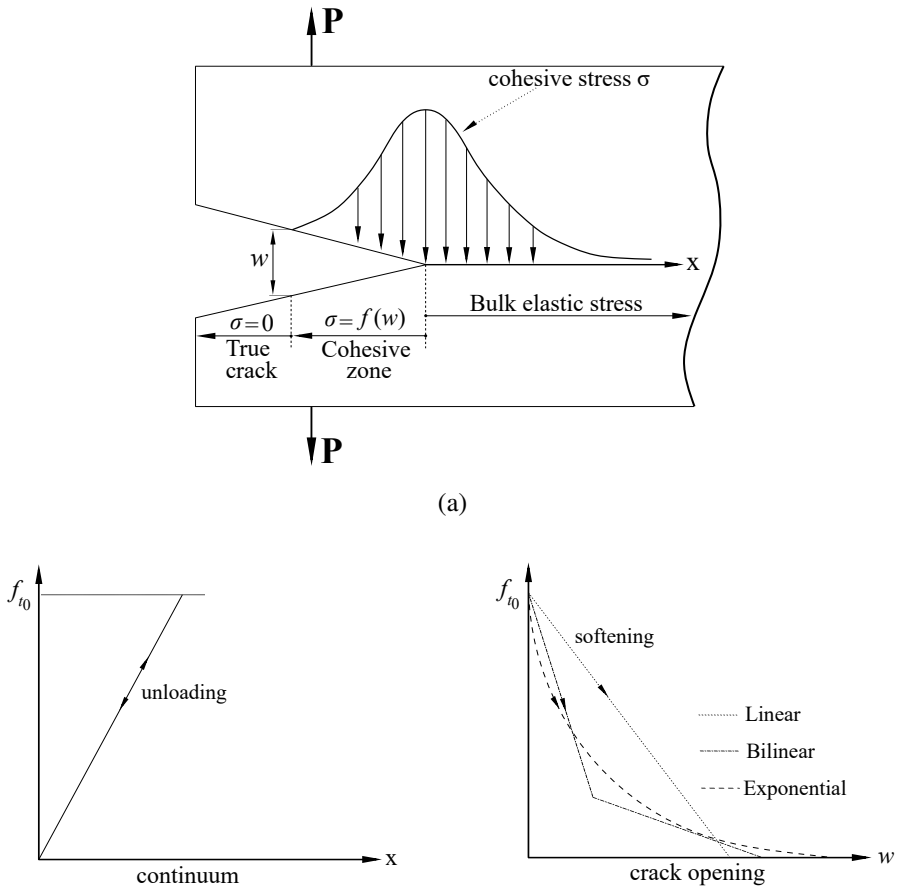

Figure 2.4: Discrete material models- (a) cohesive crack for a specimen under tension (b) material model for continuum and cohesive crack with different softening laws.

the area under the softening curve. As represented in Figure 2.4, many softening functions are available to model quasi-brittle material fracture, namely linear, bilinear and exponential laws (Bazant and Planas, 1997; Cornelissen et al., 1986; Gopalaratnam and Shah, 1985).

The crack closure as a realistic feature of a discontinuity should be considered in the softening function. To this end, a penalty function is utilised not to allow the two faces of a discontinuity

to overlap while the normal displacement jump tends to zero as bellow:

$$\mathbf{t} = \mathbf{T}_{el} \llbracket \mathbf{u} \rrbracket, \tag{2.16}$$

$$\mathbf{T}_{el} = \begin{bmatrix} k_n & 0 \\ 0 & k_s \end{bmatrix}, \tag{2.17}$$

Where $\mathbf{t}$ shows the traction vectors, $\llbracket \mathbf{u} \rrbracket$ is jump vectors, and k_n and k_s denote the normal and the shear penalties respectively.

There are two main stages to simulate the concrete fracture, including crack initiation and propagation. In the former, a criterion is required to incorporate the cohesive crack into the parent element. The latter introduces the crack path needed for the crack incorporation. In contrast with the fracture mode-I, where the stress, σ, transferred between two faces of the crack is normal to the crack faces, the interaction between normal stress, σ, and tangential stress, τ, should be considered in mixed-mode fracture.

The cracking evolution may be modelled according to fracture mode-I with zero shear stress at the discontinuity, or mixed-mode fracture, where shear stress can develop between two faces of the discontinuity. Some damage models proposed in the literature are discussed in section 2.2.2 to take into account different types of the fracture (e.g. mode-I, mode-II and mixed-mode).

In discrete crack approach, some assumptions are considered: *i*) a crack initiation occurs when the combination of normal and tangential stress reaches a cracking pocket $F(\sigma, \tau) = 0$; *ii*) the microcracks are localised in the zero bandwidth and form strong discontinuity as

discussed in section 2.1; *iii*) the discontinuity evolves according to the softening function expressed by fictitious crack model; *iv*) simultaneously the bulk around the discontinuity begins unloading to satisfy the traction continuity condition.

As discussed in section 2.1.1, the displacement in the domain of the body consists of continuous and discontinuous parts, the latter associated with the displacement jump at the discontinuity (see – Equation (2.1)). In discrete crack approach, assumptions *i* and *iv* provide a crucial link between the bulk and discontinuity for modelling; otherwise bulk is uninformed about strain localisation.

2.2.1 Initiation criterion

The numerical simulation of strong discontinuities can be classified into two main groups: continuum and discrete approaches. In the former, since the strain concept is similarly defined for bulk and interface, which means that standard stress-strain constitutive equations are applicable for the complete body. Two basic ingredients of this approach are: *i*) regularisation of the discontinuous displacement field approximated by high displacement gradients, i.e. strain localisation, in a bandwidth known as characteristic length; *ii*) definition of constitutive equations allow the strain localisation to appear in a problem (Oliver, 1996).

Conversely, discrete approaches (Dvorkin et al., 1990; Lofti and Shing, 1994) define the relation between traction and jump at the discontinuity (traction-separation law) to characterise the factious crack (cohesive zone) behaviour at the discontinuity surface, while the regular stress-strain constitutive law is considered for the continuous counterpart of the body. As a

consequence, an appropriate criterion is required to determine the discontinuity initiation and propagation.

To sum up, the onset of strain localisation determined by the acoustic tensor is employed as the initiation criterion in continuum-based theories. Since a strong discontinuity may be obtained as a limit case of a weak discontinuity (see – section 2.1), the discrete (stress versus displacement jump) constitutive equations at the discontinuity can be considered as the projection of the standard continuum constitutive law. Despite the consistency of this formulation, some difficulties can arise due to the dependence of material laws given for bulk and discontinuity (Oliver, 1996). Alfaiate et al. (2003) and Bolzon (2001) suggested an alternative, where the bulk uses an elastic relationship, leading to an independent discrete material law. Since the strain localisation cannot be monitored by the bulk material model in this approach, an initiation criterion needs to be introduced instead. Further details regarding the initiation criterion are given in the chapter 3.

2.2.2 Damage models

Four damage models used in this study are described briefly in the following sections.

Damage model by Mariani and Perego (2003)

The current section provides a short description of the discrete cohesive law modified by Mariani and Perego (2003) based on effective displacement, which is appropriate for quasi-brittle materials under mixed-mode.

The crack displacement can be decomposed into two components: the crack opening normal to the crack path, and crack sliding tangential to the crack path. Consider $\mathbf{t}_s$ and $\mathbf{t}_n$ the normal and tangential components of the traction between two sides of the crack. The effective opening displacement based on the embedded crack model (Jirásek and Zimmermann, 2001) is defined as:

$$[\![\mathbf{u}]\!]_{eq} = \sqrt{[\![\mathbf{u}]\!]_n^2 + \beta^2 [\![\mathbf{u}]\!]_s^2} \tag{2.18}$$

where$[\![\mathbf{u}]\!]_n$ and $[\![\mathbf{u}]\!]_s$ denote the normal and tangential components of displacement jump, respectively. The total incremental work equivalence may derive the equivalent traction in terms of perpendicular traction components $\mathbf{t}_s$ and $\mathbf{t}_n$:

$$\mathbf{t}_{eq}[\![\dot{\mathbf{u}}]\!]_{eq} = \mathbf{t}_n[\![\dot{\mathbf{u}}]\!]_n + \mathbf{t}_s[\![\dot{\mathbf{u}}]\!]_s \tag{2.19}$$

$$[\![\dot{\mathbf{u}}]\!]_{eq} = \frac{[\![\dot{\mathbf{u}}]\!]_n}{[\![\dot{\mathbf{u}}]\!]_{eq}}[\![\dot{\mathbf{u}}]\!]_n + \beta^2 \frac{[\![\dot{\mathbf{u}}]\!]_s}{[\![\dot{\mathbf{u}}]\!]_{eq}}[\![\dot{\mathbf{u}}]\!]_s \tag{2.20}$$

Therefore, satisfying the work equivalence results in traction vector components as below:

$$\mathbf{t}_n = \frac{\mathbf{t}_{eq}}{[\![\mathbf{u}]\!]_{eq}}[\![\mathbf{u}]\!]_n \quad , \quad \mathbf{t}_s = \beta^2 \frac{\mathbf{t}_{eq}}{[\![\mathbf{u}]\!]_{eq}}[\![\mathbf{u}]\!]_s \tag{2.21}$$

According to Camacho and Ortiz (1996), the different weights related to opening and sliding components of the two crack faces are considered as a coefficient β, which basically controls the shear strength and shear stiffness in mode-II. The damage criterion is adopted to define the crack opening under mixed-mode fracture, derived by history variable α and equivalent crack opening $[\![\mathbf{u}]\!]_{eq}$ as:

$$f([\![\mathbf{u}]\!], \alpha) = [\![\mathbf{u}]\!]_{eq} - \alpha \leq 0. \tag{2.22}$$

On the other hand, the relation between equivalent traction and crack opening is written as:

$$\mathbf{t}_{eq} = \mathbf{T}[\![\mathbf{u}]\!]_{eq} = (\mathbf{T}^e - \mathbf{T}^d)[\![\mathbf{u}]\!]_{eq}, \tag{2.23}$$

$\mathbf{T}^e$ is the initial isotropic stiffness matrix and $\mathbf{T}^d$ denotes the damage tensor controlling the degradation of equivalent interface stiffness $\mathbf{T}$. The function of α is adopted for damage stiffness $\mathbf{T}^d$ as:

$$\mathbf{T}^d = \mathbf{T}^e \left[1 - \frac{\alpha_0}{\alpha} \exp\left(-\frac{f_t}{G_F}(\alpha - \alpha_0)\right)\right] \tag{2.24}$$

where f_t and G_F are the tensile strength and fracture energy, and α_0 shows the initial value of α:

$$\alpha_0 = \frac{f_t}{\mathbf{T}^e}. \tag{2.25}$$

From the Kuhn–Tucker and consistency conditions with damage criterion Equation (2.22) follows:

$$\alpha = [[\mathbf{u}]]_{eq} \ , \ \ \dot{\alpha} = [[\dot{\mathbf{u}}]]_{eq} \tag{2.26}$$

From the derivation of Equation (2.23), and considering Equation (2.19) and Equation (2.21), the tangent stiffness matrix is written as:

$$\Delta \mathbf{t} = -\frac{\beta^2 f_t \mathbf{T}^{se}}{[\![\mathbf{u}]\!]_{eq}} \begin{bmatrix} \frac{[\![\mathbf{u}]\!]_n^2}{\beta^2 G_F} - \frac{[\![\mathbf{u}]\!]_s^2}{f_t [\![\mathbf{u}]\!]_{eq}} & [\![\mathbf{u}]\!]_s [\![\mathbf{u}]\!]_n \frac{G_F + f_t [\![\mathbf{u}]\!]_{eq}}{G_F f_t [\![\mathbf{u}]\!]_{eq}} \\ [\![\mathbf{u}]\!]_s [\![\mathbf{u}]\!]_n \frac{G_F + f_t [\![\mathbf{u}]\!]_{eq}}{G_F f_t [\![\mathbf{u}]\!]_{eq}} & \frac{\beta^2 [\![\mathbf{u}]\!]_s}{G_F} - \frac{[\![\mathbf{u}]\!]_n^2}{f_t [\![\mathbf{u}]\!]_{eq}} \end{bmatrix} \Delta [\![\mathbf{u}]\!], \tag{2.27}$$

where $\mathbf{T}^{se}$ is:

$$\mathbf{T}^{se} = (\mathbf{T}^e - \mathbf{T}^d) = \mathbf{T}^e \frac{\alpha_0}{\alpha} \exp\left(-\frac{f_t}{G_F}(\alpha - \alpha_0)\right). \tag{2.28}$$

If unloading occurs, the tangential relation reduces to:

$$\Delta \mathbf{t} = \mathbf{T}^{se} \begin{bmatrix} 1 & 0 \\ 0 & \beta^2 \end{bmatrix} \Delta [\![\mathbf{u}]\!] . \tag{2.29}$$

Damage model by Alfaiate et al. (2002)

In this section, the isotropic damage law proposed by Alfaiate et al. (2002) is reviewed.

Damage models defined in the thermodynamic framework are based on Helmholtz free energy density. The interpretation of the formulations used in standard thermodynamic results in the constitutive relation:

$$\mathbf{t} = (1-d)\mathbf{T}_{el} [\![\mathbf{u}]\!] , \tag{2.30}$$

where $0 < d < 1$ denotes the damage parameter (where $d = 0$ and 1, respectively for undamaged and fully damaged states, respectively), and $\mathbf{T}_{el}$ shows the elastic constitutive tensor (see – Equation (2.16)). The damage evolution is written as:

$$d(\kappa) = 1 - \frac{\kappa_0}{\kappa} \exp\left(-\frac{f_t}{G_F}(\kappa - \kappa_0) \right), \tag{2.31}$$

where κ_0 represents the beginning of softening ($\kappa = \kappa_0$ before damage occurs in the model). κ denotes a scalar, taking into account both maximum positive normal and shear jump components $[\![u]\!]_n$ and $[\![u]\!]_s$ respectively:

$$\kappa = \max \langle [\![u]\!]_n \rangle^+ + \beta \max |[\![u]\!]_s| . \tag{2.32}$$

The scalar variable κ may be considered as an equivalent jump ($\kappa = [\![\mathbf{u}]\!]$), which is a function of the displacement jump ($\kappa = k([\![\mathbf{u}]\!])$). Consequently, the load function in terms of displacement jump components is defined:

$$f = \langle [\![\mathbf{u}]\!]_n \rangle^+ + \beta \, |[\![\mathbf{u}]\!]_s| - \kappa \leq 0 \tag{2.33}$$

In which the factor β governs the ratio between the shear jump component and the equivalent jump parameter. It is noteworthy that $\beta = 0$ when the shear jump component is not considered, whereas $\beta \approx f_t/c_0$ (c_0 is the cohesion) according to Alfaiate et al. (2002).

The elastic tensor $\mathbf{T}_{el}$ is defined by an initial value k_0 for internal scalar variable such that $k_0 < k$ and close to zero :

$$\mathbf{T}_{el} = \frac{f_t}{k_0}\mathbf{I} \tag{2.34}$$

where $\mathbf{I}$ denotes the Kronecker tensor.

Inserting Equation (2.34) and Equation (2.31) into Equation (2.30) leads to the constitutive relation in the matrix form:

$$\left\{ \begin{array}{c} t_n \\ t_s \end{array} \right\} = \frac{\kappa_0}{\kappa} \exp\left[-\frac{f_t}{G_F}(\kappa - \kappa_0) \right] \left[\begin{array}{cc} 1 & 0 \\ 0 & 1 \end{array} \right] \left\{ \begin{array}{c} [\![\mathbf{u}]\!]_n \\ [\![\mathbf{u}]\!]_s \end{array} \right\}. \tag{2.35}$$

According to Equation (2.35), the initial equivalent jump κ_0 does not influence results considerably because it is removed from the product $\left(\frac{\kappa_0}{\kappa}\right) . \left(\frac{f_t}{\kappa_0}\right)$. As a result, κ_0 only has an effect on the exponential law at the beginning of the softening.

The rate form of constitutive relation is obtained by differentiating Equation (2.30) as below:

$$\dot{\mathbf{t}} = (1-d)\,\mathbf{T}_{el}\,[\![\dot{\mathbf{u}}]\!] - \dot{d}\,\mathbf{T}_{el}\,[\![\mathbf{u}]\!] = (1-d)\,\mathbf{T}_{el}\,[\![\dot{\mathbf{u}}]\!] - \dot{d}\,\mathbf{t}_{el} \tag{2.36}$$

where $\mathbf{t}_{el}$ denotes the elastic traction vector and $\dot{d}$ is given:

$$\dot{d} = \frac{\partial d}{\partial \kappa}\frac{\partial \kappa}{\partial [\![\mathbf{u}]\!]} \tag{2.37}$$

From Equation (2.37) and Equation (2.36):

$$\dot{\mathbf{t}} = \left[(1-d)\mathbf{T}_{el} - \frac{\partial d}{\partial \kappa}\mathbf{t}_{el} \otimes \frac{\partial \kappa}{\partial [\![\mathbf{u}]\!]}\right][\![\dot{\mathbf{u}}]\!]\,. \tag{2.38}$$

If unloading occurs the rate of damage variable is zero ($\dot{d} = 0$). Therefore, both Equation (2.36) and Equation (2.38) reduce to:

$$\dot{\mathbf{t}} = (1-d)\mathbf{T}_{el}\,[\![\dot{\mathbf{u}}]\!]\,. \tag{2.39}$$

Note that while crack closure takes place, the initial elastic constitutive relation needs to be recovered. Since the penalty function is adopted, $[\![\mathbf{u}]\!]_n \approx 0$. In compressive tractions state, no limitation on the value of shear traction inforced causes the isotropic damage model, introduced here, to be inappropriate to describe the friction occurring between two crack faces under the compressive stress.

Damage model by Wells and Sluys (2001a)

In this following, the damage model proposed by Wells and Sluys (2001a) in 2D is reviewed. Further information regarding the 3D version of the model is given in (Wells and Sluys, 2001c).

Consider a loading function as below:

$$f(\llbracket \mathbf{u} \rrbracket_n, \kappa) = \llbracket \mathbf{u} \rrbracket_n - \kappa, \tag{2.40}$$

where κ denotes the internal variable, which is the maximum value of $\langle \llbracket \mathbf{u} \rrbracket_n \rangle^+$ during the loading history. The loading is determined if $f \geq 0$, whereas unloading is considered by $f < 0$. An exponential function decaying is considered as the constitutive relation between the normal traction t_n and the normal jump $\llbracket \mathbf{u} \rrbracket_n$ considered in internal variable κ:

$$t_n = f_t \exp\left(-\frac{f_t}{G_F}\kappa\right), \tag{2.41}$$

where f_t and G_F are the tensile strength and fracture energy of the material respectively.

An exponential function similar to t_n is adopted to relate the shear traction t_s to sliding displacement along the discontinuity (shear jump) $\llbracket \mathbf{u} \rrbracket_s$ as follows:

$$t_s = D_{s\kappa_0} \exp(h_s \kappa) \llbracket \mathbf{u} \rrbracket_s, \tag{2.42}$$

where $D_{s\kappa_0}$ denotes shear stiffness at the crack initiation ($\kappa = 0$) and h_s is defined:

$$h_s = -\ln\left(\frac{D_{s\kappa}}{D_{s\kappa_0}}\right) \tag{2.43}$$

where $D_{s\kappa}$ is the shear stiffness adopted for $\kappa \gg 0$.

Differentiating Equation (2.41) and Equation (2.42) and writing the rate form of the constitutive relation matrix is given:

$$\left\{\begin{array}{c} \dot{t}_n \\ \dot{t}_s \end{array}\right\} = \left[\begin{array}{cc} -\frac{f_t^2}{G_F}\exp\left(-\frac{f_t}{G_F}\kappa\right) & 0 \\ h_s D_{s\kappa_0}\exp\left(h_s\kappa\right)[\![\mathbf{u}]\!]_s & D_{s\kappa_0}\exp\left(h_s\kappa\right) \end{array}\right] \left\{\begin{array}{c} [\![\dot{\mathbf{u}}]\!]_n \\ [\![\dot{\mathbf{u}}]\!]_s \end{array}\right\} \tag{2.44}$$

The softening behaviour described by this model is dominated by the normal jump only, and the shear stiffness tends to zero when cracking mode-I is considered. On the other hand, since shear stiffness is dependent on the normal jump, the tangential relation between traction vectors and displacement jumps is non-symmetric. One of the simplifications adopted is to consider the constant shear stiffness at the discontinuity, leading to symmetric global stiffness matrix. However, very small constant shear stiffness causes brittle global response at the post-peak loading, whereas very high value leads to stress locking (Rots, 1988).

If unloading occurs, the secant stiffness matrix is given by:

$$\mathbf{D} = \left[\begin{array}{cc} \frac{f_t}{\kappa}\exp\left(-\frac{f_t}{G_F}\kappa\right) & 0 \\ 0 & D_{s\kappa_0}\exp\left(h_s\kappa\right) \end{array}\right]. \tag{2.45}$$

The full crack closure is treated by elastic stiffness recovery as previously described in Equation (2.16).

Uncoupled damage model

Another approach simplifying the cracking model mode-I is derived based on the assumption that the shear stiffness suddenly reduces to zero while the crack begins opening. Accordingly, since the shear traction of the discontinuity remains unchanged, an uncoupled relation between shear and normal components is obtained.

If the loading function in Equation (2.40) and softening law presented in Equation (2.41) are considered, the rate form of constitutive relation in the matrix form can be given by:

$$\left\{ \begin{array}{c} \dot{t}_n \\ \dot{t}_s \end{array} \right\} = - \left[\begin{array}{cc} -\frac{f_t^2}{G_F} \exp\left(-\frac{f_t}{G_F}\kappa\right) & 0 \\ 0 & 0 \end{array} \right] \left\{ \begin{array}{c} \dot{w}_n \\ \dot{w}_s \end{array} \right\}. \tag{2.46}$$

The sudden unrealistic loss of shear stiffness can cause numerical difficulties. As a remedy, a gradual reduction in shear stiffness, which is proportional to the secant stiffness mode-I can be adopted as:

$$\left\{ \begin{array}{c} \dot{t}_n \\ \dot{t}_s \end{array} \right\} = - \left[\begin{array}{cc} -\frac{f_t^2}{G_F} \exp\left(-\frac{f_t}{G_F}\kappa\right) & 0 \\ 0 & \frac{c_0 k_s \exp\left(-\frac{f_t}{G_F}\kappa\right)}{k_n \kappa} \end{array} \right] \left\{ \begin{array}{c} \dot{w}_n \\ \dot{w}_s \end{array} \right\}. \tag{2.47}$$

Note that, the crack closure is treated according to Equation (2.16) as described earlier.

2.3 eXtended Finite Element Method (XFEM)

The simulation of crack propagation in the context of standard finite element methods can be very complex. This difficulty results both from topology aspects and from the insufficiency of the piecewise differentiable functions adopted for the field approximations, which are unable to represent the singularity at the crack tip accurately (Pin and Pian, 1973). As a result, substantial mesh refinement may be needed for the analysis of discontinuities and singularities, which has a considerable numerical cost. To tackle the weakness in standard finite element, XFEM is developed by Belytschko and Black (1999) and Moës et al. (1999) to treat weak and strong discontinuities. The key advantage of XFEM is related to its conformity, allowing mesh edges not to locate along the discontinuity path. As the main focus of this study is on strong discontinuities, the modelling of strong discontinuity by means of XFEM framework is described in the following section. For more detailed overview and usage of XFEM, the readers are referred to (Belytschko et al., 2013; Fries and Belytschko, 2010; Rabczuk et al., 2019; Yazid et al., 2009).

2.3.1 XFEM for strong discontinuities

Extrinsic enrichments are adopted in many enriched methods such as the XFEM, GFEM and the PUM, based on the PU concept introduced by Melenk and Babuška (1996). The main feature that separates XFEM from methods mentioned above is the local enrichment achieved by employing nodal enrichment technique, described in section 2.3.3.

Partition of Unity (PU)

The finite element approximation needs to satisfy the Partition of Unity requirements for convergence. The polynomial shape functions widely used to approximate the fields in finite element have this property, given by:

$$\sum_{i=1}^{n_i} \varphi_i(\mathbf{x}) = 1 \tag{2.48}$$

where φ_i is the sum of the functions belonging to a node $\mathbf{x}$ located on domain Ω (see – section 2.1.1), and n_i represents the number of nodal points.

Since a field may be interpolated by discrete nodal values utilising PU (Duarte and Oden, 1996b), any function $\Psi(\mathbf{x})$ reproduced by functions satisfying PU can be employed in XFEM. This is also called the reproducing condition (Liu et al., 1995). Accordingly, the standard finite element method approximation can be rewritten as:

$$\mathbf{u}(\mathbf{x}) = \sum_{i=1}^{n_i} N_i(\mathbf{x})\Psi(\mathbf{x})\hat{\mathbf{a}}, \tag{2.49}$$

where N_i denotes standard shape functions of FEM, and $\hat{\mathbf{a}}$ are corresponding regular nodal degrees of freedom.

Note that, $\Psi(\mathbf{x}) = 1$ in the standard FEM approximation. Conceptually, XFEM exploits the flexibility of $\Psi(\mathbf{x})$ in various forms, including a discontinuous function. Since this substitution is only required locally like in discontinuity surfaces, the rest of the domain can

be approximated by standard FEM, leading to the enhanced form:

$$\mathbf{u}(\mathbf{x}) = \underbrace{\sum_{i=1}^{n_i} N_i(\mathbf{x}) 1(\mathbf{x}) \hat{\mathbf{a}}}_{standard} + \underbrace{\sum_{j=1}^{n_i} \varphi_i(\mathbf{x}) \Psi(\mathbf{x}) \tilde{\mathbf{a}}}_{enhanced} \tag{2.50}$$

where the displacement field $\mathbf{u}(\mathbf{x})$ is interpolated based on the standard and additional degrees of freedom $\hat{\mathbf{a}}$ and $\tilde{\mathbf{a}}$ respectively. Even though there is no requirement, generally the standard finite element shape functions are also used in XFEM framework. Therefore, $\varphi_i(\mathbf{x}) = N_i(\mathbf{x})$ (Belytschko et al., 2013; Wells and Sluys, 2001a).

Strong discontinuity approximation in enhanced form

Function $\Psi(\mathbf{x})$ is used as means to incorporate the strong discontinuity. This can be done with the Heaviside function, as defined in Equation (2.2).

A signed distance function, also known as level set, is utilised to describe the discontinuity as:

$$\varphi(\mathbf{x}) = \mathbf{x} - \mathbf{x}_{dis}, \tag{2.51}$$

where $\mathbf{x}_{dis}$ denotes the location of the discontinuity.

Inserting Equation (2.51) in Equation (2.2) and considering the standard finite element shape function in lieu of $\varphi_i(\mathbf{x})$ combined with Equation (2.50) leads to the displacement of an element cut by the discontinuity as:

$$\mathbf{u}(\mathbf{x}) = \sum_{i=1}^{n_i} N_i(\mathbf{x}) \hat{\mathbf{a}} + \sum_{j=1}^{n_i} N_i(\mathbf{x}) \mathrm{H}(\varphi(\mathbf{x})) \tilde{\mathbf{a}}. \tag{2.52}$$

To avoid incompatibility at the nodes shared by the elements with unenriched displacement field, the shifting approximation is used as a remedy (Fries and Belytschko, 2010). Accordingly, the effect of $\tilde{a}$ on the nodes is omitted by shifting (e.g. $\Psi_j(\mathbf{x}) = \mathrm{H}(\varphi(\mathbf{x})) - \mathrm{H}(\varphi(\mathbf{x}_j))$) and the approximation of standard XFEM is derived as:

$$\mathbf{u}(\mathbf{x}) = \sum_{i=1}^{n_i} N_i(\mathbf{x})\hat{\mathbf{a}} + \sum_{j=1}^{n_j} N_j(\mathbf{x}) \left[\mathrm{H}(\varphi(\mathbf{x}) - \mathrm{H}(\varphi(\mathbf{x}_j))\right] \tilde{\mathbf{a}} \tag{2.53}$$

where n_j denotes the number of additional degrees of freedom.

2.3.2 Variational formulation

There are different valid variational formulation for XFEM in the literature. Moës et al. (1999) and Pommier et al. (2011) use the approach proposed by Belytschko and Black (1999) to satisfy the strong form of equations with traction-free condition on discontinuity. Wells and Sluys (2001a) employs the Dirac's delta function to calculate the energy dissipated by discontinuity. Here, the formulation presented by Malvern (1969) is reviewed.

$$\int_{\Omega\setminus\Gamma_d} (\nabla^s \delta\mathbf{u}) : \boldsymbol{\sigma}(\boldsymbol{\varepsilon})\, d\Omega + \int_{\Gamma_d} \delta \left[\!\left[\mathbf{u}\right]\!\right] . \mathbf{t}^+ d\Gamma = \int_{\Omega\setminus\Gamma_d} \delta\mathbf{u} . \bar{\mathbf{b}}\, d\Omega + \int_{\Gamma_t} \delta\mathbf{u} . \bar{\mathbf{t}}\, d\Gamma \tag{2.54}$$

where $\delta\mathbf{u}$ and $\delta \left[\!\left[\mathbf{u}\right]\!\right]$ are the admissible variations of displacement and jump respectively; $\mathbf{t}^+$ denotes traction vector at the discontinuity.

According to Equation (2.1), the virtual total displacement $\delta\mathbf{u}$ is the combination of regular $\delta\hat{\mathbf{u}}$ and enhanced $\delta\tilde{\mathbf{u}}$ displacements as:

$$\delta\mathbf{u} = \delta\hat{\mathbf{u}} + \mathrm{H}_{\Gamma_d}\delta\tilde{\mathbf{u}} \tag{2.55}$$

Inserting Equation (2.55) into Equation (2.54), and differentiating $\delta\hat{\mathbf{u}} = 0$ and then $\delta\tilde{\mathbf{u}} = 0$, while $\delta\tilde{\mathbf{u}}_{|\Gamma_d} = \delta[\![\mathbf{u}]\!]$ results in:

$$\int_{\Omega\setminus\Gamma_d} (\nabla^s \delta\hat{\mathbf{u}}) : \sigma(\varepsilon)\, d\Omega = \int_{\Omega\setminus\Gamma_d} \delta\hat{\mathbf{u}} \,.\, \bar{\mathbf{b}}\, d\Omega + \int_{\Gamma_t} \delta\hat{\mathbf{u}} \,.\, \bar{\mathbf{t}}\, d\Gamma, \tag{2.56a}$$

$$\int_{\Omega^+} (\nabla^s \delta\tilde{\mathbf{u}}) : \sigma(\varepsilon)\, d\Omega + \int_{\Gamma_d} \delta[\![\mathbf{u}]\!] .\, \mathbf{t}^+ d\Gamma = \int_{\Omega^+} \delta\tilde{\mathbf{u}} \,.\, \bar{\mathbf{b}}\, d\Omega + \int_{\Gamma_{t^+}} \delta\tilde{\mathbf{u}} \,.\, \bar{\mathbf{t}}\, d\Gamma. \tag{2.56b}$$

Equation (2.56a) and Equation (2.56b) satisfy the consistency of the weak formulation adopted in XFEM.

2.3.3 Nodal enrichment technique

As earlier discussed in section 2.3.1, the main significance of XFEM compared to the other enriched models lies on the framework enriching the nodes locally. According to (Wells and Sluys, 2001a), two main conditions should be taken into account as follows:

i) As seen in Equation (2.50), the function $\Psi(\mathbf{x})$ multiplies a set of specific nodes. Thus only the support of those nodes is affected by the function. Consequently, the shifted function only needs to be considered for nodes whose support is cut by the discontinuity.

ii) The displacement jump at the discontinuity tip should equal zero. To this end, the nodes located on the boundary of the element touched by the discontinuity tip require to be enriched when the crack passes the element and propagates into the neighbour element.

Discrete equations

The XFEM discretisation is obtained by inserting Equation (2.53) into the virtual work principle, which is comprehensively detailed in (Simone et al., 2003; Wells and Sluys, 2001a). The discrete equations are reviewed in this section.

As described in section 2.3.1, the total displacement field in XFEM is decomposed into two continuous displacement fields, $\hat{\mathbf{u}}$ and $\tilde{\mathbf{u}}$, which are associated with two layers of degrees of freedom (Dias-da-Costa et al., 2010) as:

$$\mathbf{u} = \hat{\mathbf{u}} + \Psi(\mathbf{x})\tilde{\mathbf{u}}, \tag{2.57}$$

where $\Psi(\mathbf{x})$ is shifted function, and the corresponding finite element approximations are:

$$\hat{\mathbf{u}} = \mathbf{N}(\mathbf{x})\hat{\mathbf{a}}, \tag{2.58a}$$

$$\tilde{\mathbf{u}} = \mathbf{N}(\mathbf{x})\Psi(\mathbf{x})\tilde{\mathbf{a}}. \tag{2.58b}$$

Accordingly, the strain field is written:

$$\varepsilon = \mathbf{L}\mathbf{N}(\mathbf{x})\mathbf{a} = \mathbf{B}(\mathbf{x})(\hat{\mathbf{a}} + \Psi(\mathbf{x})\,\tilde{\mathbf{a}}) \quad in\ \Omega\backslash\Gamma_d \tag{2.59}$$

Where $\mathbf{B} = \mathbf{LN}$ and differential operators are defined in the matrix $\mathbf{L}$:

$$\mathbf{L} = \begin{bmatrix} \partial/\partial x & 0 & 0 \\ 0 & \partial/\partial y & 0 \\ 0 & 0 & \partial/\partial z \\ \partial/\partial y & \partial/\partial x & 0 \\ 0 & \partial/\partial z & \partial/\partial y \\ \partial/\partial z & 0 & \partial/\partial x \end{bmatrix} \tag{2.60}$$

The incremental stress field in terms of nodal displacements is:

$$d\boldsymbol{\sigma} = \mathbf{DB}(d\hat{\mathbf{a}} + \Psi(\mathbf{x})d\tilde{\mathbf{a}}) \;\; in\; \Omega\backslash\Gamma_d \tag{2.61}$$

where $\mathbf{D}$ denotes the constitutive matrix relating incremental stress to incremental strain.

Similarly, the incremental traction vectors at the discontinuity is given by:

$$d\mathbf{t} = \mathbf{T}\, d[\![\mathbf{u}]\!] = \mathbf{TN}\, d\tilde{\mathbf{a}}. \tag{2.62}$$

The discrete form of Equations (2.56a) and Equations (2.56b) reads:

$$\mathbf{K}_{\hat{a}\hat{a}}\, d\hat{\mathbf{a}} + \mathbf{K}_{\hat{a}\tilde{a}}\, d\tilde{a} = d\hat{\mathbf{f}} \tag{2.63a}$$

$$\mathbf{K}_{\tilde{a}\hat{a}}\, d\hat{\mathbf{a}} + (\mathbf{K}_{\tilde{a}\tilde{a}} + \mathbf{K}_d) d\tilde{\mathbf{a}} = d\tilde{\mathbf{f}} \tag{2.63b}$$

where the the arrays of stiffness matrices can be given by:

$$\mathbf{K}_{\hat{a}\hat{a}} = \int_{\Omega\setminus\Gamma_d} \mathbf{B}^T \mathbf{D}\,\mathbf{B}\, d\Omega, \tag{2.64}$$

$$\mathbf{K}_{\hat{a}\tilde{a}} = \int_{\Omega} \mathbf{B}^T \mathbf{D}\,\mathbf{B}\, d\Omega, \tag{2.65}$$

$$\mathbf{K}_{\tilde{a}\tilde{a}} = \mathbf{K}_{\tilde{a}\hat{a}} = \mathbf{K}_{\hat{a}\tilde{a}}{}^T, \tag{2.66}$$

$$\mathbf{K}_d = 4 \int_{\Gamma_d} \mathbf{N}^T \mathbf{T}\,\mathbf{N}\, d\Gamma, \tag{2.67}$$

the internal force vectors are derived as:

$$d\hat{\mathbf{f}} = \int_{\Omega\setminus\Gamma_d} \mathbf{N}^T d\bar{\mathbf{b}}\, d\Omega + \int_{\Gamma_t} \mathbf{N}^T d\bar{\mathbf{t}}\, d\Gamma, \tag{2.68a}$$

$$d\tilde{\mathbf{f}} = \int_{\Omega} \Psi^T \mathbf{N}^T d\bar{\mathbf{b}}\, d\Omega + \int_{\Gamma_t} \Psi^T \mathbf{N}^T d\bar{\mathbf{t}}\, d\Gamma. \tag{2.68b}$$

It is noteworthy $\hat{\mathbf{f}}$ is the internal force usually used in standard finite element, whereas $\tilde{\mathbf{f}}$ enforcing the traction continuity in a weak sense equals zero (Wells and Sluys, 2001a).

2.3.4 Numerical integration

In standard FEM with the polynomial shape functions, Gauss integration scheme in a weak form is efficiently utilised to calculate the stiffness matrix. In the presence of a jump in XFEM framework, the standard Gauss quadrature cannot be sufficient and more considerations over the quadrature of the weak form are required, which are described herein.

Bulk

For XFEM, the integral in Equations (2.65) and (2.66) are extended over the whole element domain Ω. As a result, when an element cut by an interface, the integral over Ω should be split into two subregions Ω^+ and Ω^- as:

$$\begin{aligned} \mathbf{K}_{\hat{a}\tilde{a}} &= \int_{\Omega} \mathbf{B}^T \mathbf{D} \mathbf{B} \, d\Omega \\ &= \int_{\Omega^+} \mathbf{B}^T \mathbf{D} \mathbf{B} \, d\Omega + \int_{\Omega^-} \mathbf{B}^T \mathbf{D} \mathbf{B} \, d\Omega \end{aligned} \tag{2.69}$$

For integration purpose, dividing two subregions into triangular and quadrilateral subgrids that align with a discontinuity is common in XFEM (Belytschko et al., 2001; Moës et al., 1999), the reader my find more information in (Fries and Belytschko, 2010; Khoei, 2014). In triangular method utilised in this thesis, two different approaches can be considered: *i*) the two subregions Ω^+ and Ω^- are divided into triangular domains and the integrals over Ω are decomposed into two sub-integrals (see – Figure 2.5a); *ii*) only the subregion Ω^+ is divided, while the integrals over Ω should be calculated by Gaussian quadrature (see – Figure 2.5b). As an alternative, there are special integration formula for polygons with n edges (Mousavi et al., 2010; Natarajan et al., 2009), which are discussed in details in section 5.3.2.

Discontinuity

In the XFEM, the interface is described implicitly, and the discontinuity is usually simulated by the same shape function as the element shape function according to Equation (2.58b). This simplification leads isoparametric mapping to turn the straight discontinuity on physical element into curved one on the parent element and vice versa (Ventura, 2006), as depicted

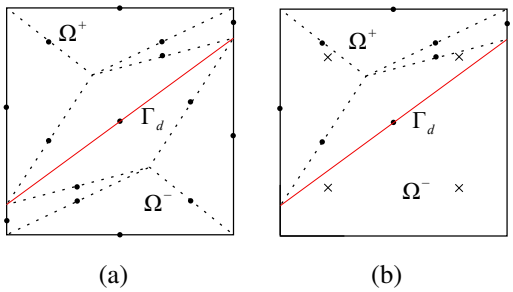

Figure 2.5: Bulk integration scheme for mid-point rule with three point (a) two sub-integrals on Ω^+ and Ω^-, and (b) one sub-integral on Ω^+ and one integral on Ω (the dots and crosses represent the additional and the regular Gaussian integration point respectively).

in Figure 2.6. As a consequence, a straight discontinuity adopted in parent element diverges from the corresponding linear path when it is mapped into the physical element. Moreover, special consideration must be taken in the integration scheme adopted, which may result in oscillatory solutions if high values of the discontinuity stiffness are employed. This issue is thoroughly explored in section 2.4.1.

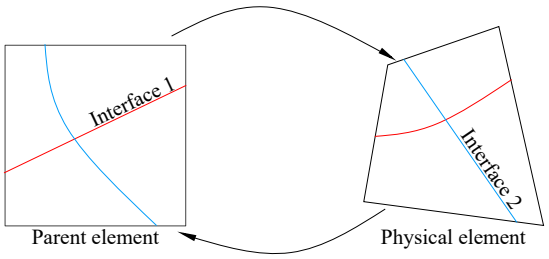

Figure 2.6: Representation of misalignment of the crack path in the parent element and the physical element.

As discussed in section 2.4.1, to avoid spurious oscillation observed in Gaussian rules, a Newton–Cotes/Lobatto scheme is employed (Coutinho et al., 2003; Schellekens and De Borst, 1993; Simone, 2004) to compute the discontinuity stiffness given in Equation (2.67).

Consequently, the integration points adopted are coincident with the additional nodes along the discontinuity to capture the jump.

2.3.5 Difficulties in the XFEM

Each robust method comes with some advantages and disadvantages. Since this thesis aims to revise and modify the XFEM as the product of PUM, the special attention needs to be devoted to the major drawbacks with the XFEM framework despite intensive studies carried out to overcome them in last decades (Babuška and Banerjee, 2012; Fries, 2008; Fries and Belytschko, 2006; Mergheim, 2009). As mentioned earlier, XFEM allows the standard FEM approximation functions to incorporate the arbitrary functions satisfied reproducing condition to make the partition of unity more flexible to model the problems including interface and moving boundary problems. Some difficulties caused by this flexibility can be reviewed in this section.

a) Integrating over discontinuities: conventionally, standard FEM needs smoothness of the integrands while utilising Gauss quadrature in weak form (Fries and Belytschko, 2010). In the presence of a jump in the element local enrichment function, the accuracy of Gauss quadrature further deteriorates. Therefore, as discussed in section 2.3.4, some special consideration should be taken to integrate over the discontinuities.

b) Ill conditioning: incorporating additional function into standard FEM approximation function leads to ill-conditioned stiffness matrix. Various studies have addressed this issue in the literature and proposed different approaches to tackle this shortcoming (Babuška

and Banerjee, 2012; Fix et al., 1973; Menk and Bordas, 2011; Mergheim, 2009). Other methods based on Cholesky decomposition are proposed by Béchet et al. (2005), Fix et al. (1973) and Strang and Fix (1973) to apply on the stiffness matrix, and form the submatrices related to the additional degrees of freedom. This preconditioning induces the numerical instability to be isolated in smaller matrices. In the context of XFEM, Béchet et al. (2005) proposed a preconditioner matrix to solve the linear equation systems easier by focusing on preconditioning the submatrices associated with enriched degrees of freedom. However, this preconditioner matrices are not appropriate for general purposes. Therefore, more investigation is required in this regard. To this end, a new formulation is developed in chapter 4 to decrease the condition number of the stiffness matrix.

c) Increasing degrees of freedom: during the crack propagation process, the enrichment used in XFEM results in the rapid increase of the additional degrees of freedom, which leads to increase the computational cost significantly. Intrinsic XFEM proposed by Fries and Belytschko (2006), using Moving Least-Squares (MLF) method to construct the particular function, where the shape functions of the two subdomains of the cracking domain are coupled by a ramp function. Despite the appealing approach, utilisation of the MLS method is proved exceedingly expensive computationally. As an alternative, an effective strategy in this regard is proposed in chapter 4.

d) Oscillating solutions: the coupling of the degrees of freedom associated with the nodes that are not connected by the element edges, called pathological coupling, causes oscillating solutions in XFEM. Various studies have addressed this phenomenon in the elements utilised in XFEM, also known as PU-based discontinuous elements (Ahmed and Sluys, 2013; Rots,

1988; Schellekens and De Borst, 1993; Simone, 2004), which is detailed in section 2.4. These studies have proposed some approaches to alleviate this difficulty, which are explored in section 2.4.2. However, non of these approaches can be considered as a general treatment, and only can be used in special conditions. An innovative formulation is developed in chapter 5 to surmount the spurious behaviour in XFEM framework.

2.4 Partition of unity-based discontinuous elements

To treat problems involving discontinuities, interface elements or embedded discontinuity elements are utilised to incorporate the displacement jumps into standard finite elements (Alfano and Crisfield, 2001; Goodman et al., 1968; Saouma et al., 1990) conventionally. Generally, the relative displacements of the nodes located at two sides of the discontinuity determine the displacement jump when using the interface elements approach (Bittencourt et al., 1996), whereas an incompatible strain mode plays the role of displacement jump incorporating into an element in embedded discontinuity approach (Simo et al., 1993).

The family of enrichment methods using the PU (including XFEM) can be considered as another alternative, introducing a category of elements, called PU-based discontinuous elements (Simone, 2004), kinematically similar to interface elements. As a consequence, the stiffness matrix of these widely-used elements (Moës et al., 1999; Remmers et al., 2003; Simone et al., 2003; Wells and Sluys, 2001a) can be examined according to the interface elements concept (Schellekens and De Borst, 1993) to clarify the weakness and improve their application.

2.4.1 Computational issue

In this section, the stiffness matrix of the conventional interface elements is considered to clarify the weakness of PU-based discontinuous elements. Since this type of elements is not the main focus of this thesis, a brief summary of the stiffness matrix of the conventional interface element is presented herein. The reader may find further information in (Goodman et al., 1968; Kaliakin and Li, 1995; Schellekens and De Borst, 1993).

Interface element behaviour

The stiffness matrix of interface element with n-node (see – Figure 2.7) is given by:

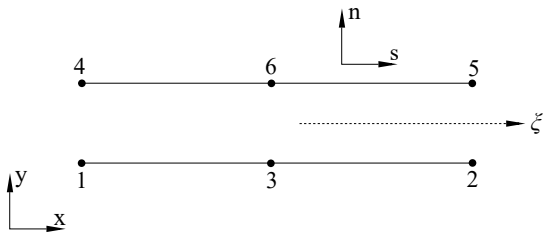

Figure 2.7: Conventional interface element.

$$\mathbf{K}_d = b \int_{\xi=-1}^{\xi=+1} \mathbf{B}^T \mathbf{D} \mathbf{B} \frac{\partial x}{\partial \xi} \mathrm{d}\xi \tag{2.70}$$

where b denotes interface width and $\mathbf{B}$ is $2 \times 2n$ matrix as:

$$\mathbf{B} = \begin{bmatrix} -\mathbf{N} & \mathbf{N} & \mathbf{0} & \mathbf{0} \\ \mathbf{0} & \mathbf{0} & -\mathbf{N} & \mathbf{N} \end{bmatrix} \tag{2.71}$$

where $\mathbf{N}$ is isoparametric shape function as:

$$\bar{\mathbf{N}} = \begin{bmatrix} N_1 & N_2 & N_3 & N_4 \end{bmatrix} \tag{2.72}$$

and constitutive matrix in local coordinate s, n is written:

$$\mathbf{D} = \mathbf{R}\mathbf{T}\mathbf{R}^T \tag{2.73}$$

where $\mathbf{R}$ denotes the rotation matrix and $\mathbf{T}$ is the traction-separation relation as:

$$\mathbf{T} = \begin{bmatrix} d_s & 0 \\ 0 & d_n \end{bmatrix} \tag{2.74}$$

where d_s and d_n are constant. For the element represented in Figure 2.7, since global and local coordinates are coincident, $\mathbf{D} = \mathbf{T}$.

Expanding $\mathbf{BDB}^T$ for linear/quadratic interface element leads to:

$$\mathbf{BDB}^T = \begin{bmatrix} \mathbf{K}_n & \mathbf{0} \\ \mathbf{0} & \mathbf{K}_s \end{bmatrix} \tag{2.75}$$

where $\mathbf{K}_i$ is written as:

$$\mathbf{K}_i = d_i \begin{bmatrix} \bar{\mathbf{k}} & -\bar{\mathbf{k}} \\ -\bar{\mathbf{k}} & \bar{\mathbf{k}} \end{bmatrix}, \quad i = s, n \tag{2.76}$$

The matrix $\bar{\mathbf{k}}$ for linear interface element is given by:

$$\bar{\mathbf{k}} = \begin{bmatrix} N_1^2 & N_1 N_2 \\ N_1 N_2 & N_2^2 \end{bmatrix} \tag{2.77}$$

In linear interface element, the results obtained from the Gaussian quadrature is coincident with the analytical integration and both of which lead to the full matrix. In contrast, nodal integration (i.e. the Newton-Cotes rule) removes the coupling terms $N_i N_j$ while $i \neq j$, also called pathological coupling. It is noteworthy that the same behaviour is observed in quadratic interface elements.

This coupling is considered as the reason behind the traction oscillation by Kaliakin and Li (1995), Rots (1988), Schellekens and De Borst (1993) and Simone (2004). These studies reveal that smoothing the response is usually observed employing the Newton-Cotes rule. Although the overintegration with the Newton-Cotes rule leads to pathological coupling, the element is less vulnerable to spurious oscillation in this case (Schellekens and De Borst, 1993). For the Gaussian integration, Coutinho et al. (2003) points out the spurious kinematical inconsistency in the conventional interface element proposed by Goodman et al. (1968). The oscillation in the displacement field causes the oscillation in the stress field, which increases when the higher penalty parameter used for the interface.

Some authors (Day and Potts, 1994; Schellekens and De Borst, 1993) relate the high gradient of stress occurring in the neighbourhood of interfaces to the oscillating behaviour. Therefore, mesh refinement can mitigate the spurious oscillation in stress profile (Kaliakin and Li, 1995). In fact, in two dimensions, if the sufficiently refined mesh is provided, trapezoidal and

Simpson rules lead to accurate linear and quadratic solutions, respectively (Kikuchi and Oden, 1988).

Structural behaviour

According to Simone (2004), the PU-based discontinuous elements are examined based on the linear elastic test for interface elements proposed by Rots (1988). As described in section 2.2, the traction vector of the discontinuity has a relation with displacement jumps, shear and normal penalties, denoted by k_s and k_n respectively. As represented in Figure 2.8a, a single notched beam with the activated horizontal jump is considered. A traction-free discontinuity ($k_n = k_s = 0$) is assumed as the notch, whereas a high value indicating perfect contact between two faces of the discontinuity is considered for the stiffness of the interface.

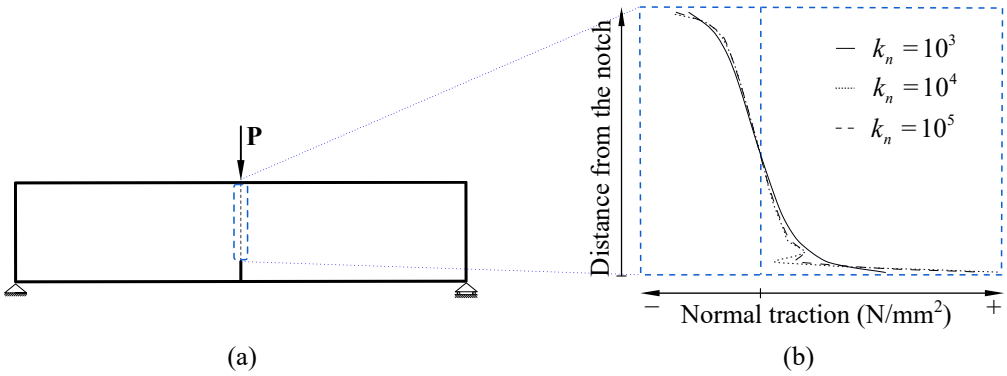

Figure 2.8: Traction-free notched beam test: (a) Schematic geometry (b) Traction profile oscillations (k_n measured in $\frac{\text{MPa}}{\text{mm}}$).

As depicted in Figure 2.8b, the results obtained by Simone (2004) indicate that the normal component of the traction profile at the discontinuity is dependent on the interface stiffness and the numerical integration approach, which has a complete agreement with the results reported by Remmers et al. (2001) and Rots (1988) regarding conventional interface element.

Particularly, the results of using the high-value penalty as normal stiffness for perfect bounded interface reveal that: i) Gauss integration scheme leads to remarkable oscillations in the normal tractions profile, regardless of the adopted mesh type (e.g. structured or unstructured mesh) ii) nodal integration scheme (e.g. trapezoidal rule) leads to improvement of traction profile compared to the Gauss quadrature counterpart (Remmers et al., 2001; Rots, 1988; Schellekens and De Borst, 1993; Simone, 2004).

On the other hand, Ahmed and Sluys (2013) investigated the effect of the quadrilateral finite elements on displacement jump approximation. Since the quadrilateral finite element can be categorised as the family of the PU-based discontinuous elements, the results reported regarding the spurious oscillation occurring in traction profile along with the discontinuity show agreement with previous studies (Schellekens and De Borst, 1993; Simone, 2004). Besides, Ahmed and Sluys (2013) indicates that the bilinear approximation function has a severe effect on displacement jump calculated at the discontinuity, leading to unrealistic strain field and consequent inaccurate nodal displacements in a simple example of one-element structure.

Since one of the main ingredients of the cohesive zone models utilised in the strong discontinuity approaches can be characterised by traction profile, the unrealistic oscillations occurring in traction forces are required to be explored. In a similar context, the spurious displacement jump of the quadrilateral finite element is investigated in the following section.

2.4.2 Alleviation of spurious behaviour

Since the spurious behaviours of the PU-based discontinuous elements has remained a dilemma in the scope of enrichment methods, the two approaches can be utilised to alleviate these phenomena are reviewed in this section.

Treatment by Simone (2004)

According to Equation (2.67), the stiffness of the discontinuity in partition of unity based discontinuous element with 4 nodes can be given by:

$$\mathbf{K}_d = \int_{\Gamma_d} \mathbf{N}^T \mathbf{R}\,\mathbf{T}\,\mathbf{R}^T \mathbf{N}\, d\Gamma = b \int_{\xi=-1}^{\xi=+1} \mathbf{N}^T\,\mathbf{T}\,\mathbf{N} \frac{\partial x}{\partial \xi}\, d\xi \tag{2.78}$$

where the transformation matrix $\mathbf{R} = \mathbf{I}$ for the discontinuity located at a element horizontally as represented in Figure 2.9, b denotes the interface width, and $\mathbf{N}$ is 2 by 2 matrix:

$$\mathbf{N} = \begin{bmatrix} \bar{\mathbf{N}} & 0 \\ 0 & \bar{\mathbf{N}} \end{bmatrix} \tag{2.79}$$

where the arrays of matrix diagonal contains elements isoparametric shape function as represented in Equation (2.72).

Expanding the integrand of Equation (2.78) leads to:

$$\mathbf{N}^T\,\mathbf{T}\,\mathbf{N} = \begin{bmatrix} \bar{\mathbf{K}}_n & 0 \\ 0 & \bar{\mathbf{K}}_s \end{bmatrix} \tag{2.80}$$

where $\bar{\mathbf{K}}_n = k_n\bar{\mathbf{K}}$, $\bar{\mathbf{K}}_s = k_s\bar{\mathbf{K}}$ according to Equation (2.17), and $\bar{\mathbf{K}}$ reads:

$$\bar{\mathbf{K}} = \begin{bmatrix} N_1^2 & N_1N_2 & N_1N_3 & N_1N_4 \\ N_2N_1 & N_2^2 & N_2N_3 & N_2N_4 \\ N_3N_1 & N_3N_2 & N_3^2 & N_3N_4 \\ N_4N_1 & N_4N_2 & N_4N_3 & N_4^2 \end{bmatrix} \tag{2.81}$$

As depicted in Figure 2.9a and according to Equation (2.81), the trapezoidal rule integration

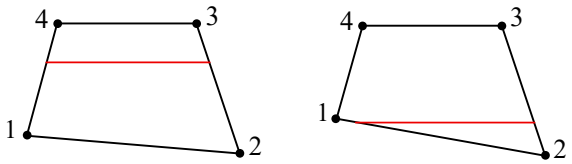

Figure 2.9: Different possibilities of horizontal discontinuity placement in quadrilateral element

scheme activates the natural coupling occurring between two sets of neighboring nodes 1-4 and 2-3, whereas the pathological couplings (e.g. N_1N_2, N_1N_3 etc) are removed. For Figure 2.9b, Gauss quadrature actives all coupling between node 2 and the rest of the nodes, where the activated pathological coupling leads to the unrealistic oscillation at traction profile. The trapezoidal rule can cancel some pathological coupling in Figure 2.9b, which results in the traction oscillation less pronounced. However, since some pathological couplings remain unchanged, the trapezoidal rule cannot be effective in all conditions. As a consequence, a more reliable approach is required to treat the difficulties caused by pathological coupling while utilising this class of elements. To this end, the following section is devoted to another treatment proposed in this regard.

Treatment by Ahmed and Sluys (2013)

As discussed in section 2.3, XFEM and FEM share the concept of transferring the forces and surface tractions to the nodes and utilise element shape functions to approximate the displacement. Since the displacement jump can be obtained along the discontinuity using the additional degrees of freedom in XFEM, the traction forces between two faces of the discontinuity should be transferred to the nodes by Equation (2.67). In elements with bilinear shape functions, the contribution of the forces at a node is considered based on the same approximation functions. As a result, constant traction at the discontinuity can lead to unequal nodal forces, satisfying the force equilibrium, not the moment equilibrium. Consequently, the spurious moment couple causes the interface to rotate unrealistically. The single element test (see – Figure 2.10) done by Ahmed and Sluys (2013) reveals that some results in (Simone, 2004) cannot remain valid if the interface direction changes. The main results can be concluded as below:

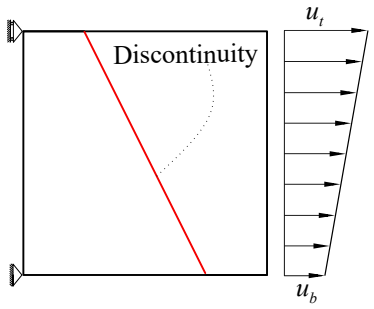

Figure 2.10: Single element test.

i) According to Equation (2.63b), $\mathbf{K}_d$ can be directly affected by displacement jump transferred to the element nodes. Consequently, the interpolation function adopted for the discontinuity jump contaminates global stiffness matrix, leading to inaccurate nodal values. Since

internal force $\tilde{\mathrm{f}}$ is affected accordingly, using the higher penalty stiffness increases the solution error as reported in (Dias-da-Costa et al., 2010; Simone, 2004).

ii) Using the nodal integration scheme (e.g. trapezoidal rule) cannot construct a constant strain field For $u_b = u_t$. Since displacement field is approximated by the bilinear functions, the unrealistic linear strain field is observed over the element.

iii) Gauss integration scheme leads to reliable results for uniform crack opening. For nonuniform crack opening ($[\![\mathbf{u}]\!]_n \neq 0$, $[\![\mathbf{u}]\!]_s \neq 0$), bilinear approximation causes spurious opening when the tangential and normal components to the discontinuity surface are not along with local axes of the element. The observation reveals that the Newton-Cotes/Lobatto integration scheme deteriorates the results in the latter case because of underintegration compared to Gauss integration scheme.

According to the results concluded, mesh refinement around the discontinuity can be considered as the only remedy proposed by Ahmed and Sluys (2013) for spurious displacement jump and interface rotation of bilinear quadrilateral elements. In fact, mesh refinement causes the unbalanced moment occurring at the interface to decrease. The reduction of the moment magnitude results in smaller spurious displacement, leading to more accurate approximation and consequent the solution.

To sum up, all treatments proposed in the literature for the spurious behaviour occurring in the PU-based elements seem occasional. In fact, since the crack path is unknown *a priori* in crack propagation analysis, the mesh refinement cannot be utilised around the interface region. Furthermore, the mesh refinement has a high cost numerically. On the other hand,

using the nodal integration are limited to the special conditions reviewed in this section. As a consequence, this class of elements need to be treated by a holistic approach. In chapter 5, a new approach is introduced to surmount all these difficulties.

2.5 Conclusions

In this chapter, a general framework for strong discontinuities in the scope of discrete crack approach is given. The link required between the continuous and discontinuous parts of the domain (e.g. discontinuity and bulk respectively) is justified, and the significance of the criterion used to initiate and propagate the discontinuity is clarified. Accordingly, chapter 3 is devoted to this matter.

Moreover, the particulars of XFEM as the product of PUM is discussed, which reveals that XFEM, as a robust framework to solve the problems involving discontinuities, suffers from some serious shortcomings, two of which are:

- increase of stiffness matrix bandwidth during the analysis, caused by the degrees of freedom progressively added to the system of equations due to the crack propagation.
- spurious behaviour obtained by utilising PU-based discontinuous elements, resulting from the unsatisfied moment equilibrium because of pathological coupling between degrees of freedom of corresponding elements.

In chapters 4 and 5, two new formulations are introduced in which these two drawbacks are overcome.

CHAPTER 3

A comparative study on crack propagation criteria

Cracking initiation and crack propagation play a central role in embedded discontinuity approaches. The cracking simulation has a significant impact on the energy balance in the cohesive zone utilised to solve the non-linear equations. Also, as a crack is represented by a discontinuous displacement in fracture mechanics, the prediction of crack trajectories determines the accuracy of the nodal displacements obtained by numerical analysis. Consequently, the criteria used to trace the crack path may dominate the numerical results. Therefore, this chapter 3 focuses on crack propagation criteria used in the discrete crack approach as a well-suited approach to analyse problems with structures showing a single dominant crack (e.g. pull-out test). To this end, in this chapter, three different cracking surfaces and an averaged stress-based criterion available in the literature are thoroughly analysed and assessed. A contribution of selecting the most suitable approach is given, depending on the dominant fracture mode in the problem at hand.

Three cracking criteria based on failure surfaces adopted as a crack initiation criterion required to link the bulk to a discontinuity (see – section 2.2.1) are reviewed in section 3.1 and further information regarding crack propagation obtained from these criteria is given. In section 3.2, an approach is almost used in continuum-based models is introduced. In section 3.3, a

comparison between different failure surfaces in terms of crack initiation performance is drawn, and some critical considerations regarding crack propagation in discrete crack approach are taken into account in section 3.4. The several benchmark tests on mode I, mixed-mode and pure compressive fracture are chosen in section 3.5 to reveal the abilities of each cracking criteria.

3.1 Cracking criteria based on failure surfaces

This section aims to briefly review the crack initiation and propagation criteria, which can be utilised in the discrete crack approach.

3.1.1 Principal stress

The principal stress criterion, also known as the Rankine criterion, is based on the maximum stress and its direction. This criterion assumes that a crack in a uniaxial stress state would initiate when the maximum principal stress reaches the tensile strength of the material. This crack propagates orthogonally to the uniaxial tensile stress (Wang and Shrive, 1995), which is perpendicular to minimum principal stress. The stress field at the tip of the crack may not have enough resolution in the discrete crack approach, which is why the local stress may not provide a reliable criterion to obtain the direction of the propagating crack. In addition, Jirásek and Zimmermann (2001) shows that a non-local measurement can be more reliable prediction to trace the crack path. Therefore, the axis of the maximum principal of average

stress tensor is considered as the normal vector to the crack. To this end, a Gaussian weight function (Wells and Sluys, 2001a) smoothing the crack tip stresses is defined as follows:

$$\omega = \frac{1}{(2\pi)^{3/2} l^3} \exp\left(-\frac{r^2}{2l^2}\right), \tag{3.1}$$

where ω represents the integration weight, r is the distance of respective integration point from the tip of the discontinuity, and l determines the specific distance around the tip. Previous studies propose different values for l. Dias-da-Costa et al. (2009) suggests the length scale parameter, which is about 1% of the Hillerborg's characteristic length l_{ch}, defined by :

$$l_{ch} = \frac{G_F E}{{f_t}^2}, \tag{3.2}$$

where G_F is Griffith's energy, E is Young's modulus, and f_t represents the tensile strength. Other authors suggest a value of the of four times the length scale for a gradient-enhanced damage model (Simone et al., 2003), whereas Wells et al. (2002) proposes $2-3$ times greater than the characteristic element size h, which is considered in this chapter.

Note that, in spite of the fact that principal stress criterion is acceptable for fracture mode I, it has been used in previous studies for various fracture modes (Dias-da-Costa et al., 2009; Meschke and Dumstorff, 2007). However, results show that this criterion may fail to provide reasonable results for mixed-mode failure. In this case, more suitable failure surface may be required to capture the combined effect of compression and tension states leading to more

accurate prediction of propagation. To this end, some modified failure pockets are introduced in the following sections.

3.1.2 Mohr-Coulomb's failure surface

Generally, the failure surface models assume that a crack initiates when the stresses in the traction space $t_n - t_s$ reach a specific value, satisfying $f(t_n, t_s) = 0$.

Recently, Saloustros et al. (2015) suggested a crack-tracking technique previously used in the smeared crack approach. This technique is the combination of three failure surfaces, Mohr-Coulomb, Tresca and Rankine, where some considerations are employed to define the crack propagation path. The discontinuity is assumed to initiate when an integration point satisfies any of the criteria adopted (i.e. Mohr–Coulomb, Tresca and Rankine). To this end, the following representation using principal stresses can be utilised as:

$$f(\sigma_1, \sigma_2) = \frac{\sigma_1}{f_t} - \frac{\sigma_2}{f_c} - 1 = 0, \quad \sigma_1 \geq \sigma_2, \tag{3.3}$$

where, σ_1, σ_2 and σ_3 denote principal stresses; f_t and f_c represent tensile and compressive strength respectively.

Several conditions may occur on the plane stress, which may lead to the different need to consider uniaxial tensile or compression states, the biaxial compression state, and combination of tensile and compression states (intermediate state). To clarify these states, some different conditions are presented in Figure 3.1. In point A, mode-I fracture occurs, and the discontinuity propagates along the normal vector to maximum principal stress (σ_{I}), whereas

if the crack initiates when Mohr–Coulomb's failure criterion is satisfied, the crack initiation occurs for values probably much greater than f_t, which is not reasonable.

For higher values of the compressive stress, this value may vary to B (see – Figure 3.1), which is quite different from what occurs in mode-I fracture and Rankine criterion cannot handle that situation. The Mohr-coulomb failure pocket cannot be applied as a single cracking surface due to the lack of a tensile cap. As a result, this failure envelop has to be used by Rankine as a tensile cap otherwise the Mohr-coulomb cannot predict the crack trajectories in either fracture mode I or mixed-mode fracture appropriately. The interested reader may refer to (Saloustros et al., 2015) studying the Mohr-Coulomb criterion in detail.

The modified failure envelops, suggested in the current work to trace the crack path are mature enough to determine the crack initiation and propagation independently, without other considerations. From the crack propagation point of view, Mohr–Coulomb's law assumes a linear relation between compressive tractions and shear, which cannot capture a smooth transition between compressive and tensile tractions (Alfaiate and De, 2004). Naturally, a more realistic failure surface is required to overcome or at least alleviate the shortage. To this end, two more complex failure surfaces are investigated in the following sections.

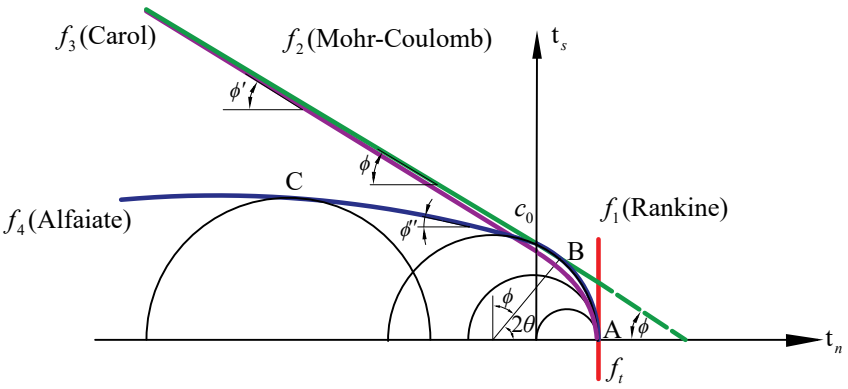

Figure 3.1: Failure surfaces.

3.1.3 Normal/shear cracking model (Carol's failure surface)

The shape of cracking surface proposed by Carol et al. (1997) is indicated in Figure 3.1, represented by a hyperbola as:

$$f = t_s^2 - (c - t_n \tan\phi)^2 + (c - f_t \tan\phi)^2, \tag{3.4}$$

where c, f_t and ϕ denote the cohesion strength, the tensile strength and the internal friction angle respectively.

The proposed hyperbolic surface is limited by two cases of crack initiation: mode-I, obtained when the surface is parallel to the horizontal axis, and cracking under shear and high value of compression, which tends towards the Mohr-Coulomb's failure surface. In contrast to the Mohr-Coulomb's failure surface, nonlinear tensile and shear strength are introduced by Carol's failure surface. The hyperbola can provide a smooth transition in intermediate states (mixed-mode fracture), overcoming the difficulty in Mohr-Coulomb's friction law. To predict the crack propagation orientation, the normal to the discontinuity is determined by angle θ

relative to maximum principal stress axis, which is given by:

$$\theta = \frac{1}{2}(\pi/2 - \phi'), \tag{3.5}$$

where ϕ' reads as:

$$\tan\phi' = \left|\frac{\partial t_s}{\partial t_n}\right|. \tag{3.6}$$

Since this hyperbola tends towards Mohr-Coulomb's failure surface for a high value of the normal compressive traction, the lack of appropriate cap for this state remains unchanged. To overcome this shortcoming, another modified failure surface proposed for quasi-brittle materials is presented next.

3.1.4 Alfaiate's cracking surface

All failure surfaces mentioned earlier face some difficulties to describe initiation and/or propagation of strong discontinuities. The Rankine criterion is not capable of capturing mixed-mode cracking, whereas the Mohr-coulomb criterion provides inaccurate predictions for high compression stress and cannot be used as a single surface properly. In addition, the linear nature of the surface causes non-smooth transition between tensile and compressive tractions, whereas Carol's failure hyperbolic surface introducing the smooth transition for tensile and compressive tractions requires a more reliable cap for high compression state.

Alfaiate et al. (2002) proposed a failure surface to tackle all these shortages. To this end, a surface in the stress vector space of the discontinuity $t_n - t_s$ has been introduced such that Rankine and modified Mohr-coulomb's friction law are considered as the two caps (see –

Figure 3.1). The failure surface adopted is given by:

$$f = t_s^2 - \frac{f_t^2 + 2c\tan\phi f_t - c^2}{f_t^2} t_n^2 - c^2(1+\tan^2\phi) + (t_n + c\tan\phi)^2 = 0, \tag{3.7}$$

where ϕ, c and f_t are the internal friction angle, the cohesion and the tensile strength. Alfaiate's failure surface can be considered as a modified Mohr-Coulomb's failure surface, whose derivatives are continuous in the traction space, allowing for the smooth transition between mode-I and mode II fracture. Experimental observations reveal that mixed-mode cracking usually leads to mode-I crack initiation unless normal traction with high compression values is considered. Note that, Equation (3.6) is utilised, similar to Carol's failure surface, to obtain the crack direction in the normal traction with high compression.

3.2 Criterion based on the averaged effective stress tensor

The previous studies showed that stress-based criteria used to predict the crack direction in the discrete cracking approach may face two shortages. First, (Jirásek and Zimmermann, 2001) showed that local measures may not provide a reliable prediction of crack paths. Second, the observation on both mode I and mode II failures reveal that the effective stress is an appropriate predictor of the strain localisation (Wells et al., 2002). To this end, Wells et al. (2002) and Wells and Sluys (2001a) introduce Equation (3.1) to alleviate the effect of local measurement, and an averaged stress-based model, which is given by:

$$\mathbf{d}_{\Gamma_d} = \sum_{i \in S} \sigma_i V_i \omega_i \frac{\mathbf{d}_i}{\|\mathbf{d}_i\|} \tag{3.8}$$

where S denotes the set of integration points i located in circular sector represented in Figure 3.2 with the averaged effective stress σ_i, the volume V_i, the weight ω_i calculated by Equation (3.1), and the vector in direction of these points denoted by $\mathbf{d}_i$. Note that the maximum accumulation of the averaged effective stress direction in a circular sector of 90° (Simone et al., 2003) or 180° (Wells et al., 2002) at the front of discontinuity tip region is considered to calculate the trajectory of discontinuity propagation.

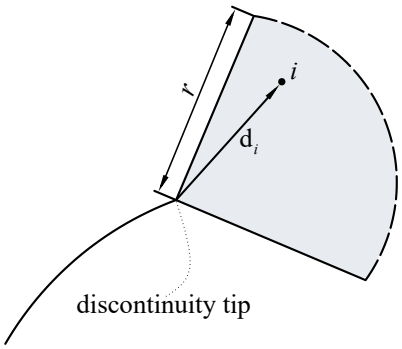

Figure 3.2: Determination of the propagation direction.

3.3 Crack initiation

In this section, four failure surfaces are compared from the initiation point of view. Note that, the averaged stress-based criterion cannot provide any failure surface and one of the failure surfaces mentioned in section 3.1 is required to allow this model to be adopted.

Four main conclusions can be drawn:

1. For a low compressive normal traction, all failure surfaces, except Rankine, lead to almost the same traction components. As mentioned earlier, the Mohr-Coulomb surface should be considered as an auxiliary surface to Rankine for mixed-mode fracture analysis.

2. For a low compressive normal traction, Carol's failure surface can provide a conservative estimate compared to Mohr-coulomb's surface. In addition, Carol's pocket can provide a smooth transition between mode-I and modeII fracture because of the continuous derivatives in the traction space. For high compressive normal traction state, Carol's failure surface tends to Mohr- coulomb failure envelop, which is inappropriate to obtain accurate failure surface. As a remedy, a modified failure surface introduced by Alfaiate and De (2004) can be adopted.

3. In both high and low compressive normal traction, Alfaiate's provides the most suitable cracking surface.

4. An increase of cohesion strength leads to narrow the difference between cracking surfaces on low compressive normal traction state (Saloustros et al., 2015). Hence, the Mohr-coulomb criterion is more efficient for brittle materials with high cohesion strength in low compressive normal traction state.

3.4 Crack propagation

To propagate the discontinuity in the strong discontinuity approaches, including XFEM, some considerations should be taken into account as briefly discussed herein.

As a discontinuity crosses through an element straight, the crack tip always lies on the element edge. The crack initiation criteria discussed in section 3.1 are required to evaluate the onset of the localisation at the crack tip and the corresponding discontinuity path. To this end, some criteria may be followed as below:

i) The stress state considered for crack evolution is defined by the mean values of the stress components at the nearest integration points of the crack tip (Alfaiate et al., 2003).

ii) As discussed earlier, a non-local stress state should be utilised to define the averaged field beyond the element size (Wells and Sluys, 2001a). To this end, a Gaussian weight function in Equation (3.1) smoothing the crack tip stresses should be adopted.

iii) The studies conducted in LEFM and cohesive cracks models (Areias et al., 2009; Ma et al., 1999) indicate that the crack path can be obtained from the relation between normal and shear opening jump components.

iv) The direction of the propagation is determined at the initiation time, using the initiation criteria described in section 3.1. The failure surface is not reached in the bulk and at the crack tip simultaneously because the traction continuity is enforced in a weak manner. Therefore, a discontinuity is introduced in the earlier stage in order to prevent traction field and bulk lying outside the cracking surface (Dias-da-Costa et al., 2009).

In the following section, four structural examples are presented to clarify the effect of proposed cracking criteria on crack initiation and propagation.

3.5 Numerical examples

In this section, the differences between the approaches described in section 3.1 and section 3.2 are studied using four different benchmark tests. The first test is adopted to investigate the performance of the different criteria in the pure tensile state in fracture mode I. The L-shaped panel test, proposed by Winkler (2001) representing the curved crack path in fracture mode-I is studied to clarify i) the differences between conventional cracking surface and modified ones ii) the averaged stress-based criterion sensitivity to the parameters used in the averaging techniques introduced by Wells et al. (2002). The third test is the mixed-mode three-point bending benchmark test studied by John and Shah (1990), which reveals that the robustness of modified cracking surfaces in mixed-mode fracture compared to principal tensile stress criterion often used in fracture mechanics. The uniaxial compression test introduced by Van Geel (1998) shows that modified cracking surfaces are capable of being used in the compressive state, representing the robustness of modified failure surfaces and their superiority over conventional ones. For all analysis, the problems are discretised by four-node elements with bilinear interpolation functions and the traction-separation law by Mariani and Perego, 2003, described in section 2.2 is employed.

3.5.1 Three point bending beam test

The first example is the three point bending beam tested by Bazant, Pfeiffer et al. (1987), with a span and thickness equal 762 mm and 38 mm respectively. A notch (25.4 ×50.8 mm) is considered at the bottom of the midspan, as represented in Figure 3.3.

The material properties of the specimen are taken as: Young's modulus E= 27413 MPa, Poisson ratio ν = 0.18, tensile strength f_t =2.886 MPa, compressive strength f_c=34 MPa, and fracture energy G_F = 0.04029 N/mm. The finite element model is discretised by 370 bilinear finite elements, and a total load of 10 kN is exerted at the middle of the upper part of the beam, as seen in Figure 3.3.

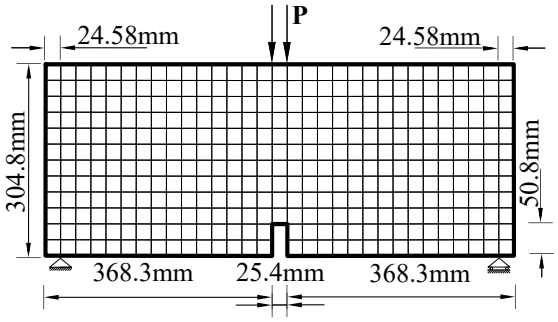

Figure 3.3: Three point bending beam.

In Figure 3.4, the displacement-load curves obtained from four approaches studied show the similarity as expected. Figure 3.5 represents two snapshots of the stress field σ_{xx} for three point bending test beam while the vertical displacement of the loaded node is u_y=0.08 mm and u_y = 0.1 mm. Since all of the criteria represent the similar deformation and consequent similar stress field and crack direction, the stress map of averaged stress criterion is represented, and the rest of the criteria results are omitted. As described in section 3.1.1, the length parameter l used in the averaging stress criterion should be 2-3 times greater than the characteristic element size h. Note that, the length parameter determines how fast the weight function decays from the discontinuity tip, which can have a significant effect on the crack path predicted by this approach. Accordingly, the sensitivity to the length parameter is investigated here. As represented in Figure 3.6, the sensitivity of the averaged stress criterion in terms of length

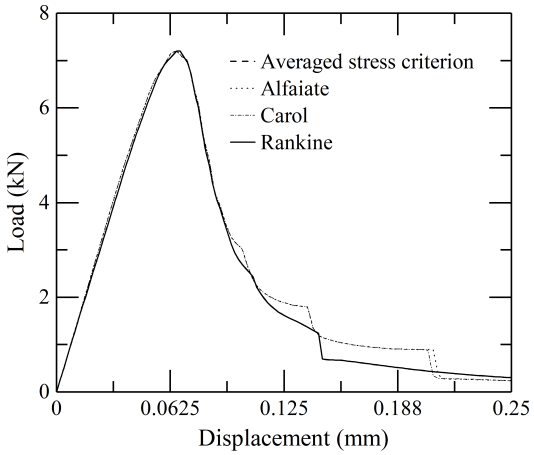

Figure 3.4: Three point bending beam: load–displacement curves for the loaded node, obtained from studied criteria including averaged effective stress, Alfaiate's, Carol's and Rankine.

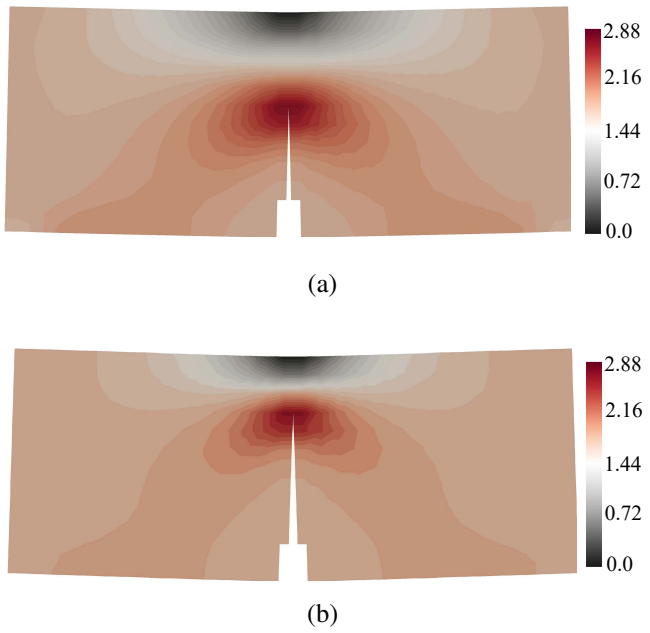

Figure 3.5: Stress field σ_{xx} in MPa for averaged effective stress criterion when the vertical displacement of the loaded node is (a) u_y=0.08 mm; (b) u_y= 0.1 mm.

parameter, taken 2.2, 2.6 and 3 times greater than the characteristic element size are studied. The results indicate that the averaged effective stress approach is not sensitive to the different length parameters given within the range recommended for this example.

The important conclusion is that there is a substantial similarity between all approaches in the pure tension example. Even in the averaged stress criterion with different length parameters, the crack propagation results are similar, and the structure load-displacement responses are practically coincident.

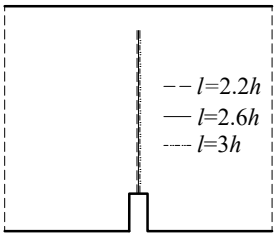

Figure 3.6: Sensitivity to the length parameter for three point bending beam test.

3.5.2 L-shaped panel test

In this section, the L-shaped panel experimentally tested by Winkler (2001) is simulated as a problem with the curved crack path. The geometry of the panel is depicted in Figure 3.7, where the bottom of the panel is fully fixed and a vertical force P=10 kN is applied at the distance of 225 mm from the middle surface of the specimen. The following material parameters are taken: Young's modulus E=25.85 GPa, Poisson ratio ν = 0.18, tensile strength f_t =2.70 MPa, and fracture energy G_F= 0.095 N/mm (Winkler, 2001). The adopted mesh represented in Figure 3.7 consists of 300 bilinear finite elements, and plan stress state is assumed. In Figure 3.8, the crack paths predicted by different criteria are represented. As observed, the Rankine criterion cannot trace the crack path at the first steps, which renders this benchmark test challenging for many studies in fracture mechanics based on the direction of maximum principal stress (Rankin failure surface) as the normal vector to crack direction.

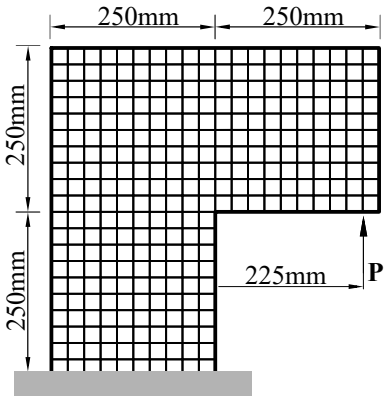

Figure 3.7: L-shape panel: geometry, boundary conditions and finite element mesh.

The modified cracking surfaces, Alfaiate's and Carol's, are able to predict the crack direction in a more realistic way until the last steps of the analysis. Although these modifications cannot exert a significant influence on the displacement-load curve of the structure (see – Figure 3.9), they allow the structure to experience the softening state properly. The criteria fail to trace the crack path when the crack approaches left vertical surface of the panel. Figure 3.10 reveals the similarity between Alfaiate's and Carol's cracking surfaces in σ_{xx} stress field and their difference with Rankine cracking surface in the last stages of analysis.

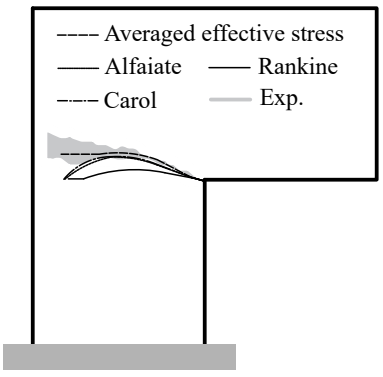

Figure 3.8: L-shape panel: Comparison of crack path traced by different approaches.

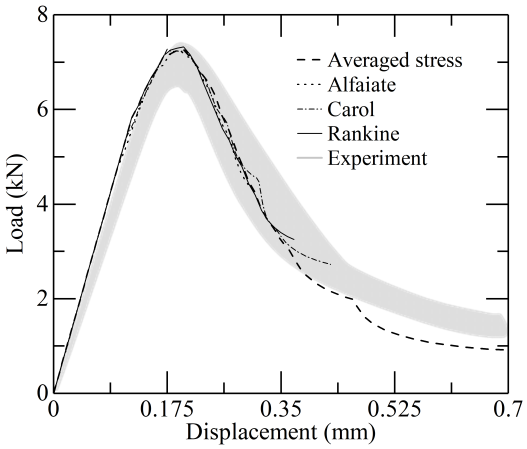

Figure 3.9: L-shaped panel: load–vertical displacement curves at the loaded node for Averaged effective stress criterion, Alfaiate's, Carol's and Rankine cracking surfaces.

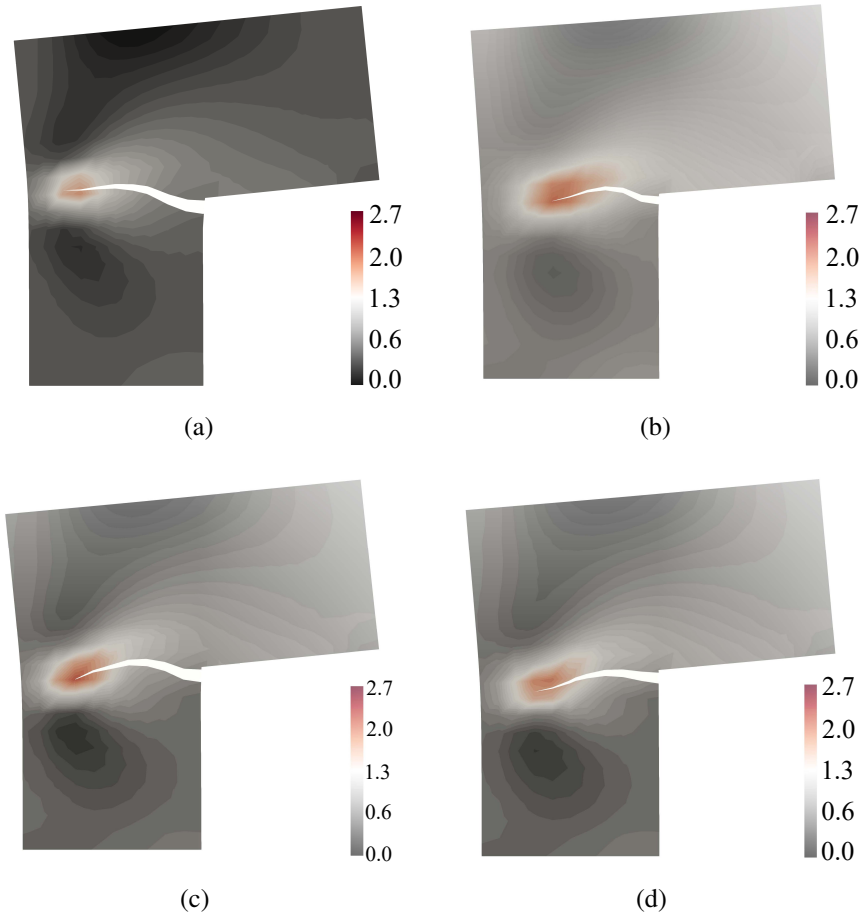

Figure 3.10: Stress along x-axis for L-shaped panel: for (a) Averaged effective stress (b) Alfaiate (c) Carol (d) Rankine in u_y=0.35 mm.

The averaged stress criterion shows a good agreement with experimental results and provides the most approximated crack path in Figure 3.8. As represented in Figure 3.9, the load-displacement curve of averaged effective stress criterion also confirms the performance of this approach. The structural deformation during the softening, while force drops to 30kN from the peak reveals the difference between averaged effective stress criterion results compared with the other approaches.

To assess the sensitivity of averaged effective stress criterion to the length parameter, values of 2.2, 2.6 and 3 times greater than the characteristic element size are investigated. As represented in Figure 3.11, the averaged effective stress criterion is quite sensitive to this parameter length. Note that, this sensitivity is even more noticeable for an unstructured mesh where the characteristic element size adopted to calculate the length parameter changes repeatedly locally while the active crack propagates through the different elements. Accordingly, the sensitivity to the length parameter also leads to mesh sensitivity, which is why this criterion may not be reliable enough to trace the crack direction despite the good results in some cases. This is why the averaged stress criterion is not applied in the next examples.

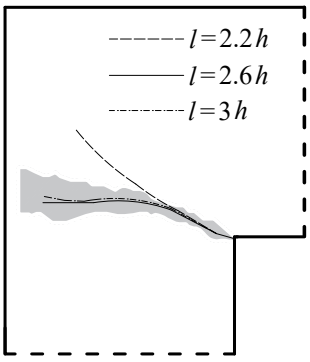

Figure 3.11: The sensitivity of averaged effective stress criterion to the length parameter characterised by the characteristic element size h for L-shape panel.

3.5.3 Mixed-mode three-point bending test

The mixed-mode three point bending beam tested by John and Shah (1990) is one of the benchmark tests available for crack tracking criteria in mixed-mode fracture. This benchmark has a single edge notched located on the bottom of the beam, and the distance from the midspan is determined by the offset ratio $\bar{\lambda}$, which is defined by the distance of the notch from midspan over half of the span length. As depicted in Figure 3.12, the beam measures $230 \times 75 \times 25.4$ mm^3 and a 19×5×25.4 mm^3 notch is located at bottom of the beam. The following material properties are used: Young's modulus E =31.37 GPa, Poisson ratio $\nu = 0.2$, tensile strength f_t =4.4 MPa, and fracture energy G_F= 0.17 N/mm (Belytschko et al., 2000).

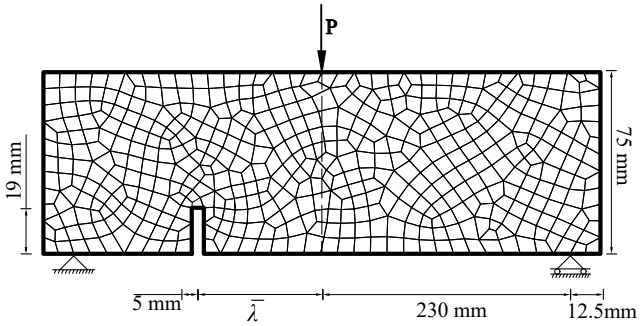

Figure 3.12: Mixed-mode three point bending beam test: geometry and mesh.

The cases of $\bar{\lambda} \leq 0.5$ are investigated here since these lead to failure with a single dominant crack (John and Shah, 1990). $\beta = 1$ is adopted for both of models studied here, which controls the shear strength and stiffness in mode-II for the traction-separation law as described in section 2.2.

The first simulated example is related to the specimen with $\bar{\lambda} = 0.5$. As depicted in Figure 3.13, Alfaiate's and Carol's failure surfaces predict the crack path appropriately and have a good

agreement with experimental results. Conversely, the Rankine criterion provides a crack path that deviates from the experimental result.

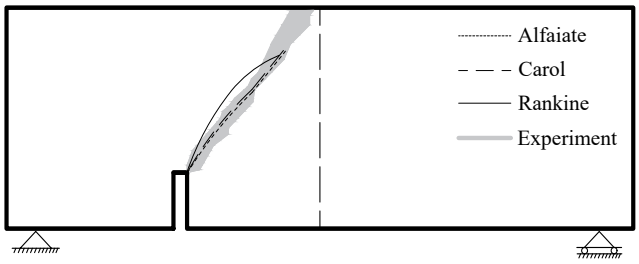

Figure 3.13: the comparison between the crack paths predicted by different cracking surface with experimental results for $\bar{\lambda} = 0.5$.

Note that load-displacement curves were not provided on the experimental study (John and Shah, 1990). In addition, the material parameters used in the simulations are taken by the values proposed in (Belytschko et al., 2000) for the same test. These can be a source of difference between the peak load obtained experimentally and numerically. As represented in Figure 3.14, the peak load is estimated as 2,100 kN for $\bar{\lambda}$=0.5 experimentally, whereas XFEM provides higher values near the peak load for studied criteria.

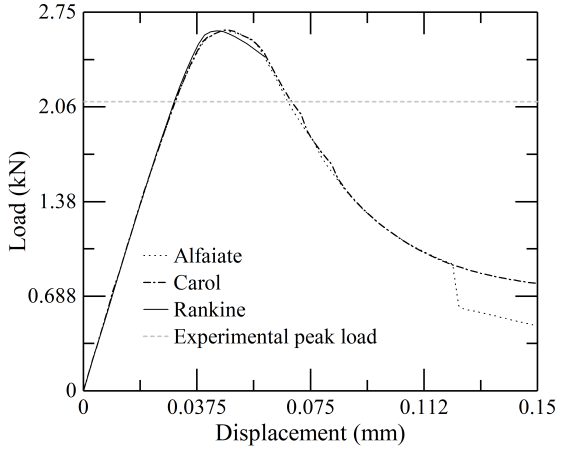

Figure 3.14: Load versus vertical displacement at the loaded node for mixed-mode three point bending beam with $\bar{\lambda} = 0.5$.

It is worth mentioning that, in previous studies (Belytschko et al., 2000; John and Shah, 1990; Mariani and Perego, 2003), the crack path has not been traced in the last steps of softening when the crack approaches the upper surface of the beam. This is related to the limitations of the criteria utilised in those studies that were not capable of capturing crack propagation in compression states, which is why the last stage of softening was never analysed. Note that, this is another difficulty that resulted from using the inappropriate failure surface (e.g. Rankine). The failure surfaces with emphasis on tensile stress as the only indicator of cracking (e.g. Rankine) cannot allow the crack occurring in structures facing the tensile and compressive state during the failure to grow to the last stages of the softening. Otherwise, the crack grows symmetrically (e.g. three point bending beam). Accordingly, a crack only propagates appropriately until the cracking area is on the tensile state. As a consequence, the criterion conventionally adopted cannot predict the crack path immediately after entering compression state, and practically the analysis fails without giving information on the last stage of the softening. Therefore, another problem is tackled in the current study is using the modified cracking surfaces (e.g. Alfaiate's and Carol's) to cover this kind of commonly-occurred case in engineering.

In Figure 3.15, the stress field along the horizontal axis is presented for different failure surfaces for vertical displacement of loaded node in u_y=0.06. As the stress field and crack path of Alfaiate's and Carol's criteria are identical, the results of Carol criterion have been omitted.

For $\bar{\lambda} = 0.25$, another model of mixed-mode three point bending beam is simulated to investigate the crack pattern and nodal values obtained by different failure surfaces. The

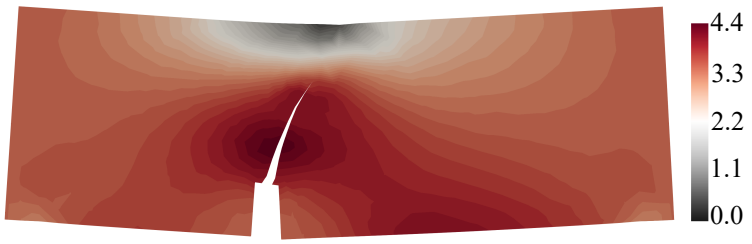

(a)

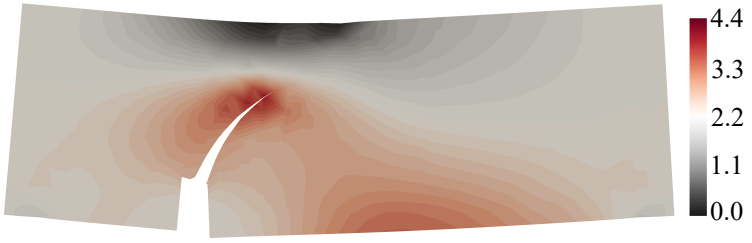

(b)

Figure 3.15: Mixed-mode three point bending test $\bar{\lambda} = 0.5$: Stress field σ_{xx} in MPa and crack path during softening when u_y=0.06 mm: (a) Alfaiate cracking surface (b) Rankine (displacements magnified 100 times).

material properties and boundary condition are the same as the previous model with $\bar{\lambda} = 0.5$, as depicted in Figure 3.12.

In Figure 3.16, the comparison between crack propagation indicated by the failure surfaces are presented. As observed, the Rankine criterion can predict the crack direction realistically for the three point bending beam with $\bar{\lambda} = 0.25$ compared to $\bar{\lambda} = 0.5$. According to experimental results, the peak load, in this case, is about $1,750$ kN. In Figure 3.17, the load-displacement curve shows that Alfaiate's and Carol's failure surfaces can predict more reliable peak load compared to the Rankine overestimating peak load in this analysis.

In Figure 3.18 the stress field along the horizontal axis in vertical displacement u_y = 0.06 for loaded node is presented.

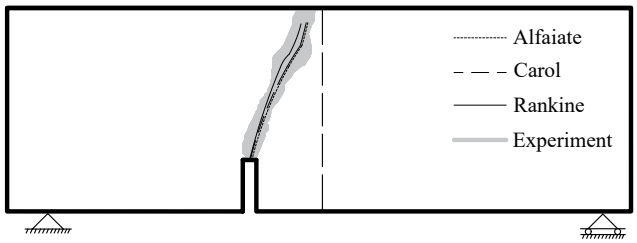

Figure 3.16: The comparison between the crack paths predicted by different cracking surface with experimental results for $\bar{\lambda} = 0.25$).

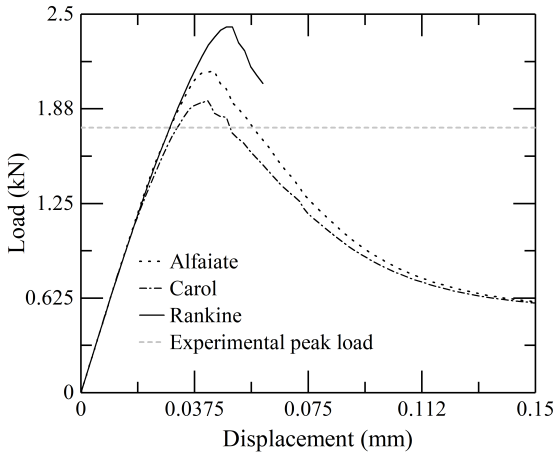

Figure 3.17: Load versus vertical displacement at the loaded node for mixed-mode three point bending beam with $\bar{\lambda} = 0.25$).

3.5.4 Uniaxial compression test

The uniaxial compression test studied by Van Geel (1998) is investigated to show the ability of modified failure surfaces to handle fracture in compression state. The cross-section of the rectangular prism is 97×97 mm^2 and the height equals 200 mm, as represented in Figure 3.19.

The material parameters are used: Young's modulus E =30 GPa, Poisson ratio $\nu = 0.18$, tensile strength f_t=2.96 MPa, compressive strength f_c=55.0 MPa (Van Geel, 1998). To estimate the compressive fracture energy G_{F_c}, empirical model proposed by Lertsrisakulrat et al. (2001) is

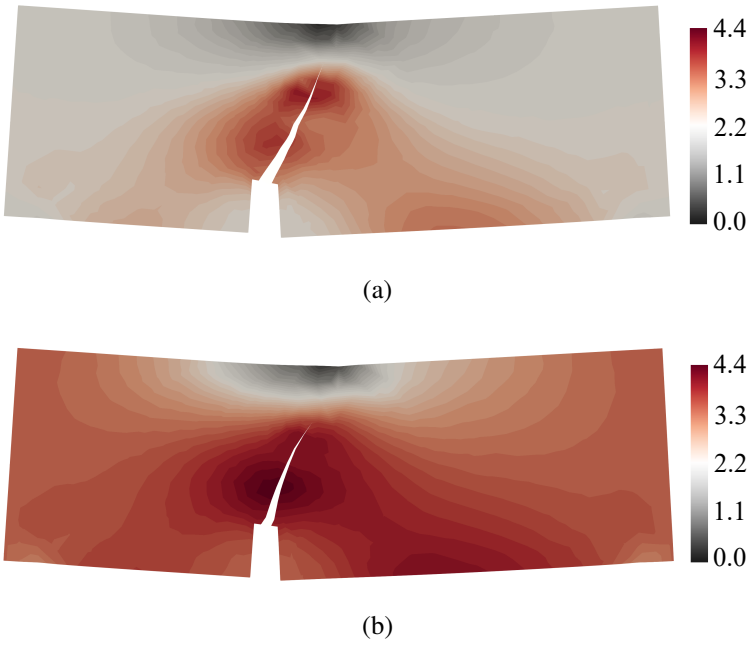

Figure 3.18: Mixed-mode three point bending test $\bar{\lambda} = 0.25$: Stress field σ_{xx} in MPa and crack path during softening when u_y=0.06 mm: (a) Alfaiate cracking surface (b) Rankine (displacements magnified 100 times).

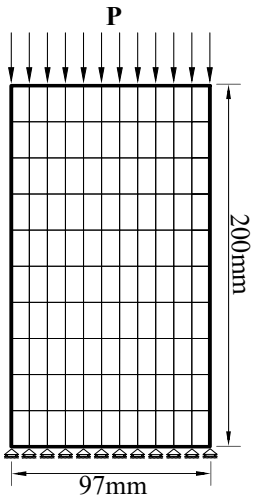

Figure 3.19: Uniaxial compression test: geometry and mesh.

utilised in this study as below:

$$G_{F_c} = 8.6 f_c^{\frac{1}{4}} \tag{3.9}$$

where the compressive fracture energy G_{F_c} has a relation with forth root of compressive strength f_c. According to Equation (3.9), $G_{F_c} \approx 23.4$ N/mm. For the discontinuity, the traction-separation relation proposed by Mariani and Perego (2003) and described in section 2.2 is used, where $\beta = 1$.

As shown in Figure 3.19, a uniformly distributed compressive load is applied in this study instead of loading platen with Teflon layer to remove the friction between loading platen and specimen on experimental research. The adopted mesh consists of 121 bilinear finite elements. Note that, to guarantee the symmetry of the problem, the two different cracks should grow from two upper and bottom surfaces of the prism and meet together at the middle surface of the specimen.

The crack pattern obtained by Alfaiate's and Carol's failure surfaces are represented and compared to experimental results in Figure 3.20. The results show a good agreement with experimental observation and the robustness of modified surfaces as a reliable full range of stress criteria to trace the crack path in contrast with Rankine pocket. Although the crack propagation results obtained from Alfaiate's and Carol's envelops are similar geometrically, there is a significant difference between peak load calculated by Alfaiate's and Carol's failure surfaces, as presented in Table 3.1. Note that, the traction-separation relationship used in the current study (see – section 2.2) has been developed for tensile state, and it cannot handle the compressive state properly. However, the peak load calculated indicates the accuracy of the simulation in terms of crack propagation.

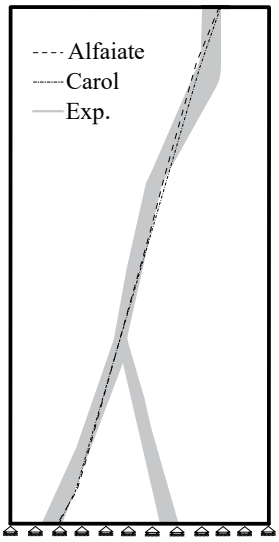

Figure 3.20: Uniaxial compression test: crack path at the end of softening stage for Alfaiate's and Carol's cracking surfaces.

Table 3.1: Uniaxial compression test: comparison of peak axial stress-displacement.

Criterion	Axial stress (MPa)	Displacement (mm)
Alfaiate	42	0.31
Carol	22	0.18
Experiment	45	0.32

In Figure 3.21, the snap shots of the stress field (σ_{xx}) along the horizontal axis in u_y=0.25 and 0.35 mm for Alfaiate's failure surface are represented.

This example shows that both components of the cracking process (initiation and propagation) dominate the analysis of concrete fracture. That is why the appropriate criterion picked for the cracking process can make a considerable change of results in fracture mechanics of quasi-brittle materials.

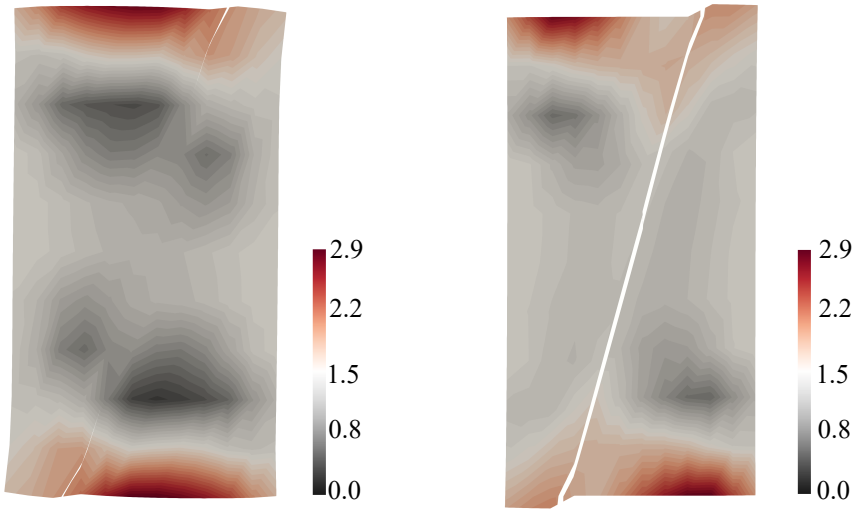

(a) (b)

Figure 3.21: Uniaxial compression test: stress field along horizontal axis for Alfaiate's surface in (a) u_y=0.25 mm (b) u_y=0.35 mm (displacements amplified 20 times).

3.6 Conclusions

In this chapter, the criteria tracing the crack path, including the approaches considering failure surfaces and averaged effective stress field to determine the crack initiation and propagation process are investigated. It is shown that all criteria used in literature and proposed here have advantages and disadvantages, such that their applicability depends on the problem at hand.

In contrast to the conventional approach, the modified failure surfaces proposed here can tackle mixed-mode failure problems during the softening as represented in section 3.5.3.

Two different failure surfaces for mixed-mode loading condition are proposed in this study. The proposed failure envelops represent the compatibility with the different loading conditions, compared to traditional fracture mechanics using Rankine cracking pocket conceptually covering mode-I fracture only.

The modified cracking surfaces reduce the computational effort to categorise the cracking states (shear, tensile or compressive) as done by the Mohr-Coulomb-based crack tracking algorithms responding to each state separately. This capability decreases the computational cost needed to check the cracking condition experienced by each element of a structure, which is a requirement for Mohr-Coulomb-based crack tracking approaches.

The comparison provided with the experimental results shows that the modified failure pockets can be employed as a full range criterion for predicting crack initiation and crack propagation in all loading conditions, including compression. Since the traction-separation laws introduced in conventional fracture mechanics are appropriate for tensile and shear states only, this shortage needs to be investigated further in future studies. Also, the results obtained reveal that the average effective stress should be utilised more carefully because of the severe sensitivity to the suggested length parameter.

As a final remark, the full range criterion studied here is a precious tool for all discrete strong discontinuity approaches, including Strong Discontinuity Approach (SDA), Discrete Strong Discontinuity Approach (DSDA), Generalised Strong Discontinuity Approach (GSDA), Linear Elastic Finite Element (LEFM) and X/GFEM, which need an initiation criterion transmitting the strain localisation information to the bulk. This study further reveals that the modified surfaces can be utilised as the credible alternative to the Rankine failure pocket used to initiate and propagate the crack for many years in discrete crack approaches. In addition, Alfaiate's failure surface can be useful to cover all range of loading conditions and even if high compression states.

CHAPTER 4

An XFEM multi-layered Heaviside enrichment for fracture propagation

---

Numerical modelling of material failure is relevant to numerous fields in science and engineering. The development of advanced numerical techniques such as eXtended Finite Elements Method has provided means of accurate prediction of failure in brittle, as well as in ductile materials. However, the present theories mostly rely on a global formulation, where the system of equations is subject to progressive increase of its dimension for crack propagation. An independent multi-layered enrichment is proposed in this chapter for an XFEM family of methods where groups of few elements in close proximity are assigned to an enrichment layer independent of the remaining ones. The enhanced degrees of freedom can be condensed out at the layer level, which in turn leads to system dimensions, sparsity, and bandness identical to those of the underlying finite elements. Nodal and elemental enrichment methods are shown to be particular limit cases of present approach.

The definition of the enrichment layers, the boundary value problem, and finite element discretisation are addressed in section 4.1. Implementation aspects in regards to multi-layered enrichment method is detailed in section 4.2. The degrees of freedom condensation process is given in section 4.3, and a cost-effective static condensation procedure, as an alternative, is suggested in section 4.4. The performance of the proposed technique is first studied using

element level examples for different crack geometries in terms of crack opening modes and condition number in Sec. 4.5. Then, using several structural examples, accuracy of the method is studied considering crack patterns, traction continuity and force-displacement responses. Finally, Sec. 4.6 summarises the main conclusions.

4.1 Theoretical formulation and finite element discretisation

The inevitable increasing computational cost of XFEM/GFEM stems from the use of a single enrichment layer and thus can be easily circumvented using multiple enrichment layers which can progressively be condensed out in the analysis. Each of these enrichment layers can be realised as the set of degrees of freedom responsible to enrich a certain neighbourhood of cracked elements as depicted in Figure 4.1 for a typical crack propagating path. These layers merely represent the enrichment neighbourhood; their height does not bear any physical/numerical meaning. The union of the subsets of enhanced degrees of freedom (corresponding to enrichment layers) must cover the entirety of cracked elements. Their intersection on the other hand, is null outside each layer; that is, the degrees of freedom from any two layers are independent of each other. The Schur complement system of such a multi-layered enrichment technique naturally overcomes dealing with any progressively enlarging system, which will be discussed further in the following.

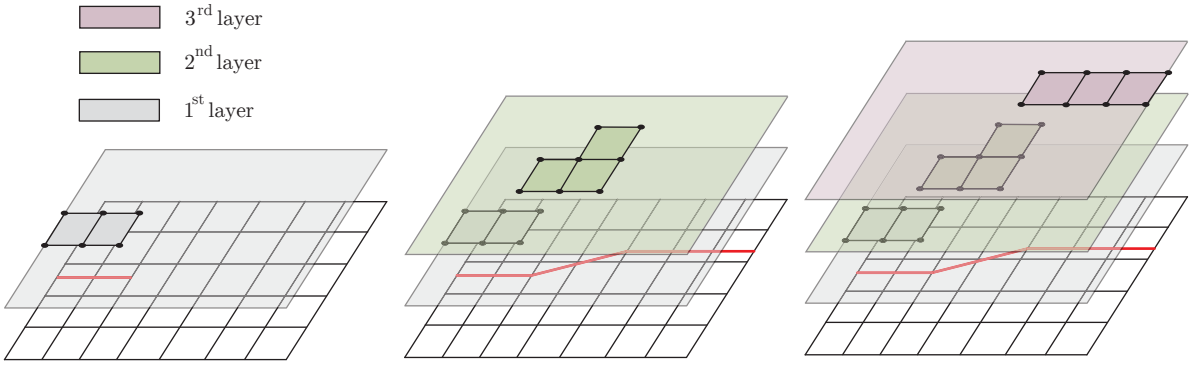

Figure 4.1: Enrichment layers with crack propagation.

The continuous and discontinuous displacement fields are discretised using the multi-layered concept as follows:

$$\hat{\mathbf{u}} = \sum_{I \in N_{tot}} \mathbf{N}_I(\mathbf{x}) \hat{\mathbf{a}}_I, \tag{4.1}$$

$$\tilde{\mathbf{u}} = \sum_{L \in N_S} \sum_{J \in N_L} \mathbf{N}_J(\mathbf{x}) \boldsymbol{\Psi}_J(\mathbf{x}) \tilde{\mathbf{a}}_{J,L} \tag{4.2}$$

In Equation (4.1), $\mathbf{N}(\mathbf{x})_I$, $\hat{\mathbf{a}}_I$, and N_{tot} represent respectively the usual element shape functions, nodal displacements associated with the continuous displacement field, and total set of nodes. The alternative definition of the discontinuous displacement field is found in Equation (4.2) with $\boldsymbol{\Psi}_J(\mathbf{x})$ representing the shifted Heaviside function (Zi and Belytschko, 2003), while $\tilde{\mathbf{a}}_{J,L}$ shows the enhanced nodal displacements of the J^{th} node enriched within the L^{th} enrichment layer. N_S and N_L on the other hand, are the total number of enrichment layers and the total number of nodes enriched in each layer L. For the sake of clarity, the full crack configuration of Figure 4.1 is repeated in Figure 4.2 to illustrate the above definitions.

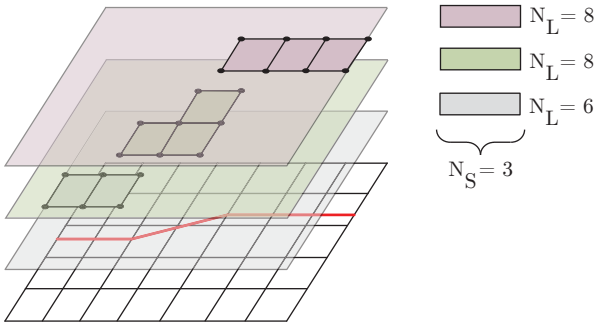

Figure 4.2: Multi-layer enrichment definitions; • represents the enrichment nodes at different layers.

It is important to note that, without further considerations, the total number of enriched degrees of freedom at this stage would be higher compared with the standard XFEM. This is so because the additional enhanced degrees of freedom found at the common edges of adjacent elements are independently included in more than one enrichment layer. Nevertheless, such an enrichment strategy can allow the complete condensation of the enhanced degrees of freedom and thus keep the global system dimensions the same as the uncracked mesh. Condensation process is realised independently of the size of each enrichment layer, which can be arbitrarily chosen between two limit cases. In the first case, a coarse scale problem can potentially represent the entire domain, in which case the standard XFEM/GFEM family of methods (Belytschko and Black, 1999; Duarte et al., 2000; Moës et al., 1999) are recovered. In the second case, an extremely fine scale would consider each element as an independent layer, which would lead to a standard type of embedded discontinuity approach. Accordingly, the static equilibrium can be expressed in terms of the regular and enriched nodal displacements. The finite element discretisation of Equation (2.56a) and Equation (2.56b) by means of the field approximations given in Equation (4.1) and Equation (4.2) leads to the similar stiffness and force terms in Equations (2.63a)-(2.68b) as described in section 2.3.3. Consequently, the

static equilibrium for a cracked element can be finally expressed as follows:

$$\begin{bmatrix} \mathbf{K}_{\hat{a}\hat{a}} & \mathbf{K}_{\hat{a}\tilde{a}} \\ \mathbf{K}_{\tilde{a}\hat{a}}^{T} & \mathbf{K}_{\tilde{a}\tilde{a}} + \mathbf{K}_{d} \end{bmatrix} \begin{Bmatrix} \hat{\mathbf{a}} \\ \tilde{\mathbf{a}} \end{Bmatrix} = \begin{Bmatrix} \hat{\mathbf{f}} \\ \tilde{\mathbf{f}} \end{Bmatrix}. \tag{4.3}$$

Note that in the integrals involving the Heaviside function, the domain is split into subdomains Ω^{-} and Ω^{+}, and the integrals are carried out on each triangular element defined by the centroid of each subdomain and the vertices (Dias-da-Costa et al., 2010; Moës et al., 1999; Park et al., 2009). Furthermore, the integral carried over Γ_d is calculated based on the Newton–Cotes scheme using two integration points for each element to alleviate the spurious oscillations that have been reported in the literature (Coutinho et al., 2003; Dias-da-Costa et al., 2010; Simone, 2004) and in chapter 5 is detailed.

4.2 Layer activation and enrichment procedure

A Rankine criterion is used to identify the onset of crack localisation based on a weighed stress state which is monitored at the centroid of non-cracked elements and at the tips of existing cracks. In the calculation of the weighed stress state, a Gaussian weight function is employed to smooth the stress field (Dias-da-Costa et al., 2009; Wells and Sluys, 2001a). A new discontinuity is introduced through the element whenever the averaged maximum stress at the crack tip reaches the tensile strength of the material, and the propagation angle is taken orthogonal to the first principal stress. The process of crack propagation is handled using a simplified version , which assures the continuity of the crack path and involves the following

steps depending on the number of pre-existing crack tips at the edges of the element about to crack: if there are no tips, a new crack segment is embedded through the centroid of the element (crack front initiation); otherwise, the crack is constrained to propagate through the tip (crack propagation).

When the crack initiation criterion is met at any given element, the possibility of assigning it to the existing enrichment layers must be explored first. An active length scale parameter l_a is used to progressively define concentric circles of diameter $\eta_L = Ll_a$ at the centroid of the first cracked element, where L is a natural number smaller than (or equal to) N_S, the number of current enrichment layers (see – Figure 4.3.a). Each time the crack propagates to a new element, this element is automatically assigned to the last enriched layer if its centroid lays inside the circle η_L. Otherwise, a new layer of enrichment must be initialised and the element is then assigned to it. This approach is very effective during crack propagation, as any element can be quickly associated to a layer by simply searching for the concentric circle with the minimum diameter that contains its centroid.

Algorithm 4.1 Enrichment procedure during crack propagation

```
1:  procedure ENRICHMENT(el, N_S, l_a)
2:      d ← element el distance from first cracked element
3:      L ← N_S
4:      η_L ← Ll
5:      if d > η_L then
6:          N_S ← N_S + 1 (initialising a new layer)
7:          L ← N_S
8:      end if
9:      return L
10: end procedure
```

The initial active length, l_a, is here defined as λh, where λ is a natural number (including zero) and h is the characteristic element size, which is the diameter of the smallest circumference that

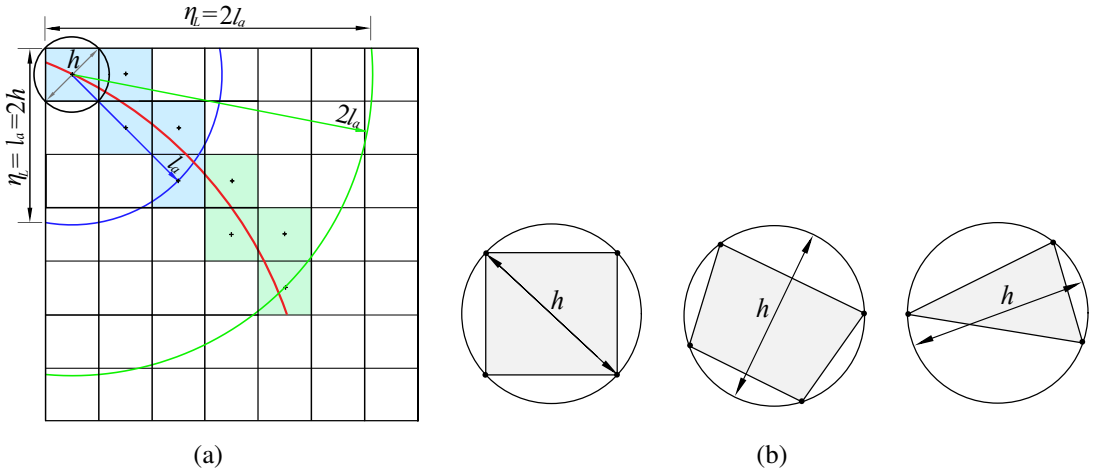

Figure 4.3: Multi-layer enrichment details: a) active length ($l_a = 2h$); and b) characteristic element size (h).

fully inscribes a finite element of typical size (see – Figure 4.3.b). Note that, an active length of $\lambda = 1$ implies that each enrichment layer will contain mostly a pair of adjacent cracked elements for a regular mesh (see – Figure 4.3.a). A completely independent enrichment of each cracked element would be achieved by taking $\lambda = 0$, whereas $\lambda = \infty$ would lead to a single layer encompassing all enriched elements, therefore matching with the standard XFEM approach. The procedure discussed above is summarised in Algorithm 4.1. d in line 2 of the algorithm, denotes the distance between the centroids of the first element and the one being currently enriched (i.e. cracked).

4.3 Local Schur complement

The condensation of the enhanced degrees of freedom is the last step in the development and implementation of the multi-layered enrichment strategy. Given that the layers are independently enriched, they can also be independently condensed out of the system of

equations. In fact, each layer of enrichment can be seen as a local Schur complement (Kraus, 2006) of a multiple system composed of all enriched layers. By manipulating the system of equations, the Schur complement or condensed stiffness matrix of each layer, $\mathbf{K}_{cond}^{els_L}$, and force counterpart, $\mathbf{f}_{cond}^{els_L}$, can be written as follows:

$$\mathbf{K}_{cond}^{els_L} = [\mathbf{K}_{\hat{a}\hat{a}} - \mathbf{K}_{\hat{a}\tilde{a}}(\mathbf{K}_{\tilde{a}\tilde{a}} + \mathbf{K}_d)^{-1}\mathbf{K}_{\tilde{a}\hat{a}}^T]^{els_L}, \tag{4.4}$$

$$\mathbf{f}_{cond}^{els_L} = [\hat{\mathbf{f}} - \mathbf{K}_{\hat{a}\tilde{a}}(\mathbf{K}_{\tilde{a}\tilde{a}} + \mathbf{K}_d)^{-1}\tilde{\mathbf{f}}]^{els_L}. \tag{4.5}$$

where all the entities are assembled stiffness and force terms of the cracked elements belonging to the layer L. This is denoted by the superscript els_L, while subscript *cond* stands for static condensation. Naturally, the Schur complement, $\mathbf{K}_{cond}^{els_L}$, has the same dimension as the uncracked system of elements, $\mathbf{K}_{\hat{a}\hat{a}}{}^{els_L}$. An alternative option that can be implemented for tackling the condensation process is presented in section 4.4.

The condensed stiffness of each layer is handled as a generalised element in the assembly of the global system. The standard finite element procedure is followed for this purpose in the first step of analysis. If there are already any enrichment layers, the condensed stiffness of each layer is used in the assembly. After that, in each step or iteration, whenever an event occurs that requires the update of an existing layer of enrichment, e.g. the stiffness of a cracked element changes and/or the crack propagates to another element within the same layer, the global stiffness matrix will also need to be updated. This, however, is done by directly updating the stiffness associated with the layer (or layers) where the change is detected. This requires disassembling the current stiffness matrix of the layer from the global system, which

includes all previously enriched elements and the newly cracked element (if it exists). Note that if this is the first cracked element to be added in the layer, only the original stiffness matrix of the element is disassembled. The local Schur complement is then calculated as represented in Equation (4.4) and added to the global stiffness matrix of the structure in the step of analysis. It is important to highlight that because of the shifted Heaviside function there is no need to consider blending elements (Zi and Belytschko, 2003).

The complete procedure described above is summarised in Algorithm 4.2, where Line 11 represents the stiffness matrix of a local Schur complement system. It should also be mentioned that, as will be discussed thoroughly in section 4.5.1, each enrichment layer typically only contains a few enriched elements, which means that the condensation processes does not involve more than a handful of elements given independence of enrichment layers.

Algorithm 4.2 Updating stiffness matrix in crack propagation problems.

1: **procedure** UPDATE($\mathbf{K}$, $\mathbf{U}$)
2: **for** each element el **do**
3: **if** crack is required (initiation criterion 4.2) **then**
4: disassemble $\mathbf{K}^{el}$ from $\mathbf{K}_{global}$
5: $L \leftarrow$ Algorithm 4.1
6: $els_L \leftarrow$ elements already enriched by L
7: **if** $els_L \neq \emptyset$ **then**
8: disassemble $\mathbf{K}^{els_L}$ from $\mathbf{K}_{global}$
9: **end if**
10: $els_L \leftarrow els_L \cup el$
11: $\mathbf{K}_{cond}^{els_L} \leftarrow [\mathbf{K}_{\hat{a}\hat{a}} - \mathbf{K}_{\hat{a}\tilde{a}}(\mathbf{K}_{\tilde{a}\tilde{a}} + \mathbf{K}_d)^{-1}\mathbf{K}_{\tilde{a}\hat{a}}^T]^{els_L}$
12: assemble $\mathbf{K}_{cond}^{els_L}$ in $\mathbf{K}_{global}$
13: **end if**
14: **end for**
15: **end procedure**

4.4 Alternative Static condensation

The concept of multi-layer enrichment and condensing each layer out leads to a global system of equations of the same size regardless of the enrichment. In addition, the sparsity as well as bandness of the stiffness matrix are also kept unchanged. It should be noted that $[\mathbf{K}_{bb}+\mathbf{K}_d]^{els_L}$ in Equation (4.4) typically varies in each step due to the non-linear material behaviour. In many applications of fracture mechanics, however, the bulk is assumed linear elastic, whereas the non-linear behaviour is lumped at the discontinuity. Even in cases where the bulk is non-linear, during the softening of the discontinuity it still unloads elastically in the neighborhood of the crack because of equilibrium conditions. In practical terms, $\mathbf{K}_{bb}^{els_L}$ can be frequently constant during analyses, while $\mathbf{K}_d^{els_L}$ may vary depending on the non-linear response of the discontinuity. Within a layer, the discontinuity stiffness term in Equation (4.4) results from the assembly of the contribution of each individual cracked elements calculated by Equation (2.67) as follows:

$$\mathbf{K}_d^{els_L} = \overset{els_L}{\mathbf{A}}\Big[4\int_{\Gamma_d}\mathbf{N}^T\mathbf{R}^T\mathbf{T}\,\mathbf{R}\,\mathbf{N}\,d\Gamma\Big], \tag{4.6}$$

where $\mathbf{A}$ represents the standard assembly operator. The integration is done based on the 2-point Newton–Cotes scheme within each element. Regardless of the selected integration scheme, the resulting expression can be generically cast for two integration points as follows:

$$\mathbf{K}_d^{els_L} = \overset{els_L}{\mathbf{A}}\Big[\overline{\mathbf{N}}_i^T\overline{\mathbf{T}}_i\,\overline{\mathbf{N}}_i+\overline{\mathbf{N}}_j^T\overline{\mathbf{T}}_j\,\overline{\mathbf{N}}_j\Big], \tag{4.7}$$

where

$$\overline{\mathbf{N}} = \mathbf{R}\,\mathbf{N} \tag{4.8}$$

$$\overline{\mathbf{T}} = 4w\mathbf{T}, \tag{4.9}$$

and subscripts i and j represent each integration point over the interface, while w stands for the corresponding integration weight. In general, $\overline{\mathbf{N}}$ will have the same dimensions of the regular shape functions: 2 by the number of regular degrees of freedom of a cracked element for bidimensional problems, whereas $\overline{\mathbf{T}}$ is 2 by 2. Equation (4.7) can be alternatively arranged as follows:

$$\mathbf{K}_d^{els_L} = \overline{\mathbb{N}}_{pq}^T \overline{\mathbb{T}}_{qq}\, \overline{\mathbb{N}}_{qp}, \tag{4.10}$$

where $\overline{\mathbb{N}}$ and $\overline{\mathbb{T}}$ are obtained by stacking in $\overline{\mathbf{N}}$ and $\overline{\mathbf{T}}$, respectively, for the elements els_L enriched by layer L. In addition, assembly operation is implied in $\overline{\mathbb{N}}$ and $\overline{\mathbb{T}}$ where $p = 2N_L$, the number of enriched degrees of freedom in layer els_L while q is the rank of matrix $\mathbf{K}_d^{els_L}$.

Considering that the matrix $\overline{\mathbb{T}}$ is a block diagonal matrix composed of constitutive matrices of individual elements, $\overline{\mathbf{T}}^e$ for $e \in els_L$, possibility of an alternative procedure for static condensation can be explored. In the following, the Sherman-Morrison-Woodburry identity (Gentle, 2007) for the inverse of the sum of two matrices is applied. Considering that $\mathbf{K}_{bb}$ and $\mathbf{K}_{bb} + \mathbf{K}_d$ are both invertible and by dropping the superscript els_L for convenience, then:

$$(\mathbf{K}_{\tilde{a}\tilde{a}} + \mathbf{K}_d)^{-1} = \mathbf{K}_{\tilde{a}\tilde{a}}^{-1} - \mathbf{K}_{\tilde{a}\tilde{a}}^{-1}\overline{\mathbb{N}}^T(\overline{\mathbb{T}}^{-1} + \overline{\mathbb{N}}\mathbf{K}_{\tilde{a}\tilde{a}}^{-1}\overline{\mathbb{N}}^T)^{-1}\overline{\mathbb{N}}\mathbf{K}_{\tilde{a}\tilde{a}}^{-1}. \tag{4.11}$$

By substituting Equation (4.11) in Equation (4.4), the following form can be obtained:

$$\mathbf{K}_{cond} = \mathbf{K}_{\hat{a}\hat{a}} - \mathbf{K}_{\hat{a}\tilde{a}}\left[\mathbf{K}_{\tilde{a}\tilde{a}}^{-1} - \mathbf{K}_{\tilde{a}\tilde{a}}^{-1}\overline{\mathbb{N}}^{T}(\overline{\mathbb{T}}^{-1} + \overline{\mathbb{N}}\mathbf{K}_{\tilde{a}\tilde{a}}^{-1}\overline{\mathbb{N}}^{T})^{-1}\overline{\mathbb{N}}\mathbf{K}_{\tilde{a}\tilde{a}}^{-1}\right]\mathbf{K}_{\hat{a}\tilde{a}}^{T}, \tag{4.12}$$

which can be recast as:

$$\mathbf{K}_{cond} = \underbrace{\mathbf{K}_{\hat{a}\hat{a}} - \mathbf{K}_{\hat{a}\tilde{a}}\mathbf{K}_{\tilde{a}\tilde{a}}^{-1}\mathbf{K}_{\tilde{a}\hat{a}}^{T}}_{\left[Const.\right]_{pp}} + \underbrace{\mathbf{K}_{\hat{a}\tilde{a}}\mathbf{K}_{\tilde{a}\tilde{a}}^{-1}\overline{\mathbb{N}}^{T}}_{\left[Const.\right]_{pq}} \left(\overline{\mathbb{T}}^{-1} + \underbrace{\overline{\mathbb{N}}\mathbf{K}_{\tilde{a}\tilde{a}}^{-1}\overline{\mathbb{N}}^{T}}_{\left[Const.\right]_{qq}} \right)^{-1} \underbrace{\overline{\mathbb{N}}\mathbf{K}_{\tilde{a}\tilde{a}}^{-1}\mathbf{K}_{\tilde{a}\hat{a}}^{T}}_{\left[Const.\right]_{qp}}. \tag{4.13}$$

Note that within the assumptions described in the beginning of this section, as the discontinuities represented within a layer progressively soften, only $\overline{\mathbb{T}}^{-1}$ remains non-constant during the analysis. All other matrices identified in Equation (4.13) are constant and only need to be evaluated once when a new discontinuity propagates within the layer. In addition, with softening, $(\overline{\mathbb{T}}^{-1} + \overline{\mathbb{N}}\mathbf{K}_{\tilde{a}\tilde{a}}^{-1}\overline{\mathbb{N}}^{T})^{-1}$ gradually reduces until completely vanishing, which in turn renders the condensed stiffness matrix that of the stress-free cracked elements.

4.5 Numerical examples

This section presents several element and structural examples used to assess the performance of the new multi-layered approach. For this purpose, the effect of the active length is first studied on the jump continuity across layers. The second example investigates the conditioning of the Schur complement system as a function of the crack location with respect to mesh nodes. Next, several structural examples having different geometries, discontinuity constitutive models, and loading conditions, are used to assess the performance at local and

global levels, and to establish a comparison with experimental and numerical data in the literature.

4.5.1 Discontinuities cutting a corner

When a discontinuity cuts a corner in a quadrilateral element, associated numerical issues can lead to either a truly rank deficient system (Linder and Armero, 2007a; Manzoli and Shing, 2006); or an ill-conditioned one with consequences in both static (Fries and Belytschko, 2010; Siavelis et al., 2013; Strouboulis et al., 2000) and dynamic problems (Belytschko et al., 2003; Remmers et al., 2008). While the latter imposes difficulties in obtaining accurate and efficient solutions, the former leads to internal mechanisms (instabilities) which if not addressed robustly, can completely hamper the solution procedure. In this regard, the performance of the proposed multi-layer strategy is first studied for the case of internal mechanisms using an element level example. The effect of the number of enrichment layers on the continuity of jumps is studied on a domain discretised using a regular mesh of 2 by 2 elements, each with an edge length of 2. The domain has a crack crossing three finite elements with the geometry depicted in Figure 4.4. Non-homogeneous Dirichlet boundary conditions are applied over the perimeter of the domain to reproduce an arbitrary opening with non-constant jumps along the cracks. The Young's modulus and Poisson ratio of the bulk are 1 and 0.2, respectively. The normal tangent stiffness is chosen as -1×10^{-5} and 0, respectively to capture the behaviour of an almost and a fully softened step of analysis. In both cases, the shear tangent stiffness is zero.

For each normal stiffness, three different enrichment strategies are compared. Firstly, three enrichment layers are used, one for each cracked element. In the second case, two layers are used, one containing two neighbour cracked elements, and the other containing the third cracked element. Finally, in the third case, a single layer contains all the cracked elements. All enriched layers are illustrated using colours in the first row of Figure 4.4. Naturally, the number of additional degrees of freedom required by each model prior to the static condensation are different, in this case, 24, 20, and 16. The results for an almost and fully softened discontinuity are shown in the second and third rows of Figure 4.4. From this figure it is clear that the non-conforming crack openings are enhanced considerably. However, when two elements are enriched in the same layer this problem is substantially reduced, and vanishes when all elements are in the same layer, as it would be expected.

The instability becomes severe in the case of the fully softened cracks in the models with three layers, which is in agreement with the instability reported for embedded approaches (Linder and Armero, 2007a; Manzoli and Shing, 2006). In this case, the stiffness matrix of the model is indeed rank deficient by one, which can be verified by an eigen-decomposition following the application of the Dirichlet boundary conditions. Therefore, there is an internal spurious deformation mode allowing the non-physical rotation of the triangular domain cut by the discontinuity and seen on the bottom left corner of Figure 4.4. More importantly, the rank deficiency is not present for any other model, regardless of the stiffness of the discontinuity. Therefore, as long as every enrichment layer contains more than a single element in the present problem, the deficiency is resolved. In general however, certain mesh/crack geometries might necessitate the use of slightly more than two elements in each

enrichment layer in order to resolve the aforementioned numerical issues. Stress locking was also noticed when using three enrichment layers which is associated with the substantial non-conforming crack openings. Considering the ability of XFEM in capturing the kinematics of both transnational and rotational rigid body movements along with the relative stretching of Ω^+ over Ω^- (Dias-da-Costa et al., 2010), stress locking was not observed for the models containing more than one element in a layer. In addition, unlike the embedded approaches, no additional constraints were needed on the enhanced field to overcome the singularity associated with rigid body rotation as suggested by (Linder and Armero, 2007a; Manzoli and Shing, 2006).

4.5.2 Circular inclusion

Following the discussion in section 4.5.1, the performance of the method is here investigated by targeting the ill-conditioning of the system, which can compromise the accuracy and efficiency of the solution procedure. For this purpose, the effect of the condensation on the condition number of the stiffness matrix is studied on an inclusion embedded in a domain (see – Figure 4.5.a). This problem was first solved analytically in (Keer et al., 1973), and using XFEM in (Belytschko et al., 2001). For the sake of clarity in the investigation of the effect of the enrichment and crack location relative to mesh nodes, a very coarse discretisation is employed (see – Figure 4.5.b). The domain size is 0.9 by 0.9 and has the same properties of the circular inclusion: Young's modulus and Poisson ratio of 1 and 0, respectively. A unitary uniform compressive stress in the vertical direction, and a unitary tensile stress in the horizontal direction are simultaneously applied to the matrix. The interface is cohesionless,

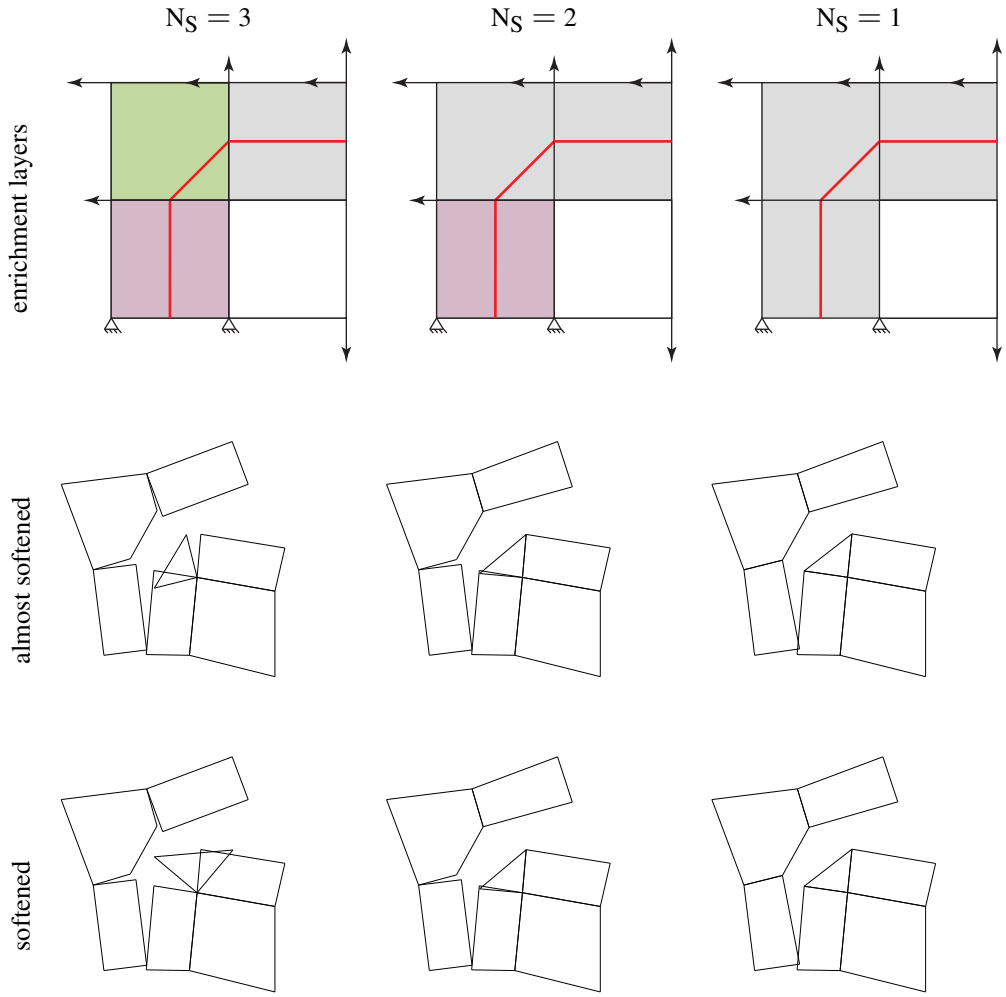

Figure 4.4: Instability of stiffness matrix in case of a crack separating a single node on one side. Almost softened and softened normal tangent stiffness represent respectively, $k_n = -1 \times 10^{-5}$ and $k_n = 0$. Arrows represent the prescribed Dirichlet boundary conditions.

which means that only compressive stresses can develop at the interface between the inclusion and matrix. Accordingly, a very small penalty value of 10^{-5} is chosen in the shear direction (k_s) just to prevent the rotational motion of the inclusion. In the normal direction and when in contact, the normal penalty is selected in the range of 1 to 10^{10}. When the interface is in tension, a zero normal tangent stiffness is assumed instead. Four different enrichment configurations employed in this example are illustrated in Figure 4.6.

The geometry of the interface is defined by the intersection of the edges of the elements with the inclusion perimeter. The inclusion size defined by its radius, R, is varied in each analysis from R_{min} – which creates small regions where discontinuities separate a single node – to R_{max} where discontinuities are tangent to the external boundaries of the elements.

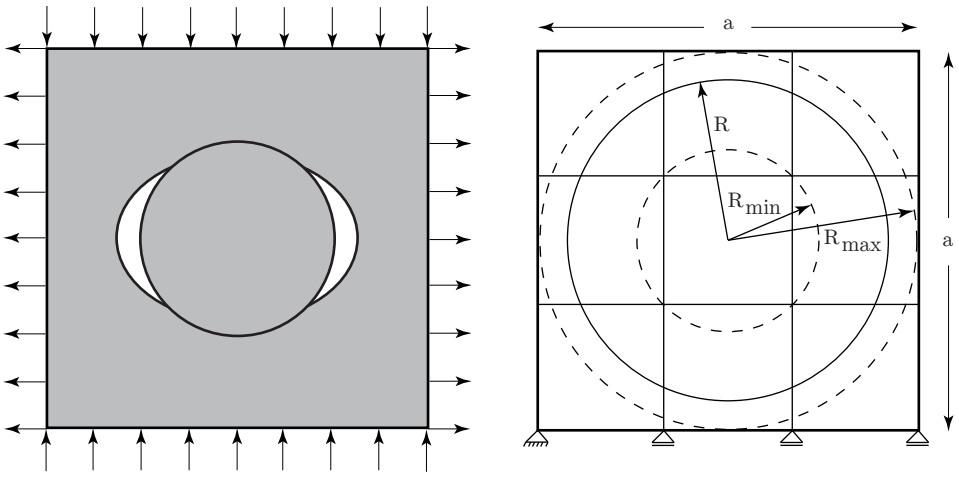

Figure 4.5: Inclusion problem definition: a) analytical model; b) finite element mesh with variable inclusion radius range.

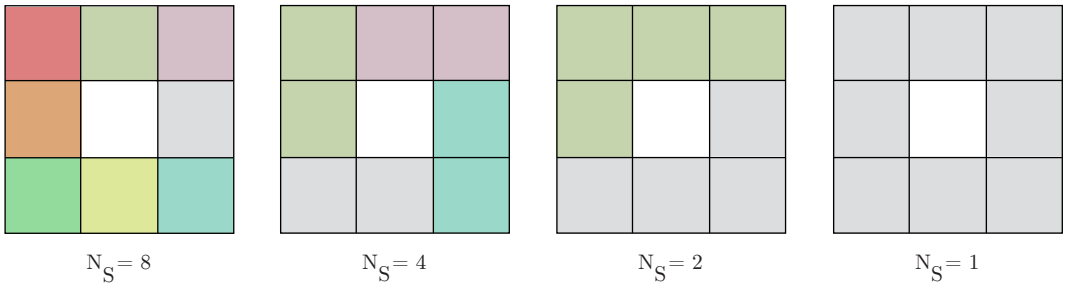

Figure 4.6: Inclusion problem enrichment layers.

Figure 4.7 shows the condition number as a function of the inclusion radius for different active lengths, as well as that obtained using standard XFEM. For the latter, the normal stiffness directly impacts the condition number as illustrated by the shaded area on the figure,

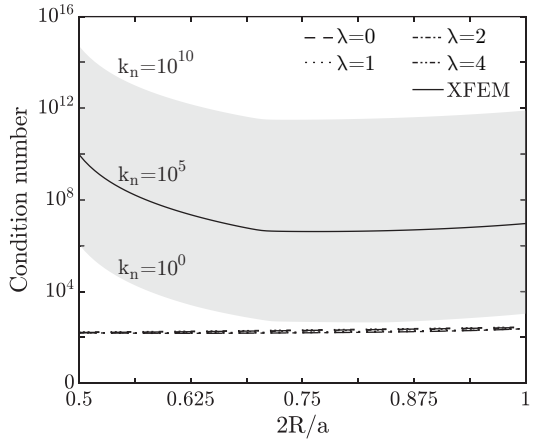

Figure 4.7: Condition number as a function of inclusion radius.

which is the envelope for all the range of tested values and varying radius. There is indeed considerable linear dependency between the regular and enrichment shape functions when the crack approaches a single node (Siavelis et al., 2013), i.e. when the radius is close to R_{min}. With an increasing radius, the condition number decreases, regardless of the penalty employed, until $R \approx (R_{min} + R_{max})/2$. After that, there is a slight increase when the interface approaches the parallel outer edges. Conversely, the multi-layer enrichment strategy, shows a drastic smaller condition number for all active lengths. In fact, this is of the same order of the underlying uncracked finite element mesh. In addition, the condition number remains nearly constant with respect to the interface stiffness, which is why only the curve for $k_n = 10^5$ is represented in the figure. This is a significant advantage of the multi-layered approach, which is associated with the static condensation of the enhanced degrees of freedom and allows maintaining the condition number similar to the non-cracked mesh.

4.5.3 Single-edge notched beam

A single-edge notched beam with anti-symmetric loading conditions (Schlangen, 1993) is simulated in this section. The reference beam is $400 \times 100 \times 100$ mm^3 with a $5 \times 20 \times 100$ mm^3 notch at the top, and is discretised by 474 bilinear finite elements – see representation in Figure 4.8. Concrete is treated as linear elastic, with a Young's modulus of $35,000$ N/mm^2 and a Poisson's ratio equal to 0.15. The tensile strength of the material is 3.0 N/mm^2 and fracture energy $G_F = 0.1$ N/mm (Schlangen, 1993). The initial normal and shear stiffnesses are $k_n = k_s = 10^5$ N/mm^5, and upon crack opening the uncoupled mode-I at the discontinuity with zero shear stiffness.The arc-length method is applied to monotonically increase the relative crack mouth sliding displacement (CMSD).

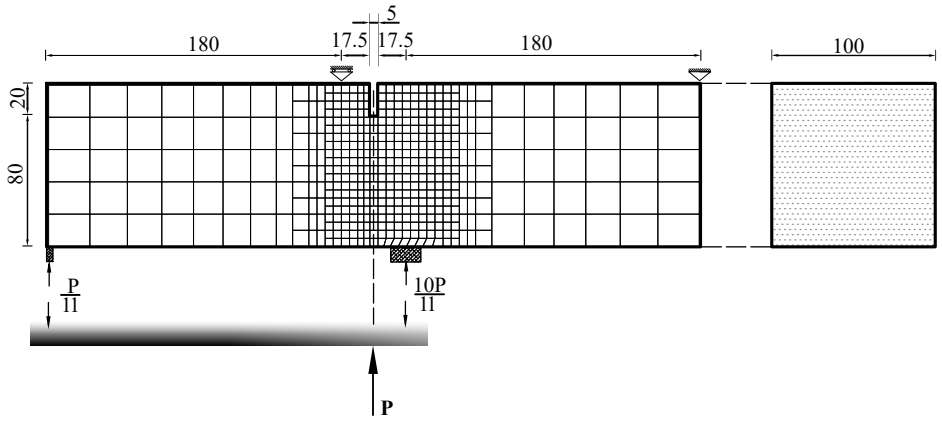

Figure 4.8: Geometry and mesh (dimensions in 'mm').

Figure 4.9 shows the enrichment layers for $\lambda = 1$, which on average implies two or three elements compose each enrichment layer for a regular mesh. The crack mouth sliding displacement (CMSD) *versus* load curves for different active lengths of $\lambda = 1$, 2 and 8 are represented in Figure 4.10, where it can be seen the good agreement among the lengths and also standard XFEM. The results of $\lambda = 0$ are also presented, which, as was already discussed

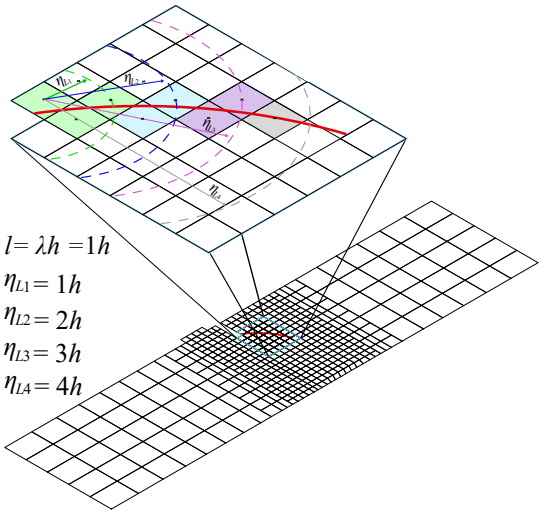

Figure 4.9: Representation of enrichment layers for $\lambda = 1$ at an advanced stage of crack propagation.

in a previous section, leads to internal mechanisms and difficulties in the numerical solution. This explains the different response after softening begins, which significantly deviates from the solution at the last stages of loading. The effect of the internal mechanism is represented in Figure 4.11 for a crack mouth opening displacement (CMOD) of 0.1 mm, which seems to support the conclusion that enough conformity is obtained for λ above 1. Interestingly, even though the curves are quite similar for an active length of 1 and 2, differences can still be found in the stress distribution particularly at the last stages of the analysis (see – Figure 4.12). The model with the smallest active length does not capture appropriately the stress localisation near the lower support, which may be caused by the combined effect of insufficient mesh size and not enough compatibility among the elements inside each layer. Regardless of this local effect, the crack patterns are nearly coincident.

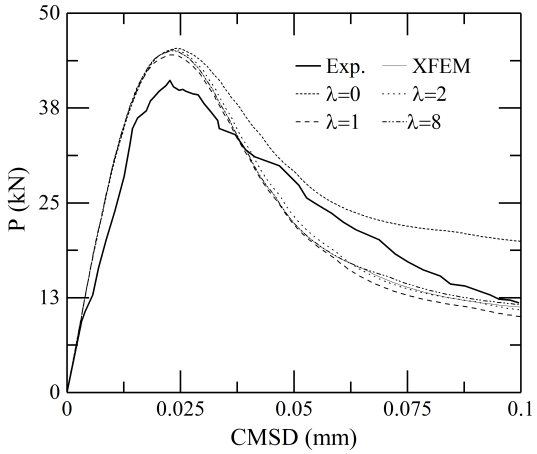

Figure 4.10: Load *versus* CMSD curves for different active lengths and experimental results.

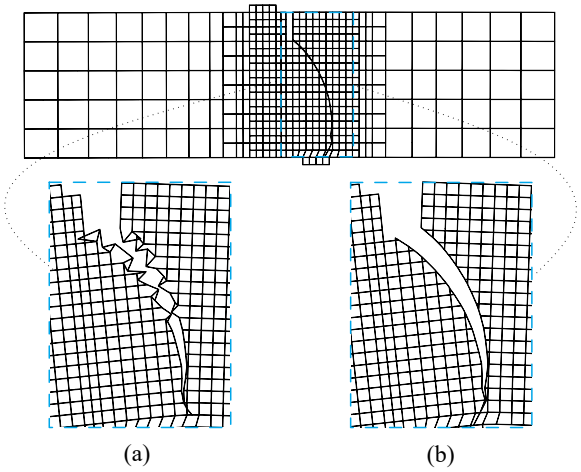

Figure 4.11: Single-edge notched beam: deformed mesh at CMOD=0.1mm (with displacements amplified 50 times): (a) $\lambda = 0$; (b) $\lambda = 1$.

4.5.4 Galvez notched beam

A single-notched beam was tested under bending by Gálvez et al. (1998) with different support conditions. The sample with K = 0 is adopted here to investigate further the effect of mixed mode fracture. The geometry of the structure is represented in Figure 4.13 together with the selected mesh of 1,217 bilinear elements. The concrete is simulated using a Young's modulus of $38,400$ N/mm^2 and a Poisson ratio of 0.2, whereas the tensile strength is $f_t = 3.0$ N/mm^2.

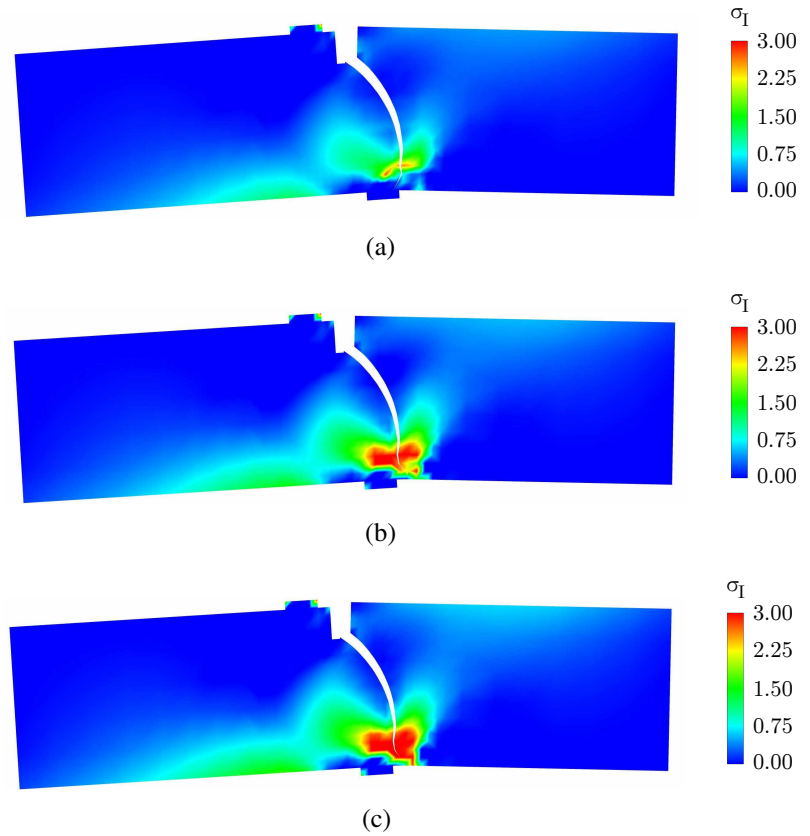

Figure 4.12: Single edge notched beam – maximum principal stress (N/mm^2) contour at u_v=0.3mm (with displacements amplified 100 times): (a) $\lambda = 1$; (b) $\lambda = 2$; (c) XFEM.

The uncoupled mode-I exponential softening law with fracture energy $G_F = 0.0688$ N/mm is taken for the discontinuity. The crack path is defined with an angle of 64° based on the experimental data and a relatively high penalty stiffness, $k_n = k_s = 10^8$ N/mm^3, is used to enforce it to remain closed at each integration point until reaching the tensile strength. The shear stiffness drops to zero with the opening of the crack, whereas the normal stiffness follows directly from the softening mode-I law. The arc-length method is used to solve the problem by monotonically increase the Crack Mouth Opening Displacement (CMOD).

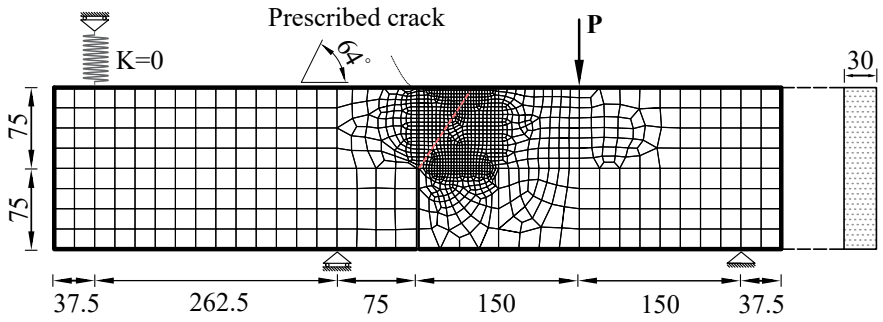

Figure 4.13: Geometry, loading and boundary conditions, and mesh (dimensions in 'mm').

Figure 4.14 shows the load *versus* CMOD curves for multi-layers of different sizes, all with a very good agreement with standard XFEM and experimental results. Results for different active lengths are almost coincident. This can also be seen in the stress fields shown in Figure 4.15, where an active length of $\lambda = 1$ already provides results in excellent agreement with those of XFEM.

To explore more in detail the effect of the non-conforming elements, it can be seen that there are minor localised differences in the traction profile in front of the notch (see – Figure 4.16). A minor oscillation is found about 95 mm above the notch for the discretisation with the smaller active radius. It should be mentioned that such an oscillation could be related to the high penalty adopted for the discontinuity and the small number of elements connected in the layer (see – section 4.5.1). Interestingly, although these differences are quite noticeable in the early stages of the analysis, i.e. CMOD$=0.05$ mm (see – Figure 4.16.a), they tend to vanish at the later stages, i.e. CMOD$=0.16$ mm (see –Figure 4.16.b), which is why the multi-layer enrichment provides good results almost independently of the selected size of the domain even though there can still sometimes occur just one element in a layer when $\lambda = 1$ is adopted.

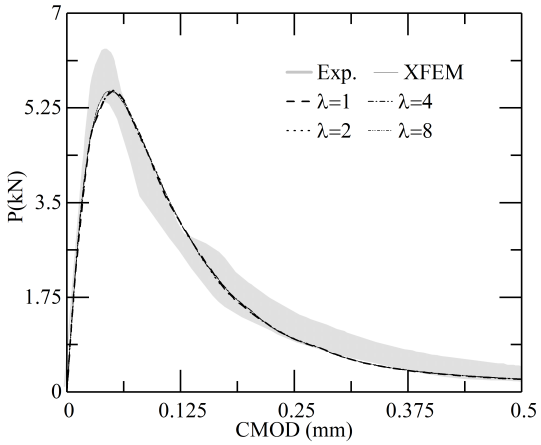

Figure 4.14: Load *versus* CMOD curves for the different active lengths and experimental results.

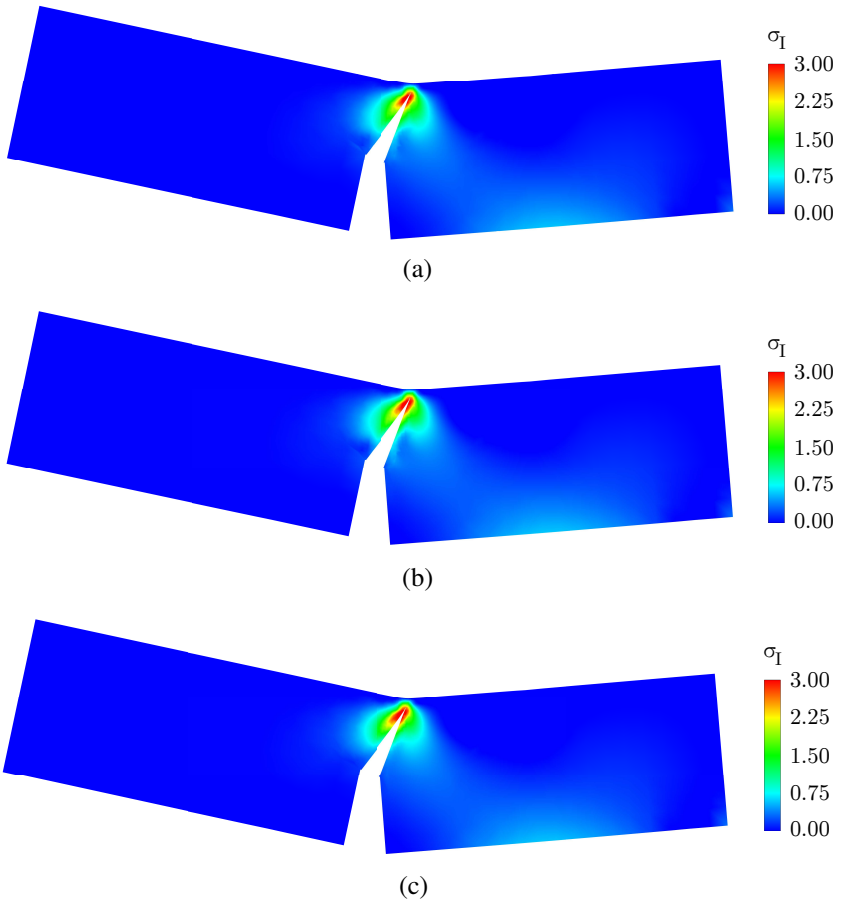

Figure 4.15: First principal stress (N/mm^2) contour at CMOD = 0.2 mm (with displacements amplified 200 times) for: (a) $\lambda = 1$; (b) $\lambda = 2$; and (c) XFEM.

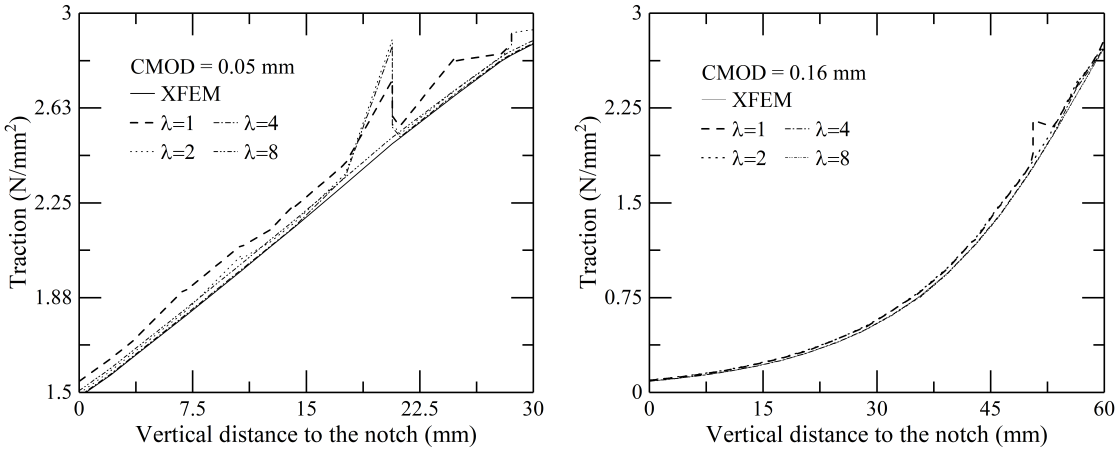

Figure 4.16: Traction profile above the notch at: (a) peak load for CMOD= 0.05 mm: and (b) softening for CMOD= 0.16 mm.

4.5.5 Nooru-mohamed test

A double edge-notched specimen with mixed-mode fracture tested by Nooru (1992) is analysed in this section. The specimen measures $200 \times 200 \times 50$ mm^3, and has two notches with $25 \times 5 \times 50$ mm^3 horizontally at the middle of both left and right edges (see – Figure 4.17). The mesh with 435 bi-linear finite elements is also represented in the same figure. The material properties are given in (Nooru, 1992), where the Young's modulus and Poisson ratio are $E = 30,000$ N/mm^2 and $\nu = 0.2$, respectively, whereas the tensile strength and fracture energy are 3.0 N/mm^2 and 0.11 N/mm, respectively. The isotropic damage model from (Dias-da-Costa et al., 2009) is adopted to describe the discontinuity, where the mixed-mode is taken into account by selecting $\beta = f_{t_0}/c_0 = 0.6$, where f_{t_0} and c_0 are the tensile and cohesive strengths of concrete.

Note that, the cohesion c_0 to calculate β as a crucial factor in constitutive model can be estimated using the Mohr's failure theory for brittle materials (Alfaiate et al., 2002) assuming

a concrete compressive strength of 38 N/mm^2. As a result, $c_0 = 1/2\sqrt{|f_c|\, f_t} \approx 5$ MPa leads to $\beta = f_t/c_0 = 0.6$. Loading is applied by two L-shaped steel frames attached to the specimen

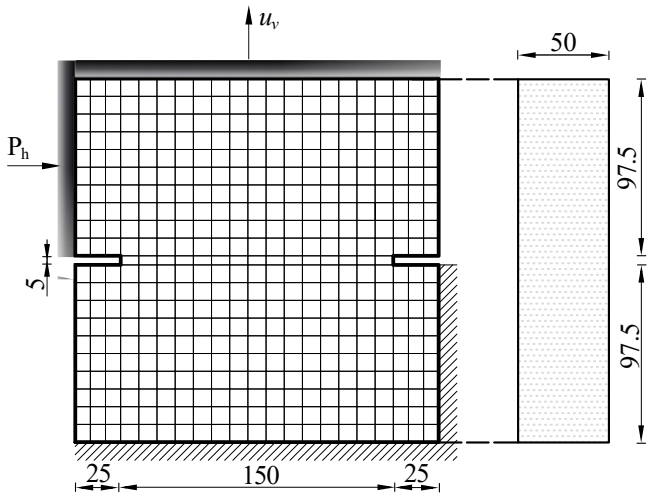

Figure 4.17: Geometry, loading and boundary conditions, and mesh (dimensions in 'mm').

on each side (see – Figure 4.17). A load is first applied horizontally and kept constant at 10^4 N, after which the vertical displacement, u_v, is gradually increased on the top frame until the failure of the specimen. This non-proportional loading scheme causes the direction of the principal stresses to gradually rotate with an increasing vertical displacement. The load *versus* vertical displacement curves for different active lengths are shown in Figure 4.18. The formulation fails to capture the experimental peak load, which was also found in other works in the literature and could be related to deficiencies associated with the load set-up, that could introduce spurious bending stresses and therefore reduce the strength of the specimen during testing (Cervera and Chiumenti, 2006; Gasser and Holzapfel, 2006; Pivonka et al., 2004). However, such a difference does not prevent from assessing the proposed formulation; in particular, it can be again mentioned the nearly matching results among all enrichment choices with $\lambda \geq 2$ and the standard XFEM. In this case, the differences found for $\lambda = 0$ are

not so significant as the ones identified earlier in the single-edge notched beam. This could certainly be related to the constitutive model of the discontinuity which involves mixed-mode and therefore constrains the shear mode more effectively (i.e. reduces the ability to form internal mechanisms) during the analysis.

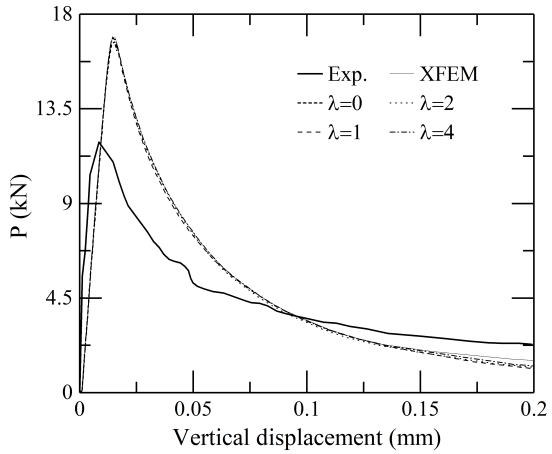

Figure 4.18: Load *versus* vertical displacement for different active lengths superposed with experimental results.

The stress field and crack path are shown in Figure 4.19, which confirms the similarity of results even for the smallest active length. In the traction profile, there is a minor disruption of the field associated with a triangular domain appearing in the early stages of crack propagation in the neighbourhood of the notches for the model with zero active length (see – Figure 4.20.a). This also caused instability in the analysis close to the peak load, which is represented in Figure 4.18. The effect of the non-conforming field completely vanishes for higher active lengths and results from $\lambda = 1$ are in perfect agreement with the standard XFEM.

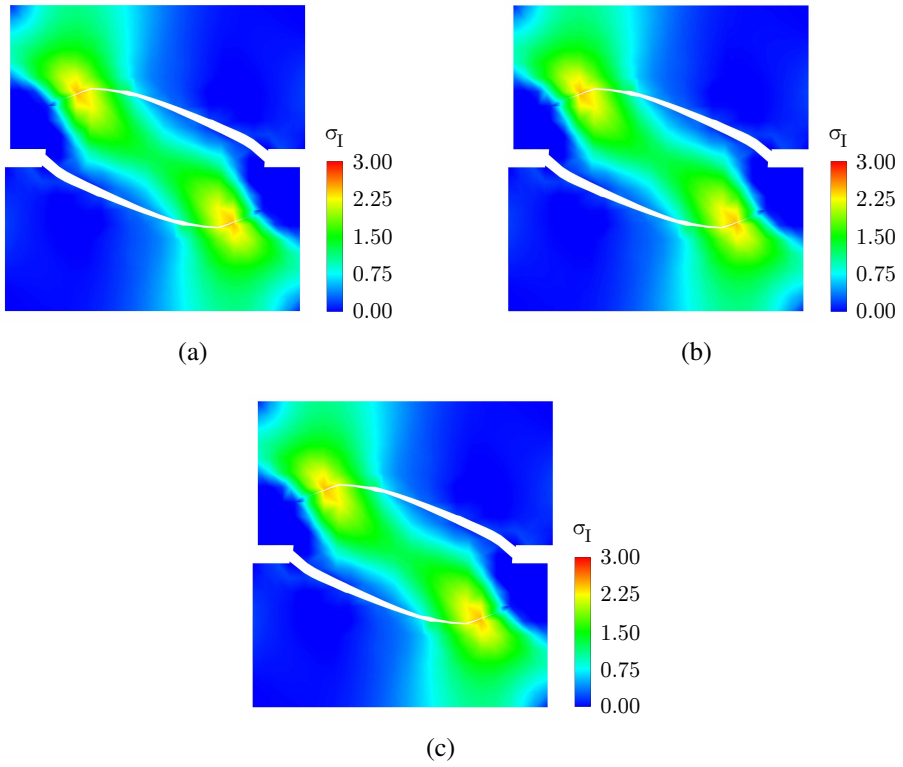

Figure 4.19: First principal stress (N/mm^2) maps at u_v=0.1mm (with displacements amplified 50 times): (a) $\lambda = 1$; (b) $\lambda = 2$; and (c) standard XFEM.

4.5.6 Pre-notched gravity dam model

A gravity dam model tested by Barpi and Valente (2000) with the geometry, boundary conditions and loading scheme represented in Figure 4.21 is simulated in this section. The mesh is composed of $1,848$ bi-linear elements with a noticeable refinement near the notch, which is required to correctly capture the stress and direction of crack propagation. The material properties are provided in (Barpi and Valente, 2000): dead-weight $2,400$ kg/m^3, Young's modulus $35,700$ N/mm^2, Poisson ratio 0.1, tensile strength 3.6 N/mm^2 and fracture energy 0.184 N/mm. An uncoupled mode-I law with exponential softening is adopted for the discontinuity, with the shear stiffness dropping to zero upon crack opening at each integration point. The structure is loaded in two stages, with the weight of the concrete being applied first,

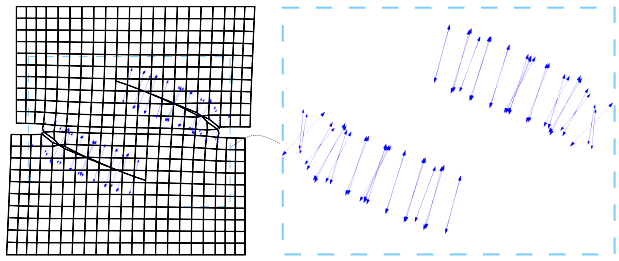

(a)

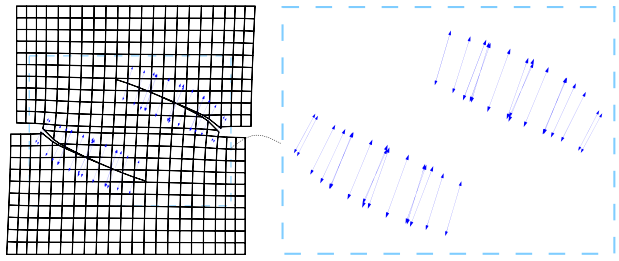

(b)

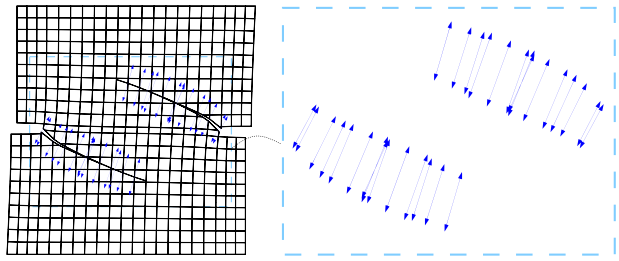

(c)

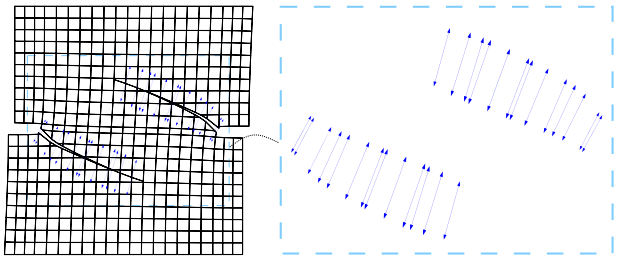

(d)

Figure 4.20: Traction vectors at each integration point at CMOD=0.013 (displacements amplified 500 times) for: (a) $\lambda = 0$; (b) $\lambda = 1$; (c) $\lambda = 2$; and (d) standard XFEM.

followed by the effect of the water pressure which is increased until failure. This is achieved by gradually increasing four concentrated loads which have the same resultant of the pressure

(see – Figure 4.21.a). The arc-length method is used to obtain the solution of the problem by enforcing the monotonic increase of the CMOD.

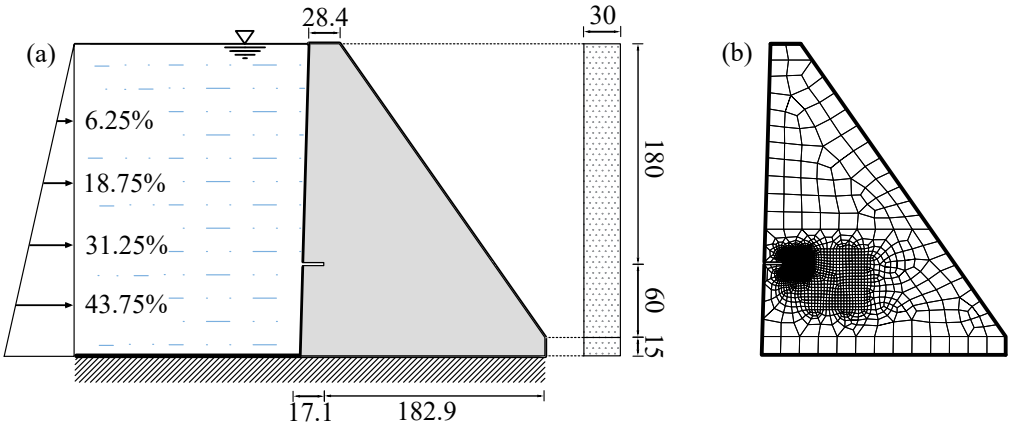

Figure 4.21: Prenotched gravity dam model: (a) geometry (dimensions in 'cm'); and (b) mesh.

Figure 4.22 shows the load *versus* CMOD curves from all simulations. Overall, the simulations capture well the peak load and initial stages of softening. However, the selected contitutive model, which is based on a mode-I law, is unable to correctly approximate the mixed-mode behaviour after the peak load. This insufficiency was already reported by Barpi and Valente (2000) who adopted a similar mode-I model. An active length larger than $\lambda = 0$ provides results showing a very good match with the standard XFEM, although for $\lambda = 1$ some differences can be found for a CMOD$\geq$ 0.25 mm. It should be mentioned though that the active length is here set based on the typical size of the refined mesh around the notch, which means that outside that region the same active length leads to an independent enrichment of each element and this explains the inability apparent at final stages of softening. This effect, however, vanishes for higher active lengths, since they are capable of capturing at least two elements for each enrichment layer in the region around the refinement (and this number was already shown to be enough for a good approximation in other examples). The result

for $\lambda = 0$ is also shown in the figure for completeness, although the instabilities caused by the internal mechanisms do not allow obtaining convergence beyond CMOD$=0.2$ mm. This can also be seen in the deformed mesh, and the stress profile represented in Figure 4.23 and Figure 4.24 respectively.

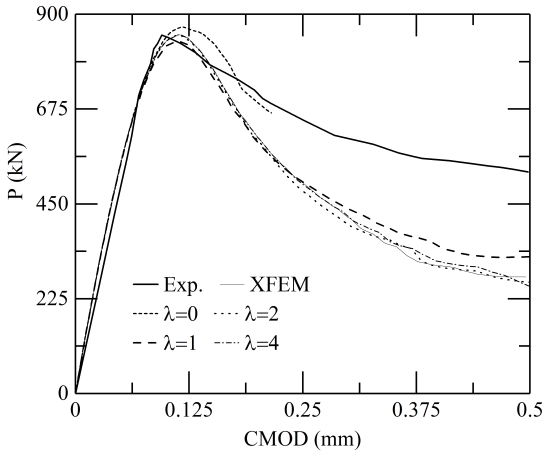

Figure 4.22: Load *versus* CMOD curves superposed with experimental results.

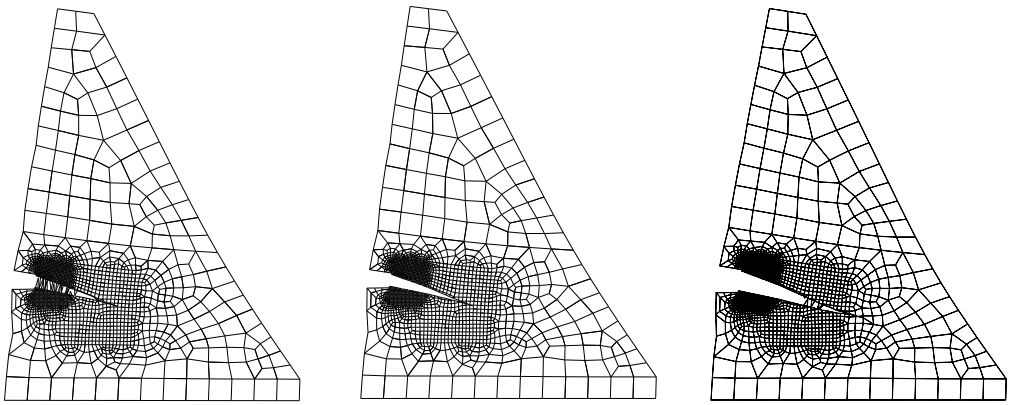

(a) (b) (c)

Figure 4.23: Deformed mesh at CMOD = 0.2 mm for (a) $\lambda = 0$; (b) $\lambda = 1$, and CMOD=0.3 for (c) $\lambda = 1$ (displacements amplified 500 times).

The traction profile is plotted for the various active lengths and standard XFEM in Figure 4.25 when CMOD$=0.028$ mm, where it can be seen the good among all approaches. Again some

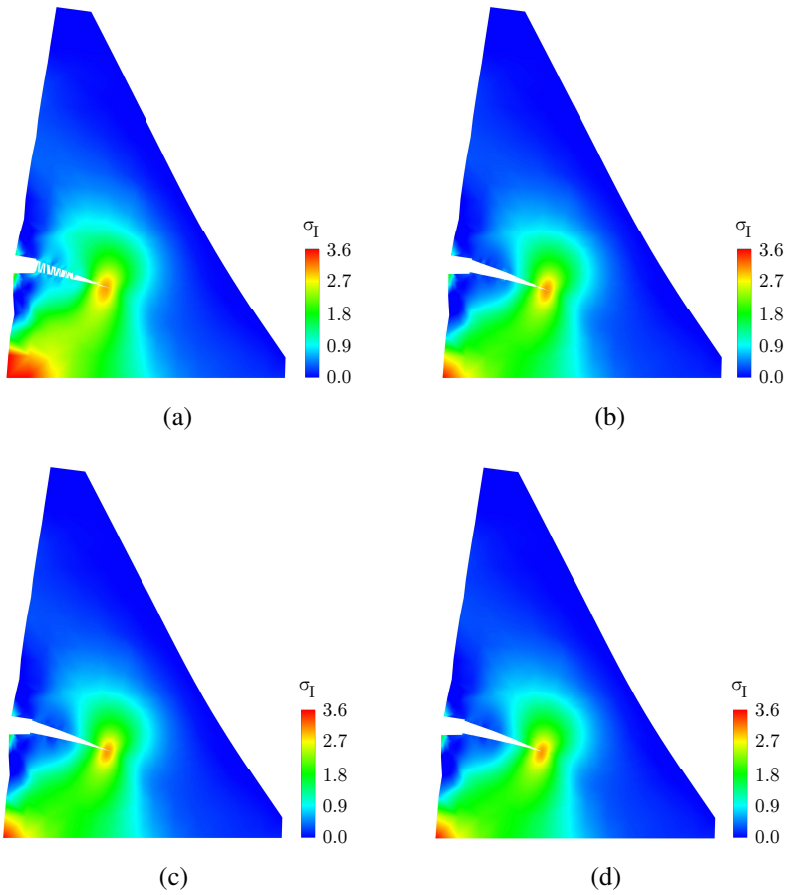

Figure 4.24: Notched gravity dam – maximum principal stress contour at CMOD = 0.2 mm : (a) $\lambda = 0$; (b) $\lambda = 1$; (c) $\lambda = 2$; (d) XFEM (displacements amplified 500 times).

minor oscillations in the profile can be found for the smallest length. Despite the oscillation found, the remaining traction profile is not contaminated, which means that this effect remains local. Such an effect is not present in the simulations with $\lambda \geq 2$.

4.6 Conclusions

This chapter presented a local formulation for XFEM which keeps the number of degrees of freedom, sparsity as well as bandness of the stiffness matrix associated with the underlying

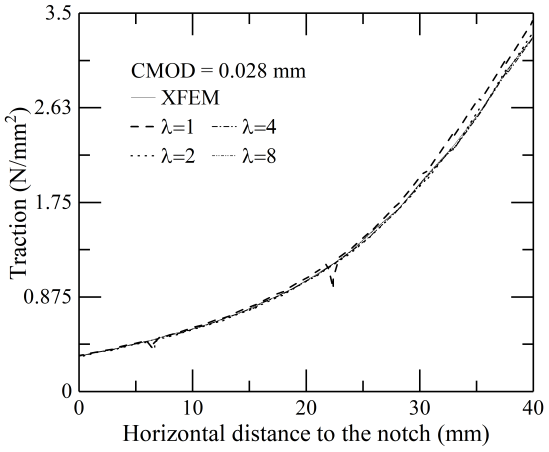

Figure 4.25: Traction profile in front of the notch.

standard finite element mesh fixed. Multi-layer enrichments were used while resolving the singularities related to specific crack geometries. The robustness and accuracy of the method was demonstrated using several element and structure level examples in terms of condition number, crack opening, force-displacement response and traction profile along the cracks.

The local enrichment degrees of freedom were defined based on an active length independent of the remaining cracked elements. Using two element level examples it was shown that enriching each element separately could lead to a singular stiffness matrix when a crack cuts a single node. Enriching pairs of adjacent elements, on the other hand, was enough to prevent any zero energy deformation mode. This, contrary to embedded strong discontinuity approaches, was achieved without the need to eliminate any deformation mode such as linear jumps.

Although only a piece-wise jump continuity was guaranteed due to the active length, the deformed state resembled that of standard XFEM almost perfectly for active lengths above 1. This held true for both element and structure level examples independent of the finite element

mesh, loading direction and traction-jump law. Traction profiles, as a representative of local behaviour, showed oscillations for active lengths of 0 and 1, but become in good agreement with standard XFEM above that. Finally, global (i.e. force-displacement) responses also showed excellent agreement when compared with the standard XFEM results.

CHAPTER 5

Surmount spurious behaviour of PU-based discontinuous elements

---

This chapter presents a new formulation to overcome underlying difficulties in existing PU-based discontinuous elements in the framework of XFEM. The formulation proposed employs polygonal shape functions as an alternative to enrichment layers in conventional XFEM. By doing so, the spurious oscillation of traction profile and fictitious displacement jumps can be naturally overcome.

In section 5.1, the computational issues found with the shape functions of standard finite elements, in particular, quadrilateral elements are discussed, and the results of previous studies are summarised. The polygonal finite element and their interpolants are studied in section 5.2. The enrichment technique employing polygonal interpolants in polygonal enrichment-based XFEM is described in section 5.3. Four different numerical tests are simulated in section 5.4 to assess the robustness of the proposed formulation.

5.1 Computational issue

As discussed briefly in section 2.4.1, PU-based discontinuous elements show a spurious behaviour affecting the traction profile of the discontinuity (Simone, 2004) and consequent

nodal values (Ahmed and Sluys, 2013), specially if higher values of the penalty considered in cohesive zone models. Among the previous studies, Ahmed and Sluys (2013) relate this phenomenon to the unsatisfied moment equilibrium occurring at the interface of quadrilateral elements with bilinear shape functions. The traction between two discontinuity faces needs to be transmitted to the finite element nodes by the equivalent forces. In this situation, the moment couple generated may not be satisfied by $\sum \mathbf{F} = 0$, which results in the fictitious rotation of the interface as represented in Figure 5.1. However, any specific treatment, except for mesh refinement, which would decrease the unbalanced moment at the interface and spurious behaviour, has not been suggested. In fact, the careful selection of the nodal integration scheme, as an alternative, has been found only to alleviate the anomalous behaviour if the discontinuity propagates along with the one of the element local axes. According to previous works, three main conclusions could be drawn:

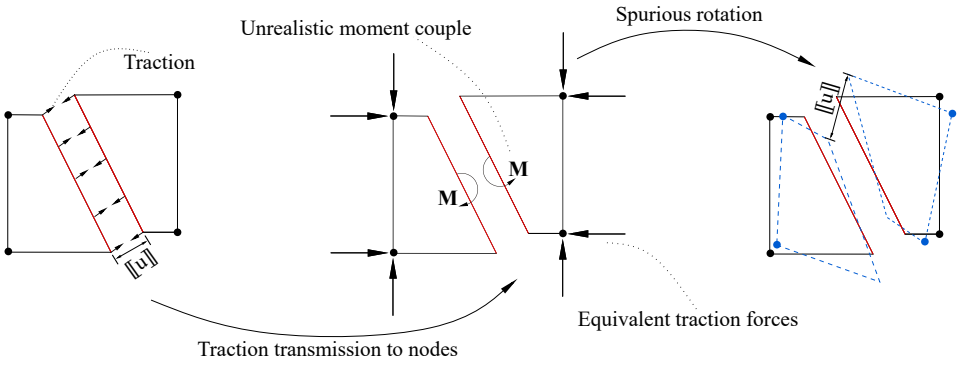

Figure 5.1: Representation of unrealistic moment couple in the transmission of the traction to the equivalent nodal forces.

a) The use of a nodal integration scheme may lead to improving of the results if it removes the pathological coupling while maintaining the natural coupling (Simone, 2004) (see – section 2.4.1). This is so because the inappropriate coupling between

degrees of freedom, which can be considered as one of the main reasons behind the spurious behaviour of PU-based discontinuous elements, is mitigated by nodal integration.

b) The bilinear interpolation used for quadrilateral elements results in unrealistic displacement (e.g. rotational movement) across the discontinuity such that the nodal integration schemes and the mesh refinement cannot completely treat this phenomenon (Ahmed and Sluys, 2013).

c) If the discontinuity propagates parallel to one of the element local axes, despite using bilinear interpolation functions, appropriate results can be obtained with nodal integration (Ahmed and Sluys, 2013).

According to Ahmed and Sluys (2013), bilinear finite elements as a family member of PU-based discontinuous elements cannot interpolate the strain field appropriately across the discontinuity in most cases, which contaminates the stress field over the corresponding element. However, this cannot be the only reason due to c).

Moreover, as represented in Figure 5.2, the interaction between nodes 2 and 1, and between 2 and 3 are considered as natural coupling. In contrast, the interaction between nodes 2 and 4 generates pathological coupling, which leads to spurious oscillation (Simone, 2004). As a consequence, treatment is required to avoid pathological coupling in PU-based element.

To sum up, the information obtained from previous studies reveal that the standard interpolation functions cannot describe the kinematics of discontinuity inside the corresponding

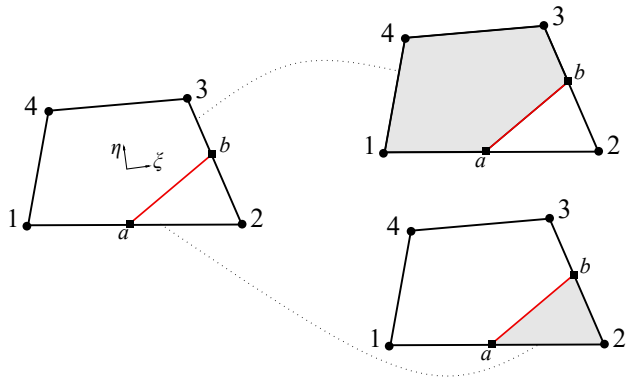

Figure 5.2: Representation of polygonal parts formed in a quadrilateral element with corner cut (regular and additional nodes are represented by black circle and square respectively).

element. In fact, using the inappropriate interpolation function leads to pathological coupling, which provides the element with fictitious freedom generating spurious oscillation.

In the following sections, polygonal element shape functions are proposed to enrich the interpolation function used in bilinear finite elements to overcome the difficulties mentioned above.

5.2 Polygonal shape functions

As discussed in section 5.1, adopting shape functions suitable for the two separate domain cut by a crack could interpolate the corresponding displacement/strain field more accurately. According to Simone (2004), using the isoparametric shape functions for conventional linear and quadratic interface elements results in the construction of the pathological coupling in the corresponding stiffness matrix. Pathological couplings relate the degrees of freedom together that are not naturally coupled in an element. Accordingly, this thesis aims to use the polygonal shape functions to avoid these inappropriate coupling between degrees of

freedom. For irregular polygons, Wachspress (see – Appendix A) and Laplace (Sukumar and Tabarraei, 2004; Wachspress, 1971) interpolants can be employed as polygonal interpolants. For enrichment, Laplace shape functions realised as natural neighbour-based interpolants are used in the present study.

Laplace interpolants

Sibson (1980) introduced natural neighbour interpolation as an approach to fit and smooth the data. The Laplace interpolant, also called natural neighbour interpolants, is computationally more attractive than Sibson interpolant (Sukumar and Tabarraei, 2004).

As depicted in Figure 5.3, if there is a common Voronoi edge for point P and node P_i in Voronoi cell, P_i is called a natural neighbor of the P. Accordingly, the Laplace shape function for node P_i is given by (Christ et al., 1982):

$$\varphi_i^l(\mathbf{x}) = \frac{\alpha_i(\mathbf{x})}{\sum_{j=1}^{n} \alpha_j(\mathbf{x})}, \tag{5.1}$$

$$\alpha_j(\mathbf{x}) = \frac{s_j(\mathbf{x})}{h_j(\mathbf{x})}, \quad \mathbf{x} \in \mathbb{R}^2 \tag{5.2}$$

where $\alpha_i(\mathbf{x})$ denotes Laplace weight function, $s_j(\mathbf{x})$ is the length of Voronoi edge between point P and node P_i, and $h_j(\mathbf{x})$ shows the Euclidean distance between P and P_i, as represented in Figure 5.3.

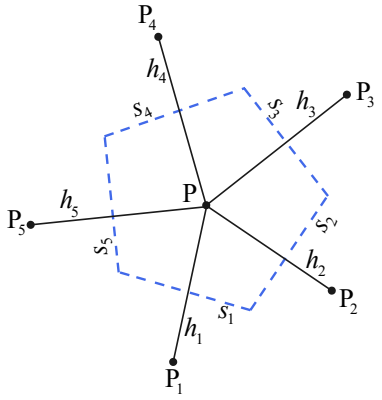

Figure 5.3: Voronoi diagram of point P.

Since the Laplace interpolant meets all properties discussed in Appendix A2 and essential boundary condition with a Galerkin procedure required for finite elements, Laplace interpolant is utilised herein.

5.3 XFEM enrichment by polygonal interpolant

In this section, a polygonal interpolant is utilised to overcome the difficulties due to some limitations in XFEM, whose enrichment is provided by the second layer of degrees of freedom (Dias-da-Costa et al., 2010). To this end, the interpolation functions conventionally used by XFEM to interpolate the enrichment layer are replaced by polygonal shape functions. It is worth mentioning that the polygonal shape function is chosen according to the shape of each subdomain defined by the discontinuity passing through the corresponding element. Consequently, if the finite element is separated into two quadrilaterals, a quadrilateral Laplace shape function would be recovered to interpolate the field on enrichment layer, otherwise pentagonal and triangular Laplace shape functions are utilised in the case of quadrilateral elements.

As represented in Figure 5.4, since the enrichment layer in conventional XFEM treats the displacement jump, the physical meaning of the discontinuity cannot be interpreted explicitly. Conversely, the XFEM enriched by polygonal interpolants can position the additional nodes at the discontinuity and solves this incompatibility.

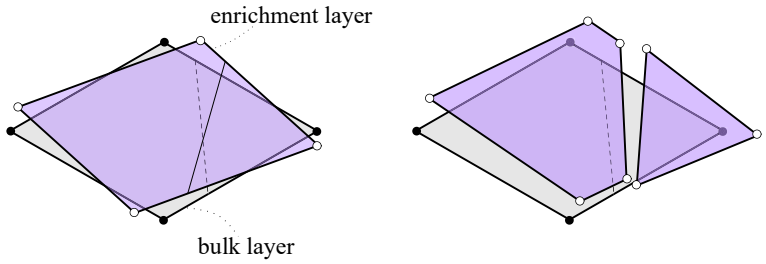

Figure 5.4: Representation of the enrichment difference: (a) conventional XFEM and (b) XFEM enriched by polygonal interpolant (black and white nodes show regular and additional nodes respectively).

5.3.1 Finite element discretisation

The variational form of an elasto-static boundary value problem with a strong discontinuity is given in Equation (2.13).

The total displacement field as a summation of continuous and discontinuous fields is given as follows:

$$\mathbf{u}(\mathbf{x}) = \mathbf{N}(\mathbf{x})\hat{\mathbf{a}} + \mathscr{H}_{\Gamma_d}\overline{\mathbf{N}}(\mathbf{x})\tilde{\mathbf{a}}, \tag{5.3}$$

In Equation (5.3), $\mathbf{N}(\mathbf{x})$ and $\hat{\mathbf{a}}$ represent respectively the usual finite element shape functions and nodal displacements associated with the continuous field. $\overline{\mathbf{N}}(\mathbf{x})$ and $\tilde{\mathbf{a}}$ on the other hand, represent Laplace shape functions and enhanced nodal displacements defined at polygon

vertices (see – Figure 5.2). Nodal displacement decomposition can also be written similar to Equation (5.3) as follows:

$$\mathbf{a} = \hat{\mathbf{a}} + \mathbf{H}_{\Gamma_d}\tilde{\mathbf{a}}, \tag{5.4}$$

where $\mathbf{H}_{\Gamma_d} = (\mathscr{H}_{\Gamma_d}\mathbf{I} \mid \mathbf{0})$ is the augmented polygonal Heaviside matrix. $\mathscr{H}_{\Gamma_d}$ represents the Heaviside function which is chosen as 0 and 1 over Ω^- and Ω^+, respectively, while $\mathbf{I}$ is the square identity matrix with dimensions of underlying cracked element. In addition, considering that enhanced nodal displacements on the crack ends do not contribute to those on the regular nodes (Kronecker-delta property), $\mathbf{0}$ is defined as a zero rectangular matrix with 4 columns. The use of Equation (5.4) directly in the variational form given in Equation (2.13) would lead to blending elements similar to conventional XFEM (Belytschko and Black, 1999). In order to eliminate the additional computational cost and implementation complexity associated with those elements, an alternative approach is adopted here. Using the change of variables $\hat{\mathbf{a}} = \mathbf{a} - \mathbf{H}_{\Gamma_d}\tilde{\mathbf{a}}$, Equation (5.3) is recast as follows:

$$\mathbf{u}(\mathbf{x}) = \mathbf{N}(\mathbf{x})\mathbf{a} + \left(\mathscr{H}_{\Gamma_d}\overline{\mathbf{N}}(\mathbf{x}) - \mathbf{N}(\mathbf{x})\mathbf{H}_{\Gamma_d}\right)\tilde{\mathbf{a}}, \tag{5.5}$$

Inserting Equation (5.5) back in Equation (2.13) the following is obtained:

$$\begin{aligned} &-\int_{\Omega\setminus\Gamma_d}\left[\mathbf{B}\delta\mathbf{a}+(\mathscr{H}_{\Gamma_d}\overline{\mathbf{B}}-\mathbf{BH})\delta\tilde{\mathbf{a}}\right]^T\mathbf{D}\left[\mathbf{Ba}+(\mathscr{H}_{\Gamma_d}\overline{\mathbf{B}}-\mathbf{BH})\tilde{\mathbf{a}}\right]\,\mathrm{d}\Omega \\ &-\int_{\Gamma_d}\left[\overline{\mathbf{N}}\delta\tilde{\mathbf{a}}\right]^T\mathbf{T}_d\left[\overline{\mathbf{N}}\tilde{\mathbf{a}}\right]\,\mathrm{d}\Gamma+\int_{\Omega\setminus\Gamma_d}\left[\mathbf{N}\delta\mathbf{a}+(\mathscr{H}_{\Gamma_d}\overline{\mathbf{N}}-\mathbf{NH})\delta\tilde{\mathbf{a}}\right]^T\mathbf{b}\,\mathrm{d}\Omega \\ &\qquad+\int_{\Gamma_t}\left[\mathbf{N}\delta\mathbf{a}+(\mathscr{H}_{\Gamma_d}\overline{\mathbf{N}}-\mathbf{NH})\delta\tilde{\mathbf{a}}\right]^T\bar{\mathbf{t}}\,\mathrm{d}\Gamma=0, \end{aligned} \tag{5.6}$$

By progressively taking $\delta\tilde{\mathbf{a}}=0$ and $\delta\mathbf{a}=0$ in Equation (5.6), the following discretised equilibrium equations can be obtained in terms of total and discontinuous nodal displacements:

$$\begin{bmatrix}\mathbf{K}_{aa} & \mathbf{K}_{a\tilde{a}}\\ sym & \mathbf{K}_{\tilde{a}\tilde{a}}+\mathbf{K}_d\end{bmatrix}\begin{Bmatrix}\mathbf{a}\\ \tilde{\mathbf{a}}\end{Bmatrix}=\begin{Bmatrix}\mathbf{f}_a\\ \mathbf{f}_{\tilde{a}}\end{Bmatrix}, \tag{5.7}$$

with the stiffness and force terms defined as follows:

$$\mathbf{K}_{aa}=\int_\Omega\mathbf{B}^T\mathbf{DB}\,\mathrm{d}\Omega, \tag{5.8}$$

$$\mathbf{K}_{a\tilde{a}}=\mathbf{K}_{B\overline{B}}-\mathbf{K}_{aa}\,\mathbf{H},\ \text{where}\ \mathbf{K}_{B\overline{B}}=\int_{\Omega^+}\mathbf{B}^T\mathbf{D}\overline{\mathbf{B}}\,\mathrm{d}\Omega \tag{5.9}$$

$$\mathbf{K}_{\tilde{a}\tilde{a}}=\mathbf{K}_{\overline{BB}}-\mathbf{K}_{B\overline{B}}^T\,\mathbf{H}-\mathbf{H}^T\mathbf{K}_{B\overline{B}}+\mathbf{H}^T\mathbf{K}_{aa}\mathbf{H},\ \text{where}\ \mathbf{K}_{\overline{BB}}=\int_{\Omega^+}\overline{\mathbf{B}}^T\mathbf{D}\overline{\mathbf{B}}\,\mathrm{d}\Omega \tag{5.10}$$

$$\mathbf{K}_d=\int_{\Gamma_d}\overline{\mathbf{N}}^T\mathbf{T}_d\,\overline{\mathbf{N}}\,d\Gamma, \tag{5.11}$$

$$\mathbf{f}_a=\int_\Omega\mathbf{N}^T\mathbf{b}\,d\Omega+\int_{\Gamma_t}\mathbf{N}^T\bar{\mathbf{t}}\,d\Gamma, \tag{5.12}$$

$$\mathbf{f}_{\tilde{a}} = \int_{\Omega^+} \overline{\mathbf{N}}^T \mathbf{b}\, d\Omega + \int_{\Gamma_t^+} \overline{\mathbf{N}}^T \bar{\mathbf{t}}\, d\Gamma - \mathbf{H}^T \mathbf{f}_a, \tag{5.13}$$

where $\square^T$ stands for transpose, while $\mathbf{B}$ and $\overline{\mathbf{B}}$ correspond to the strain displacement matrices of the conventional underlying element and polygon enrichment counterpart, respectively. Given that the bulk is assumed linear isotropic, the properties of the Voigt notation were explored to make use of stiffness matrix $\mathbf{D}$ and matrix multiplication in Equations (5.8)–(5.10). Finally, $\mathbf{f}_a$ and $\mathbf{f}_{\tilde{a}}$ define the vectors of external forces applied on the regular and enriched degrees of freedom.

5.3.2 Integration procedure

According to Equations (5.8)-(5.13), integration over the underlying conventional finite element and enrichment polygon domains are required. While any standard quadrature rule can be adopted for the former, in case of latter, the integrals are carried out on triangular sub-regions defined by the centroid of a polygon and its vertices (Dias-da-Costa et al., 2010; Moës et al., 1999; Park et al., 2009; Sukumar and Tabarraei, 2004). For this, the integration points over the parent triangular element are first mapped to the physical sub-triangular region (see – Figure 5.5). This is given in line 6 of the Algorithm 5.1. However, the shape functions are defined on the canonical elements for both conventional finite element and polygon element. Therefore, the corresponding location of the integration point on the physical domain must be obtained in the coordinate system of the canonical element. This is performed using a simple Newton-Raphson (NR) procedure (Sukumar and Tabarraei, 2004) as given in lines 7 and 9 of the Algorithm 5.1 for polygonal and underlying finite elements, respectively. The

input arguments in the pseudocode, n, n_{int}, $\mathbf{x}_{el}$, and $\mathbf{x}_{crack}$ represent the number of polygon nodes, number of integration points in the triangular parent element, nodal coordinates of the underlying mesh, and crack end counterparts.

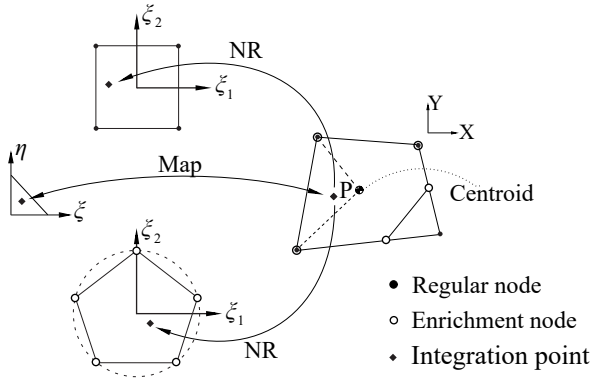

Figure 5.5: Isoparametric mapping for canonical element.

The shape function derivatives in the physical coordinate system for polygon elements are obtained similarly to conventional finite elements as follows:

$$\begin{Bmatrix} \frac{\partial \overline{\mathbf{N}}_i}{\partial \mathbf{x}} \\ \\ \frac{\partial \overline{\mathbf{N}}_i}{\partial \mathbf{y}} \end{Bmatrix} = \underbrace{\begin{bmatrix} \frac{\partial \xi}{\partial \mathbf{x}} & \frac{\partial \eta}{\partial \mathbf{x}} \\ \\ \frac{\partial \xi}{\partial \mathbf{y}} & \frac{\partial \eta}{\partial \mathbf{y}} \end{bmatrix}}_{\mathbf{J}^{-1}} \begin{Bmatrix} \frac{\partial \overline{\mathbf{N}}_i}{\partial \xi} \\ \\ \frac{\partial \overline{\mathbf{N}}_i}{\partial \eta} \end{Bmatrix} \tag{5.14}$$

Finally, the integral carried over Γ_d is calculated using a Newton–Cotes scheme with two integration points for each crack.

5.4 Numerical examples

In this section, three numerical examples are simulated to explore the effectiveness of proposed formulation on alleviation of spurious behaviour of PU-based discontinuous elements. To this

Algorithm 5.1 Integration over Ω^+

procedure ENRICHMENT INTEGRATION($n, n_{int}, \mathbf{x}_{el}, \mathbf{x}_{crack}$)
  $F \leftarrow 0$, (initialising F $\simeq \int_{\Omega^+} f\, d\Omega$ – see Eqs. (5.9)- (5.11) and (5.13))
  for $i = 1 : n$ **do**
    $\mathbf{J}^i \leftarrow \begin{bmatrix} \frac{\partial \mathbf{x}}{\partial \xi} & \frac{\partial \mathbf{y}}{\partial \xi} \\ \frac{\partial \mathbf{x}}{\partial \eta} & \frac{\partial \mathbf{y}}{\partial \eta} \end{bmatrix}$, (Jacobian matrix)
    for $j = 1 : n_{int}$ **do**
      $\mathbf{x}_P \leftarrow \sum_{k=1}^{3} \mathbf{N}_k(\xi_{P_j}, \eta_{P_j})\mathbf{x}_k$, (map)
      $\xi_P^{n-gon} \leftarrow f(\xi_\mathbf{1}, \xi_\mathbf{2}) = \mathbf{x}_P - \sum_{k=1}^{n} \overline{\mathbf{N}}_k(\xi_1, \xi_2)\mathbf{x}_k = 0$, (Newton-Raphson)
      obtain $\overline{\mathbf{N}}$ & $\nabla\overline{\mathbf{N}}$, for sub-triangle i and integration point j
      $\xi_P^{bulk} \leftarrow f(\xi_\mathbf{1}, \xi_\mathbf{2}) = \mathbf{x}_P - \sum_{k=1}^{4} \mathbf{N}_k(\xi_1, \xi_2)\mathbf{x}_k = 0$, (Newton-Raphson)
      obtain $\mathbf{N}$ & $\nabla\mathbf{N}$ for sub-triangle i and integration point j
      $F \leftarrow F + f_{ij}|\mathbf{J}^i|\mathbf{w}^j$
    end for
  end for
  return F
end procedure

end, section 5.4.1 is devoted to studying on anomalous displacement jump in the interface by single element test. In section 5.4.2, an investigation is conducted on the oscillation in traction profile by Linear elastic notched beam test. section 5.4.3 is dedicated to assessing the robustness of the developed formulation in the analysis of delamination problems. Eventually, the accuracy of the proposed formulation is discussed by a structural example in section 5.4.4.

5.4.1 Single element test

In order to investigate the PU based methods and spurious behaviour of the bilinear quadrilateral element, a single element test is simulated by Ahmed and Sluys (2013) (see – Figure 5.6), where the anomalous displacement jump (crack opening) is taken into consideration. To this

end, a finite element with unstructured mesh and unparalleled discontinuity to the edges of the elements is considered (see – Figure 5.7).

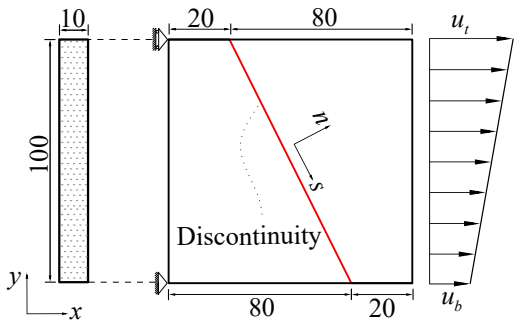

Figure 5.6: Single element test: geometry and boundary conditions.

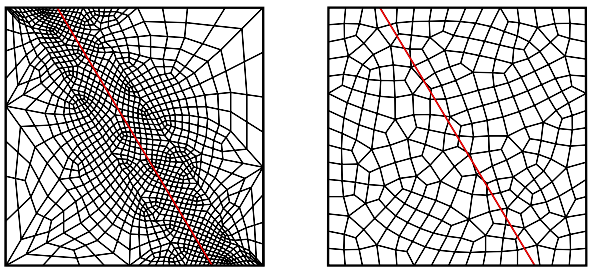

(a) (b)

Figure 5.7: Representation of adopted meshes for single element test: (a) fine mesh (b) coarse mesh.

The material proprieties are given as: the bulk is treated as linear elastic, with a Young's modulus of 40 GPa and a Poisson ration equals zero (Ahmed and Sluys, 2013). An Isotropic damage law (see– section 2.2.2) is assumed for discontinuity, where the normal and tangential penalties $k_n = k_s = 10^5\,\mathrm{N/mm^3}$.

As represented in Figure 5.6, a prescribed displacement is applied to the right surface of the single element structure by displacement control method. Two loading conditions can be considered for this structure to model the uniform and nonuniform crack opening. The

former is modelled by uniform prescribed displacement $u_b = u_t = 10^{-3}$mm. In the later, a prescribed linear displacement is imposed along the right surface of the structure while $u_b = 0$ and $u_t = 10^{-3}$mm. The Newton-Cotes/Lobatto integration scheme is considered for numerical integration of the bulk and corresponding discontinuity.

The numerical results are compared to the analytical solution of the problem, leading to the total load $\mathrm{P} = 398.6327\mathrm{N}$ applied at the loading ends with the displacement jumps $[\![\mathbf{u}]\!]_x = 3.4182 \times 10^{-6}$mm and $[\![\mathbf{u}]\!]_y = 0$ along the x and y axes respectively.

As depicted in Figure 5.8, the displacement jump along x-axis has an excellent agreement with reference solution for uniform and nonuniform crack opening. These results reveal that the polygonal interpolation function can remove the pathological coupling between degrees of freedom. Besides, the unstructured meshes adopted herein indicate that polygonal enrichment is such effective that the discontinuity can propagate arbitrarily through the elements without the need to be parallel to the corresponding elements of local axes.

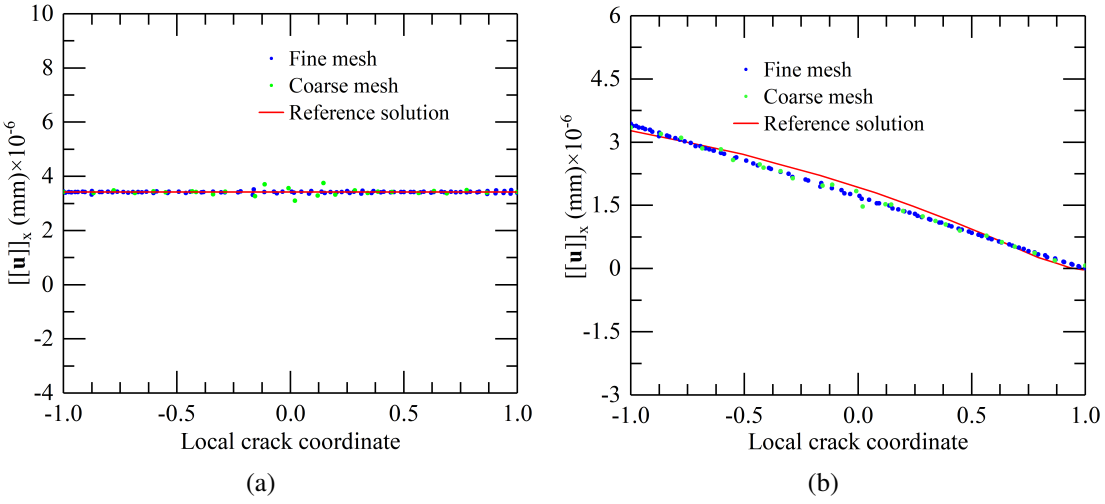

Figure 5.8: Horizontal displacement jump for single element test: (a) uniform crack opening (b) nonuniform crack opening.

In Figure 5.9, the traction profiles for finer mesh indicate that the standard XFEM enrichment cannot provide stable traction map along with the crack faces during the uniform crack opening even for the penalty with small value (i.e. $10^3\,\mathrm{N/mm^3}$). On the contrary, polygonal enrichment formulation shows flawless performance on traction profiles along with the X and Y axes. Similarly, in Figure 5.10, the traction considerably deviates applying higher penalty parameters for standard XFEM formulation whereas this trend remains stable for proposed formulation and the difference between traction values is related to higher stiffness applied for the interface as the penalty parameter.

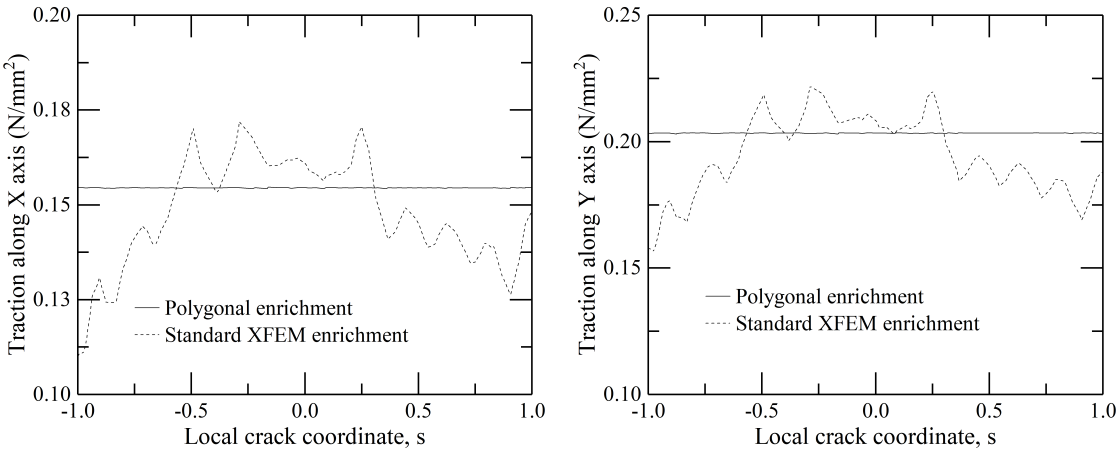

Figure 5.9: Traction profile for uniform crack opening: (a) along X axis (b) along Y axis.

The corresponding results for non-uniform opening along with the X and Y axes are represented in Figure. 5.11. Significant oscillations are found in the traction profile in the case of standard XFEM, which confirms the reported difficulties in capturing traction profiles in the presence of the high penalties in stiff interface problems (Aragón and Simone, 2017; Dias-da-Costa et al., 2010; Simone, 2004).

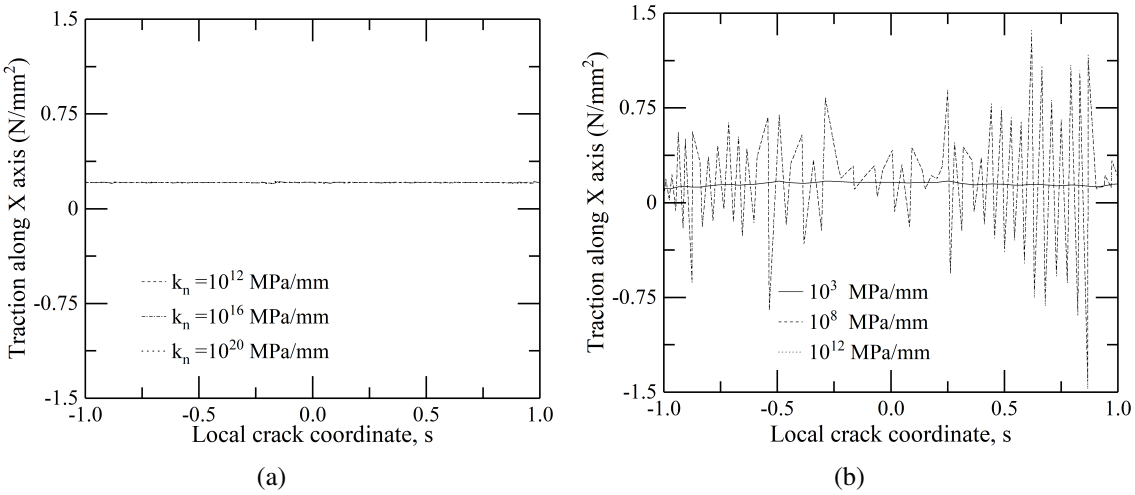

Figure 5.10: Traction profile of uniform crack opening: (a) polygonal enrichment (b) standard XFEM enrichment for different penalty parameters.

The effect of the stiffness of the interface is presented in Figure 5.12. Interestingly, only for a relatively soft discontinuity (i.e. $10^3\,\mathrm{MPa/mm}$), standard XFEM provides a smooth traction profile along the crack. The oscillatory phenomenon becomes worst with increasing stiffness, and severe oscillations appear for the highest tier. In the case of the polygonal enrichment approach, the oscillations are effectively avoided and the solution remains nearly unchanged even when the stiffness is increased from stiff (i.e. $10^8\,\mathrm{MPa/mm}$) to very stiff (i.e. $10^{20}\,\mathrm{MPa/mm}$).

5.4.2 Linear elastic notched beam

Rots (1988) introduced a linear elastic test to examine the conventional interface elements. Dias-da-Costa et al. (2010) and Simone (2004) used this test to study the difficulty of traction oscillation in XFEM by focusing on numerical integration schemes. In this section, this test is

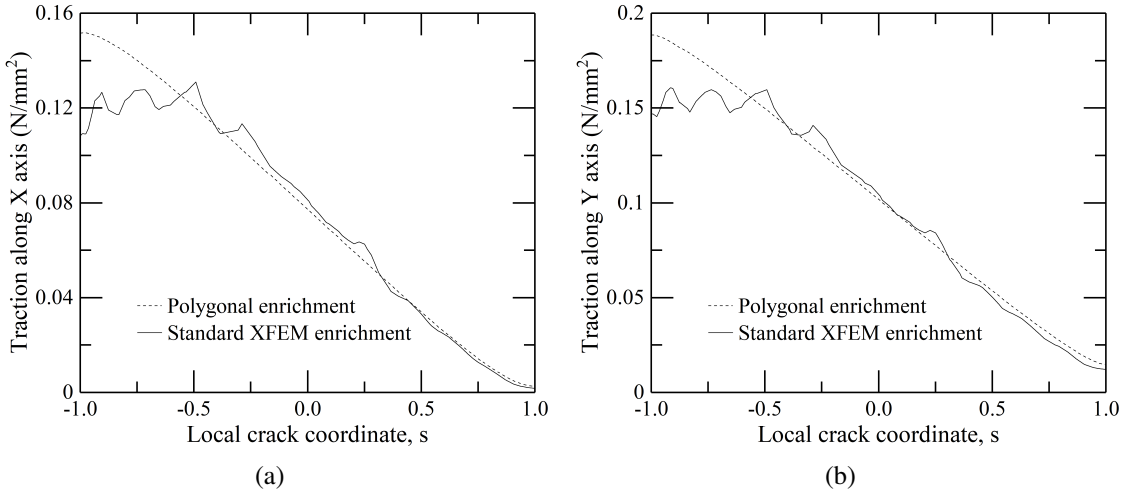

Figure 5.11: Traction profile for non-uniform crack opening: (a) along X axis (b) along Y axis.

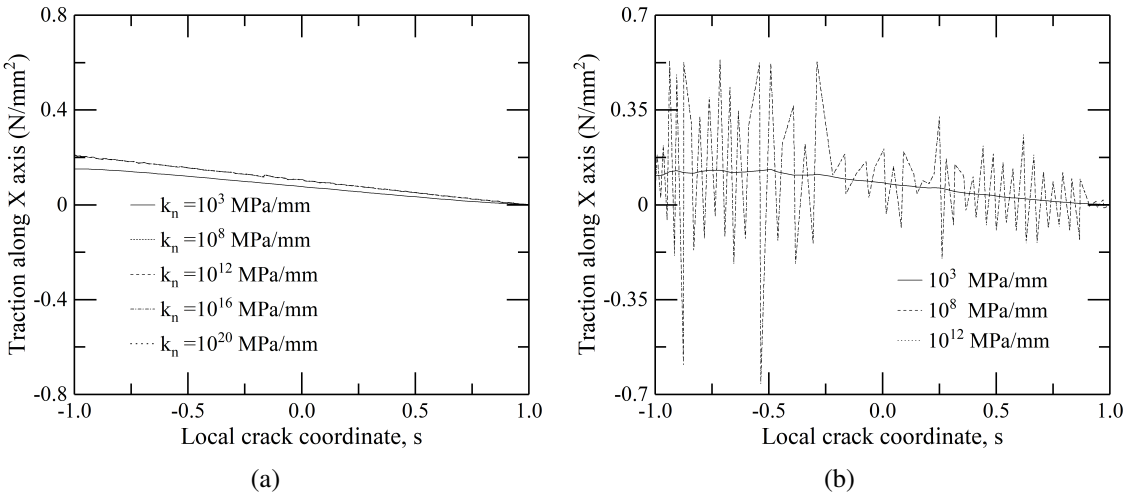

Figure 5.12: Traction profile of non-uniform crack opening: (a) polygonal enrichment (b) standard XFEM enrichment for different penalty parameters.

used to investigate the effectiveness of polygonal enrichment on XFEM and its problem with traction profile. The four-node quadrilateral elements are utilised under plane stress condition.

As depicted in Figure 5.13, the discontinuity is located at the centre of the beam and the material properties are assumed as : the Young's modulus equals 20000$\mathrm{N/mm^2}$ and Poisson's ratio is considered 0.2 for the bulk (Simone, 2004).

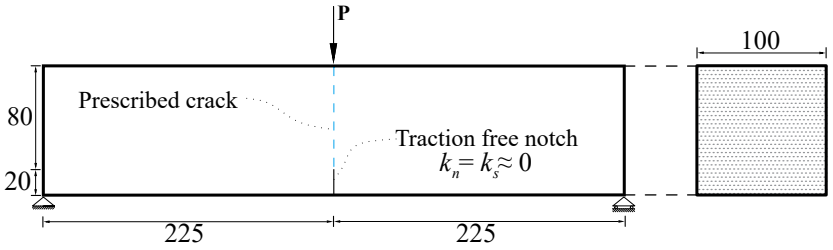

Figure 5.13: Linear elastic notched beam: geometry and boundary condition.

The load of P = 1 kN is imposed to the beam. As depicted in Figure 5.14, an unstructured mesh and structured mesh are adopted herein. The notch with 20 mm depth is considered as a traction free discontinuity ($k_n = k_s = 0$). The high value penalty parameters are adopted for the prefect contact and the horizontal displacement jump should be activated to simulate the pure mode-I.

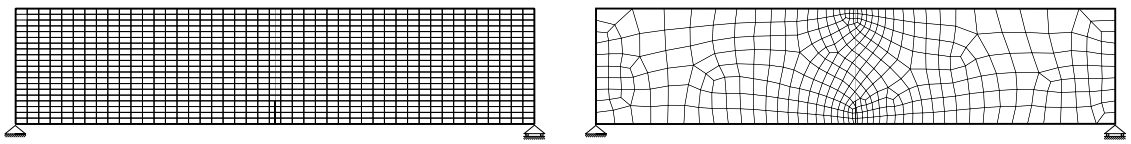

Figure 5.14: Representation of adopted meshes for Linear elastic notched beam: (a) structured mesh (b) unstructured mesh.

The traction profile of linear elastic notched beam for polygonal and standard XFEM enrichments by Newton–Cotes/Lobatto integration scheme is represented in Figure 5.15 and Figure 5.16, respectively for structured and unstructured meshes adopted. The results indicate that the polygonal enrichment can remove the spurious oscillation in traction profile of quadrilateral element by using Newton–Cotes/Lobatto integration scheme, whereas bilinear shape functions utilised in standard XFEM leads to spurious behaviour in the unstructured meshed model.

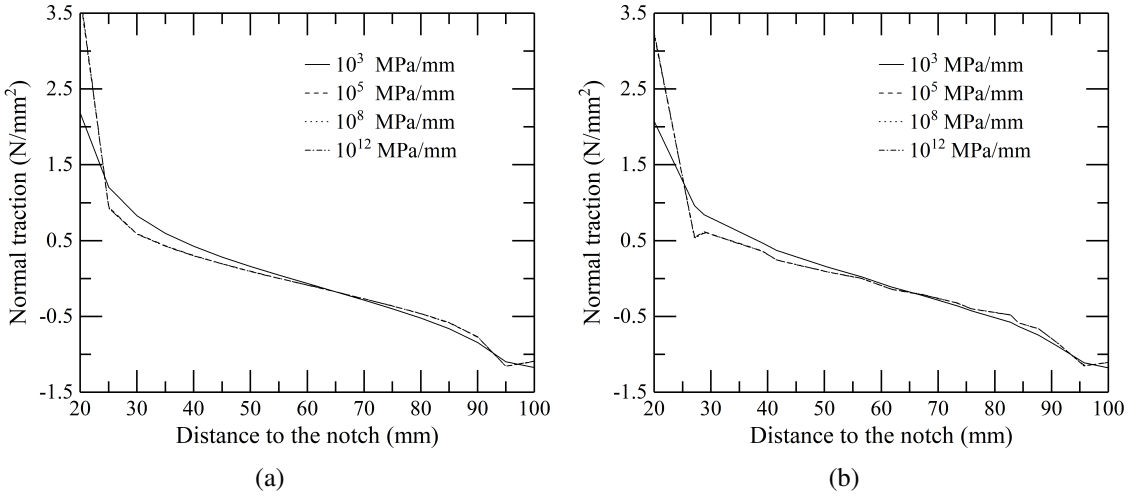

Figure 5.15: Linear elastic notched beam – traction profile in front of the notch with polygonal enrichment and Newton-Cotes/Lobatto with two points for different penalty parameters: (a) structured mesh (b) unstructured mesh.

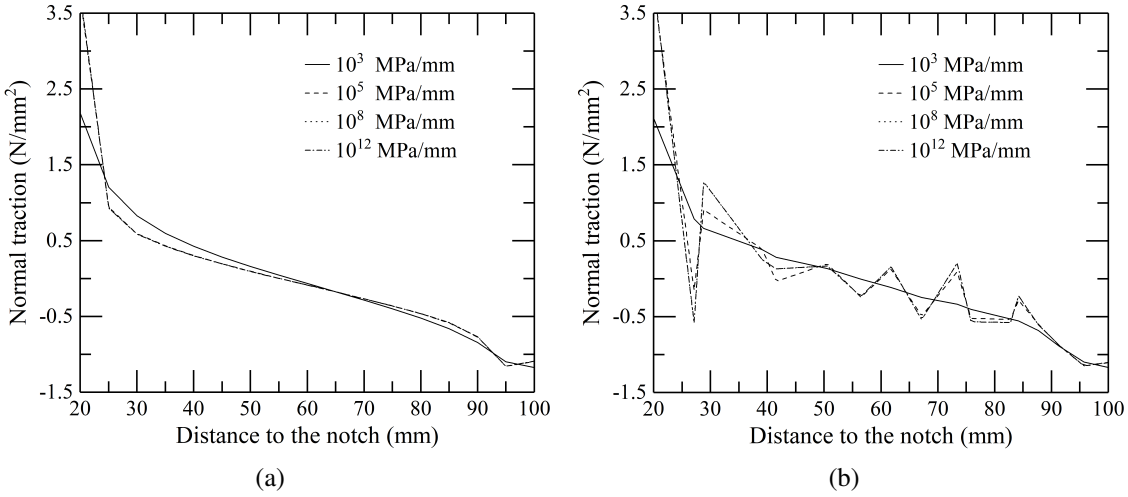

Figure 5.16: Linear elastic notched beam – traction profile in front of the notch with standard XFEM enrichment and Newton-Cotes/Lobatto with two points for different penalty parameters: (a) structured mesh (b) unstructured mesh.

Figure 5.17a, in contrast to the results of standard XFEM enrichment (see – Figure 5.17b), indicates that the polygonal enrichment can omit the spurious oscillation in traction profile even though any local axes of the cracking elements are not along with the crack path.

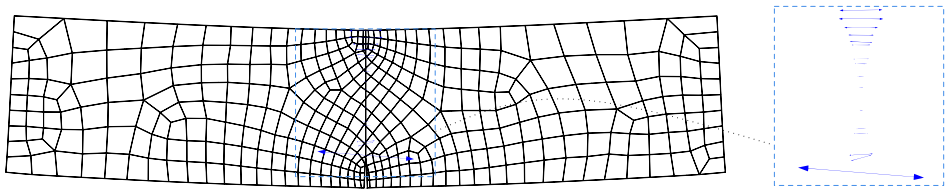

(a)

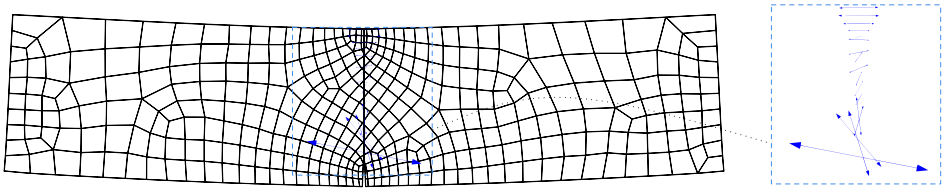

(b)

Figure 5.17: Linear elastic notched beam – representation of traction vectors for unstructured mesh by means of Newton-Cotes/Lobatto : (a) Polygonal enrichment (b) standard XFEM enrichment.

5.4.3 Peel test

A double-cantilever beam tested by Remmers et al. (2001) is simulated to assess the ability of the proposed formulation to analyse the delamination or interface problems.

The beam consists of two layers with equal thickness and identical material properties. As depicted in Figure 5.18, the reference beam is $10 \times 1 \times 1\,\mathrm{mm}^3$ with a 1 mm traction-free notch, which is loaded by the peel forces at the right end. The material properties given are assumed: the Young's modulus $E = 100\,\mathrm{N/mm}^2$; Poisson ration $\nu = 0.3$; tensile strength $f_t = 1\,\mathrm{N/mm}^2$ and fracture energy $G_F = 0.1\,\mathrm{N/mm}$ (Remmers et al., 2001).

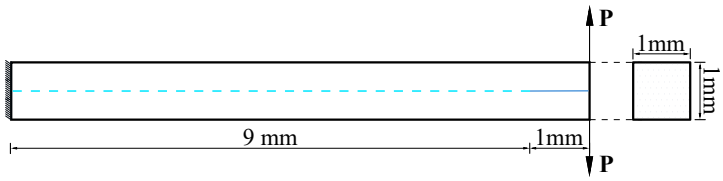

Figure 5.18: Peel test: geometry and boundary conditions.

The fracture mode-I is assumed as the dominant fracture mode. Consequently, shear traction is considered to be zero. As represented in Figure 5.19, structured and unstructured mesh with 250 and 288 bilinear finite elements, respectively are adopted to investigate the mesh dependency of the results. The penalty parameter for the interface is set to $k_n = 10^6\,\mathrm{N/mm^3}$.

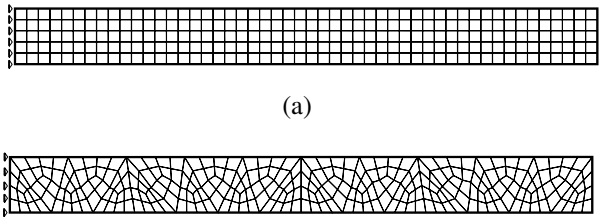

(a)

(b)

Figure 5.19: Representation of adopted meshes for peel test: (a) structured mesh (b) unstructured mesh.

As represented in Figure 5.20, the load *versus* displacement response of the structure for standard XFEM and polygonal enrichments demonstrate that the proposed formulation has a perfect agreement with the results of the previous study (Remmers et al., 2001). Since the formulation of standard XFEM faces serious difficulties in analysing this test using unstructured mesh, the inaccurate results of standard XFEM formulation are removed. Consequently, this approach can be considered as a mesh-independent and reliable alternative to standard XFEM.

The traction profile for different penalty parameters during the peak load and the last softening stages in vertical displacement $u_y = 0.4\,\mathrm{mm}$ and $u_y = 4\,\mathrm{mm}$ (see – Figure 5.21) indicate the robustness of the proposed formulation, leading no oscillation in traction profile even for the penalties greater than $10^8\,\mathrm{N/mm^3}$, which is studied previously (Dias-da-Costa et al., 2010; Rots, 1988; Simone, 2004). As a consequence, the proposed formulation may be appropriate

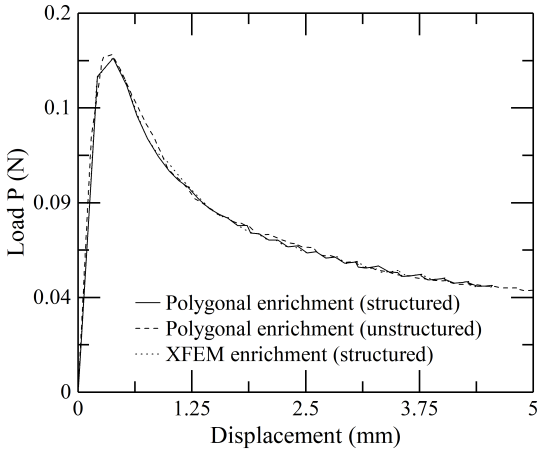

Figure 5.20: Peel test: load *versus* vertical displacement curves for different formulations.

and accurate option to be utilised for interface problems that need perfect bound between two surfaces, which is simulated utilising the high value of interface stiffness.

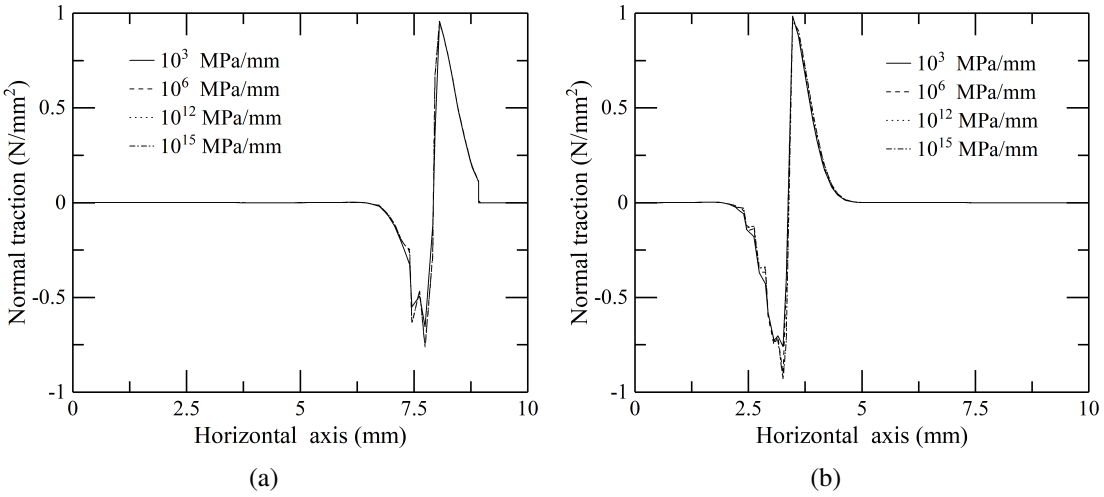

Figure 5.21: Peel test: traction profile of unstructured mesh for different penalty parameters in vertical displacement (a) $u_y = 0.4\,\text{mm}$ and (b) $u_y = 4\,\text{mm}$.

The stress maps for polygonal and standard XFEM enrichments are represented in Figure 5.22, which reveal that the proposed formulation has a good agreement with standard XFEM and accurately captures the stress field around the crack tip during the softening.

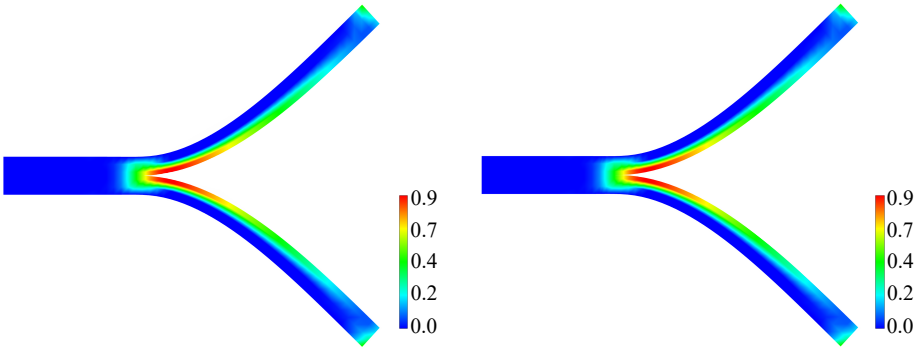

(a) (b)

Figure 5.22: Peel test: stress map of (a) polygonal enrichment and (b) standard XFEM enrichment in $u_y = 4\,\text{mm}$.

5.4.4 Four-point shear test

Four-point shear beam tested by Arrea (1982) is simulated in this section to investigate the effect of proposed formulation on a structural example treated the mixed-mode problem.

The specimen geometry, boundary conditions and the mesh adopted are depicted in Figure 5.23. Since compressive strength, f_c, the Young's modulus, E, and the Poisson's ratio, ν are the only parameters measured in (Arrea, 1982), the previous studies consider significantly different values for the corresponding parameters, including cohesive zone parameters can only be assessed experimentally (Arrea, 1982; Cendón et al., 2000). Consequently, the constitutive parameters utilised in this study are assumed: the Young's modulus $E = 24800\,\text{N/mm}^2$; Poisson ratio $\nu = 0.18$; tensile strength $f_t = 3.8\,\text{N/mm}^2$; and fracture energy $G_F = 0.125\,\text{N/mm}$.

The traction-separation law introduced by Alfaiate et al. (2002) in section 2.2.2 is adopted to treat the mixed-mode fracture in four-point shear test. To this end, $\beta = 0.7$, the normal and shear stiffness is considered $k_n = k_s = 10^5\,\text{N/mm}^3$ for discontinuity closure.

The mesh adopted is discretised by 1236 quadrilateral finite elements (see – Figure 5.23). The arc-length method is utilised to enforce the monotonic increase of Crack Mouth Sliding Displacement (CMSD).

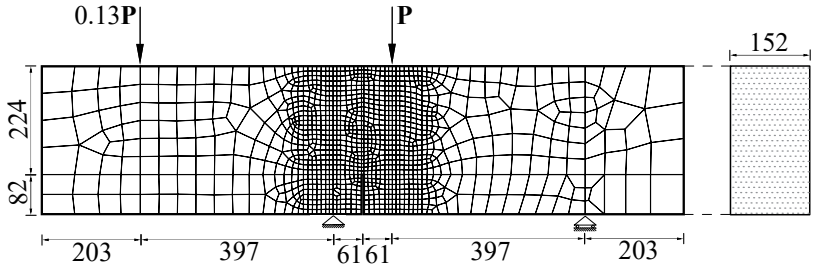

Figure 5.23: Four-point shear test: geometry and mesh.

The CMSD *versus* load curves for standard XFEM and the developed formulation are represented in Figure 5.24 and compared with experimental results. The obtained results indicate that the difference between the two formulation lies in the post-peak part of the loading. Although the difference is not significant, the polygonal enrichment presents better agreement with experimental results.

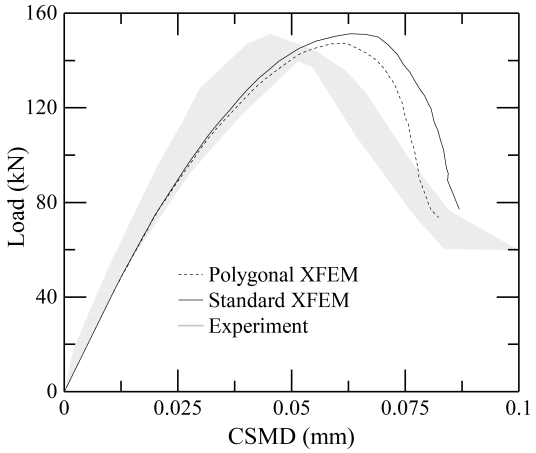

Figure 5.24: Four-point shear test: Comparison of polygonal enrichment with standard XFEM and experimental results.

The deformed structure and the corresponding stress maps depicted in Figure 5.25 for different stages of loading show the accuracy of the proposed formulation without any difficulties at the crack tip.

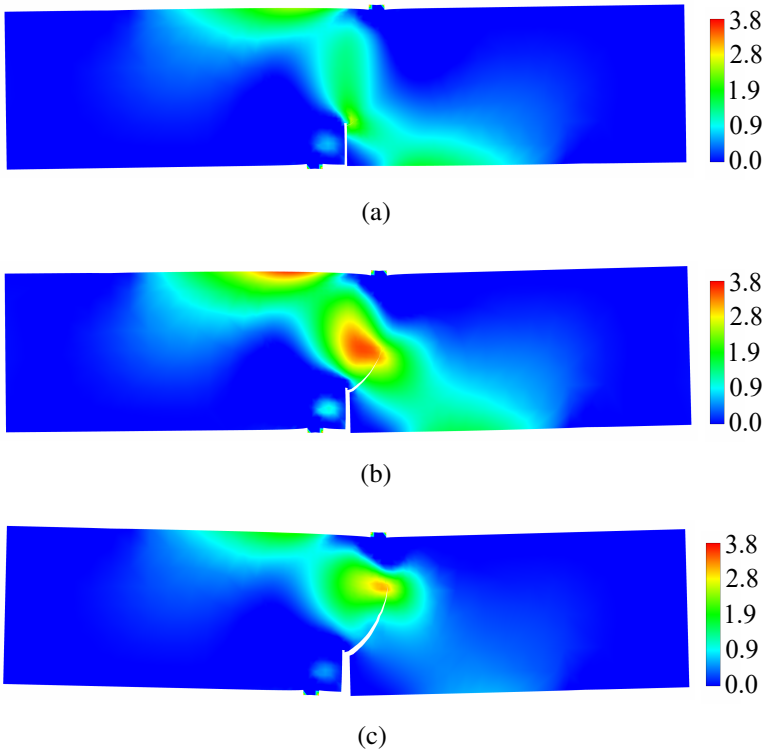

Figure 5.25: Four-point shear test: stress map of polygonal enrichment for: (a) CMSD = 0.025 mm; (b) CMSD = 0.07 mm; and (c) CMSD = 0.085 mm.

5.5 Conclusions

This chapter presented a new formulation utilising polygonal interpolants for XFEM enrichment. This formulation results in resolving the XFEM difficulties caused by using quadrilateral finite elements, including spurious oscillation in traction between two faces of a discontinuity, and fictitious displacement jump at the interface. The robustness and accuracy of the formulation were assessed using both element and structural examples in terms of

force-displacement response, traction profile along with the discontinuity, and displacement jump (crack opening).

In contrast to the conventional remedies (e.g. mesh refinement, using nodal integration) of the anomalous oscillatory behaviour, the proposed formulation is capable of overcoming it without loss of generality regarding discontinuity propagation path in terms of the parent element natural co-ordinates.

Eventually, the new formulation gives physical meaning to the degrees of freedom used for calculating the opening of the discontinuity in XFEM. As a consequence, the enrichment by polygonal interpolant enables XFEM to be utilised for the penalty stiffness above $10^8\,\mathrm{N/mm^3}$, leading to the remarkable ability to treat boundary conditions directly at the discontinuity such as moisture, temperature or the injection of epoxy resin for crack repair.

CHAPTER 6

Conclusions

In this work, different aspects of crack propagation modelling in quasi-brittle materials are improved. The contributions made to the research field can be divided into three parts as follows.

The discrete crack approaches use two constitutive models to analyse the fracture process: one for the discontinuity and another for the bulk (i.e. continuum part). The bulk can be handled as linear elastic, with the non-linear behaviour being lumped in the discontinuity. With such an approach, the constitutive model of the bulk cannot provide information about strain localisation, which is required to capture the process of crack localisation and propagation. The first drawback can be overcome by a crack initiation criterion. The adequate determination of the path of the discontinuity, traced by propagation criterion, should be considered as the second most important term used to analyse the fracture process, which considerably influences nodal values.

In conventional approaches, the Rankine failure surface is a widely-used criterion, where a discontinuity is initiated when the principal stress reaches the tensile strength of the material and is propagated aligned with the normal to maximum principal stress plane. In a recent study, different surfaces are proposed and compared for crack propagation to clarify the

advantages and disadvantages for the problem at hand. As a new contribution of this study to the discrete crack approach, it can be mentioned more reliable cracking criteria for the full range of traction space (i.e. tensile and compressive states) without the need of any predefined consideration to be given manually to identify strain localisation and trace the discontinuity orientation.

XFEM is one of the most popular frameworks that can be used to treat the problems involving strong discontinuities. Even though this formulation can benefit from the crack-tracking strategies analysed, other intrinsic issues can compromise the accuracy of the analysis. For instance, the additional degrees of freedom used in XFEM to enrich the nodes whose supports cut by a discontinuity, rapidly increase while crack propagates across the specimen. These additional degrees of freedom are considered as global unknowns to guarantee the continuity of the traction and the displacement jump fields across element boundaries. This justification, however rational, also increases the computational effort required to solve the system of equations. In this thesis, a formulation using a novel multi-layered Heaviside enrichment strategy is proposed. These independent multi-layers covering additional degrees of freedom lead the associated enrichments to be condensed out of the system of equations, whose size and conditioning are significantly improved. Eventually, without special treatment, the new formulation enables piece-wise continuous displacement jumps across element boundaries, even where a crack cuts a corner.

Among various elements used in the finite element method, the class of elements treating the problems involving discontinuity, called PU-based discontinuous element, causes several computational issues such as spurious displacement jump (i.e., crack opening) and fictitious

oscillation in traction profile transferring between two discontinuity faces. These inaccuracies have a severe effect on nodal values obtained by solving the system of equations to the analysis failure in some cases. Despite several casual treatments suggested in previous studies, no robust approach to solve these issues has been introduced in the literature. As a contribution to the research field, a new formulation is proposed in this work to overcome those difficulties. This formulation employs the attribute of XFEM, in which the interpolation functions used for the second layer of degrees of freedom can be picked arbitrarily if those functions satisfy the partition of unity. Accordingly, the polygonal interpolant is utilised for the proposed formulation in lieu of polynomial shape functions conventionally used in XFEM. As a result, the novel enrichment method resolves the difficulties caused by using the shape functions that cannot interpolate the traction or/and displacement jump fields appropriately.

6.1 Main Conclusions

A new robust numerical approach has been developed to model the propagation of strong discontinuities using a partition of unity-based approach. Three new improvements have been presented: *i*) the modified failure surfaces, which are utilised as new cracking criteria managing crack initiation and propagation processes in discrete crack approaches; *ii*) an efficient formulation for XFEM using novel multi-layered Heaviside enrichment strategy to reduce the degrees of freedom in global stiffness matrix and improve the conditioning of the system of equations; and *iii*) a novel formulation utilising appropriate interpolants for the second layer of degrees of freedom in XFEM to overcome the computational difficulties, namely spurious displacement jump and oscillation in traction profile.

The comparison between cracking criteria indicates that Alfaiate's failure surface in terms of crack initiation and propagation can be considered as the most accurate cracking surface in different stress states (Alfaiate and De, 2004). The curved shape of the failure surface causes some difficulties in implementation; however, it guarantees a smooth transition between tensile and compressive states and different range of shear stresses.

The multi-layered Heaviside enrichment formulation may be interpreted as an efficient formulation for standard XFEM. This formulation reduces the bandwidth of the global stiffness matrix and condition number of the equation systems. In contrast to embedded approaches showing non-conformity of approximated fields at the element level, the proposed formulation offers piece-wise continuous displacement jumps across element boundaries.

The polygonal enrichment formulation replaces the interpolant conventionally used in XFEM. The advantages gained by the interpolation function replacement overcome several computational issues. The new formulation improves the applicability of the XFEM to problems which may require specific boundary conditions to be introduced at the discontinuity (e.g. moisture and temperature). The new formulation removes the fictitious oscillation in traction profiles caused by pathological coupling between degrees of freedom.

Several important conclusions are drawn from the numerical examples given in each chapter, namely:

- Chapter 3 - Crack propagation criterion

- In mode-I failure, the similarity found among results obtained from different cracking criteria allows concluding that the Rankine criterion can be utilised as the most straightforward criterion to implement and use for these type of problems.
- For mixed-mode failure, the reliability of the Rankine criterion depends on the problem being analysed, which could fail to trace the crack path and consequent load *versus* displacement response of the structure.
- The averaged effective stress criterion shows the inconsistency of results. The significant sensitivity of this approach to predefined parameters and mesh sensitivity, questions the reliability of the criterion. Accordingly, despite good results in some cases, the criterion is not recommended for the discrete crack approach.
- In contrast to the Rankine criterion, the modified cracking surfaces (i.e. Alfaiate's and Carol's failure surfaces) represent good performance to capture the peak load and softening stage during mixed-mode failure.
- The lack of a compressive cap in the Rankine cracking surface and an incompatibility with the discrete constitutive model prevent this criterion from reliably predicting crack initiation and propagation in mixed-mode fracture.
- The modified cracking surfaces provide nearly coincident results for all traction states except for uniaxial compression, where Alfaiate's cracking surface shows robust and accurate performance. Consequently, this method can be considered overall the most robust one to predict both initiation and propagation for quasi-brittle materials in different traction states.

• Chapter 4 - multi-layered XFEM approach

- In the multi-layered XFEM formulation, the enrichment layers containing more than a single element resolve the deficiency of non-conforming crack opening from internal fictitious deformation modes fully preventing the non-physical rotation of corners of elements cut by the discontinuity. This is achieved without the need to eliminate any deformation mode such as linear jumps, which is one of the shortcomings of embedded strong discontinuity approaches.
- In contrast to standard XFEM, the condition number of the proposed formulation remains nearly constant with respect to the interface stiffness. Consequently, a considerable advantage of the new formulation is associated with the static condensation of the enhanced degrees of freedom, allowing the condition number to remain close to the one obtained for the non-cracked mesh.
- Regardless of the size of the active length, the noticeable oscillation in the traction profile caused by the discretisation with the smaller active length tends to vanish at the last stages of the analysis. This reveals that the multi-layer enrichment can provide good results almost independently of the selected size of the domain, even when there can be a layer with just one element in certain cases.

• Chapter 5 - Polygonal enrichment functions

- In contrast to standard XFEM, integration on Ω^- is not necessary for polygonal enrichment formulation, leading to easier implementation and decrease in computational effort.
- In PU-based discontinuous finite elements, the pathological coupling between degrees of freedom can be eliminated using the polygonal enrichment formulation.

Consequently, the displacement jump (crack opening) obtained using the proposed formulation indicates excellent agreement with analytical solutions.

– One of the main shortcomings of standard XFEM, the serious spurious oscillation in the traction profile that becomes worst for higher values of interface stiffness, is automatically resolved utilising the proposed formulation, even when high interface stiffnesses are adopted (i.e. penalty parameters in the order of $10^{20}\,\mathrm{N/mm^3}$).
– The boundary condition cannot influence the accuracy of the results of traction profile and displacement jump obtained from polygonal enrichment formulation, whose robustness is approved analysing several interface problems.
– The conventional assumption that PU-based discontinuous elements require nodal integration schemes (e.g. Newton-Cotes/Lobatto) to provide a satisfactory traction profile and crack opening improves the presented formulation significantly compared to standard XFEM.
– The polygonal enrichment formulation solves the severe difficulty of standard XFEM in modelling the problems with stiff discontinuities (e.g. cracks repaired with the injection of epoxy resin), and interface problems considering boundary condition on discontinuity (e.g. moisture uptake, temperature-dependent problems).

Eventually, it should be emphasised that the proposed formulations can select appropriate cracking criterion based on the problem at hand and improve the accuracy and versatility in analysing both crack propagation and interface problems using PU-based approaches, specially XFEM. In contrast to standard XFEM, the polygonal enrichment formulation allows the discontinuities to be defined explicitly, leading to the strong physical meaning of the additional

degrees of freedom. This attribute, in addition to the accuracy of obtained displacement jump, makes this formulation especially suitable for specific problems where boundary conditions can be introduced/specified directly at the discontinuity, such as temperature-dependent problems or the injection of epoxy resin for crack repairing. On the other hand, only integrating on Ω^+ in polygonal enrichment formulation and employing multi-layered Heaviside enrichment formulation reduce the computational costs in two different ways.

6.2 Suggestions for future developments

The discrete crack models have been mostly exclusively applied to situations of pure or close-to-pure tensile cracking. An investigation of the possibilities of extending the models for dealing with the compressive state is suggested for future development. As a result, the appropriate cracking criteria for compression state could be further assessed to analyse the post-peak behaviour of the specimens subjected to compressive loading.

Furthermore, the polygonal enrichment formulation can be employed in various interface problems, namely: delamination of composite materials, bond-slip behaviour of reinforced concrete, pull-out tests, and even more complex phenomena such as the effect of moisture and temperature on the behaviour of reinforced concrete structures, and alkali-silica reaction effect on steel-concrete bond behaviour.

The formulations developed herein are implemented for two-dimensional problems exclusively, including plane stress. For further development, three-dimensional modelling can be

considered for both polygonal enrichment formulation and multi-layered Heaviside enrichment. It should be emphasised that the multi-layered Heaviside strategy can be even more effective in decreasing the global stiffness matrix bandwidth and consequent computational cost for three-dimensional problems than two-dimensional modelling.

This page was intentionally left blank

APPENDIX A

Polygonal Finite Element

In contrast with conventional finite element method using polynomials as interpolants, Wachspress (1971) introduced a concept to generate the unconventional shape functions on *convex* $n-gons$. Later, these interpolants were revised (Belikov et al., 1997; Moorthy and Ghosh, 2000; Rashid and Gullett, 2000; Sukumar and Malsch, 2006; Tiwary et al., 2007) and Laplace interpolation (Hiyoshi and Sugihara, 1999), as a natural neighbor-based interpolation scheme, which is capable to be utilised easily in finite element method framework was developed. Since Laplace interpolants are utilised in this thesis, a brief summary about the Wachspress interpolants as the conventional polygonal interpolants and the patch tests need to be satisfied by shape functions used in the finite element are given herein.

A1 Wachspress interpolants

Wachspress (1971) proved that the shape function on $n-gons$ are rational polynomials, which are given by:

$$N_i^n(x,y) = \frac{\mathscr{P}^{n-2}(x,y)}{\mathscr{P}^{n-3}(x,y)} \tag{A.1}$$

where $\mathscr{P}^{(m)}(x,y)$ is a polynomial of degree m.

A simpler expression for Wachspress interpolants is proposed by Meyer et al. (2002) as:

$$\varphi_i^w(\mathbf{x}) = \frac{w_i(\mathbf{x})}{\sum_{j=1}^{n} w_j(\mathbf{x})} \tag{A.2}$$

where:

$$w_i(\mathbf{x}) = \frac{A(p_{i-1}, p, p_{i+1})}{A(p_{i-1}, p_i, p)A(p_i, p_{i+1}, p)} = \frac{\cot\gamma_i + \cot\delta_i}{\|x - x_i\|^2} \tag{A.3}$$

where $A(a,b,c)$ denotes the signed area of triangle $[a,b,c]$, while γ_i and δ_i are depicted in Figure A.1.

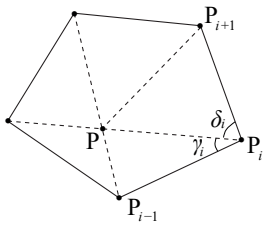

Figure A.1: Wachspress shape functions on a pentagon.

Note that, $\varphi_i^w(\mathbf{x})$ is non-negative and the polygon must be convex ($\gamma_i + \delta_i < 0$). In addition, instead of calculation of the angles γ_i and δ_i explicitly, the cotangents are computed by vector cross and dot product formulae. Considering (a_1,a_2), (b_1,b_2) and (c_1,c_2) are the vertices coordinates of the triangle $[p_i, p_{i+1}, p]$, the $\cot\delta_i$ reads as:

$$\cot\delta_i = \frac{(P_{i+1} - P_i).(P - P_i)}{|(P_{i+1} - P_i) \times (P - P_i)|} = \frac{(b_1 - a_1)(c_1 - a_1) + (b_2 - a_2)(c_2 - a_2)}{(b_1 - a_1)(c_2 - a_2) - (b_2 - a_2)(c_1 - a_1)} \equiv \frac{C}{S} \tag{A.4}$$

and its derivatives can be calculated by:

$$\frac{\partial(\cot\delta_i)}{\partial c_1} = \frac{(b_1 - a_1) - \cot\delta_i(a_2 - b_2)}{S} \tag{A.5a}$$

$$\frac{\partial(\cot\delta_i)}{\partial c_2} = \frac{(b_2 - a_2) - \cot\delta_i(b_1 - a_1)}{S} \tag{A.5b}$$

Similarly the $\cot\gamma_i$ can be computed. It is noteworthy that the Wachspress shape functions provide all conditions discussed in section A2 on polygons by means of the lowest-order shape functions (Warren et al., 2007).

A2 Interpolant patch tests

The shape functions of the polygonal finite element need to satisfy all the patch testes of conventional shape functions in finite elements. Consider a polygonal body Ω with boundary $\partial\Omega$. The body is described by n nodes, which are labelled p_i and located at the coordinate $\mathbf{x}_i \equiv (x_i, y_i) \in \bar{\Omega}$, while $\bar{\Omega} = \Omega \cup \partial\Omega$, as depicted in Figure A.2. A set of shape functions $\phi_i(\mathbf{x})$ for point p can interpolate the scalar-value function $u(\mathbf{x})$ as below:

$$u(\mathbf{x}) = \sum_{i=1}^{n} \phi_i(\mathbf{x}) u_i, \tag{A.6}$$

where u_i denotes the unknowns at the neighbors of the point p. Accordingly, the following patch tests should be satisfied by the interpolant:

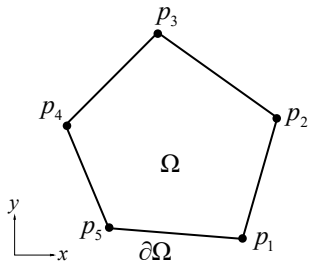

Figure A.2: Polygonal domain.

1- $\phi_i(\mathbf{x})$ should form a partition of unity, be non-negative and bounded:

$$\sum_{i=1}^{n} \phi_i(\mathbf{x}) = 1, \quad 0 \leq \phi_i(\mathbf{x}) \leq 1. \tag{A.7}$$

2- The nodal value should be identical to the value interpolated at a node:

$$\phi_i(\mathbf{x}_j) = \delta_{ij} \tag{A.8}$$

where δ_{ij} is the Kronecker-delta.

3- Since constant and linear completeness of the trial function satisfies convergence condition in Galerkin method for second-order partial differential equations, interpolant needs to satisfy linear completeness (Hughes, 2012):

$$\sum_{i=1}^{n} \phi_i(\mathbf{x})\mathbf{x}_i = \mathbf{x}. \tag{A.9}$$

References

Agathos, Konstantinos et al. (2016). 'A well-conditioned and optimally convergent XFEM for 3D linear elastic fracture'. *International Journal for Numerical Methods in Engineering* 105.9, pp. 643–677.

Ahmed, A and LJ Sluys (2013). 'Anomalous behavior of bilinear quadrilateral finite elements for modeling cohesive cracks with XFEM/GFEM'. *International journal for numerical methods in engineering* 94.5, pp. 454–472.

Alfaiate, J and Almeida JR De (2004). 'Modelling discrete cracking on masonry walls'. *Masonry International* 17.2, pp. 83–93.

Alfaiate, J, EB Pires and JAC Martins (1997). 'A finite element analysis of non-prescribed crack propagation in concrete'. *Computers & Structures* 63.1, pp. 17–26.

Alfaiate, J, A Simone and LJ Sluys (2003). 'Non-homogeneous displacement jumps in strong embedded discontinuities'. *International Journal of Solids and Structures* 40.21, pp. 5799–5817.

Alfaiate, J, GN Wells and LJ Sluys (2002). 'On the use of embedded discontinuity elements with crack path continuity for mode-I and mixed-mode fracture'. *Engineering fracture mechanics* 69.6, pp. 661–686.

Alfano, GaMAC and M_A Crisfield (2001). 'Finite element interface models for the delamination analysis of laminated composites: mechanical and computational issues'. *International journal for numerical methods in engineering* 50.7, pp. 1701–1736.

Aquino, W et al. (2009). 'Generalized finite element method using proper orthogonal decomposition'. *International journal for numerical methods in engineering* 79.7, pp. 887–906.

Aragón, Alejandro M and Angelo Simone (2017). 'The discontinuity-enriched finite element method'. *International Journal for Numerical Methods in Engineering* 112.11, pp. 1589–1613.

Areias, P et al. (2009). 'Arbitrary bi-dimensional finite strain cohesive crack propagation'. *Computational Mechanics* 45.1, pp. 61–75.

Armero, Francisco and Krishna Garikipati (1996). 'An analysis of strong discontinuities in multiplicative finite strain plasticity and their relation with the numerical simulation of strain localization in solids'. *International Journal of Solids and Structures* 33.20-22, pp. 2863–2885.

Arrea, M (1982). 'Mixed-mode craok propagation in mortar and concrete'. *Report No. 81-13, Department of Structural Engineering*.

Arrea, Manrique (1981). 'Mixed-mode crack propagation in mortar and concrete'. *Dept. of Struct. Engrg. Rep.*, pp. 81–13.

Babuška, Ivo and Uday Banerjee (2012). 'Stable generalized finite element method (SGFEM)'. *Computer methods in applied mechanics and engineering* 201, pp. 91–111.

Babuška, Ivo and Jens M Melenk (1997). 'The partition of unity method'. *International journal for numerical methods in engineering* 40.4, pp. 727–758.

Barenblatt, Grigory I (1959). 'The formation of equilibrium cracks during brittle fracture. General ideas and hypotheses. Axially-symmetric cracks'. *Journal of Applied Mathematics and Mechanics* 23.3, pp. 622–636.

Barpi, F and S Valente (2000). 'Numerical simulation of prenotched gravity dam models'. *Journal of Engineering Mechanics* 126.6, pp. 611–619.

Bazant, Zdenek P, Phillip A Pfeiffer et al. (1987). 'Determination of fracture energy from size effect and brittleness number'. *ACI Materials Journal* 84.6, pp. 463–480.

Bazant, Zdenek P and Jaime Planas (1997). *Fracture and size effect in concrete and other quasibrittle materials*. Vol. 16. CRC press.

Béchet, Éric et al. (2005). 'Improved implementation and robustness study of the X-FEM for stress analysis around cracks'. *International Journal for Numerical Methods in Engineering* 64.8, pp. 1033–1056.

Belikov, VV et al. (1997). 'The non-Sibsonian interpolation: a new method of interpolation of the values of a function on an arbitrary set of points'. *Computational mathematics and mathematical physics* 37.1, pp. 9–15.

Belytschko, T, D Organ and C Gerlach (2000). 'Element-free Galerkin methods for dynamic fracture in concrete'. *Computer Methods in Applied Mechanics and Engineering* 187.3-4, pp. 385–399.

Belytschko, Ted and Tom Black (1999). 'Elastic crack growth in finite elements with minimal remeshing'. *International journal for numerical methods in engineering* 45.5, pp. 601–620.

Belytschko, Ted, Yun Yun Lu and Lei Gu (1994). 'Element-free Galerkin methods'. *International journal for numerical methods in engineering* 37.2, pp. 229–256.

Belytschko, Ted, YY Lu and L Gu (1995). 'Crack propagation by element-free Galerkin methods'. *Engineering Fracture Mechanics* 51.2, pp. 295–315.

Belytschko, Ted et al. (2001). 'Arbitrary discontinuities in finite elements'. *International Journal for Numerical Methods in Engineering* 50.4, pp. 993–1013.

Belytschko, Ted et al. (2003). 'Dynamic crack propagation based on loss of hyperbolicity and a new discontinuous enrichment'. *International journal for numerical methods in engineering* 58.12, pp. 1873–1905.

Belytschko, Ted et al. (2013). *Nonlinear finite elements for continua and structures*. John wiley & sons.

Bittencourt, TN et al. (1996). 'Quasi-automatic simulation of crack propagation for 2D LEFM problems'. *Engineering Fracture Mechanics* 55.2, pp. 321–334.

Bolzon, G (2001). 'Formulation of a triangular finite element with an embedded interface via isoparametric mapping'. *Computational Mechanics* 27.6, pp. 463–473.

Borst, R de et al. (1993). 'Fundamental issues in finite element analyses of localization of deformation'. *Engineering Computations: Int J for Computer-Aided Engineering* 10.2, pp. 99–121.

Borst, Rene de et al. (2004). 'Discrete vs smeared crack models for concrete fracture: bridging the gap'. *International journal for numerical and analytical methods in geomechanics* 28.7-8, pp. 583–607.

Camacho, Godofredo T and M Ortiz (1996). 'Computational modelling of impact damage in brittle materials'. *International Journal of solids and structures* 33.20-22, pp. 2899–2938.

Carol, Ignacio, Pere C Prat and Carlos M Lopez (1997). 'Normal/shear cracking model: application to discrete crack analysis'. *Journal of engineering mechanics* 123.8, pp. 765–773.

Cendón, DA et al. (2000). 'Modelling the fracture of concrete under mixed loading'. *International Journal of Fracture* 103.3, pp. 293–310.

Cervenka, Vladimir (1985). 'Constitutive model for cracked reinforced concrete'. In: *Journal Proceedings*. Vol. 82. 6, pp. 877–882.

Cervera, M and M Chiumenti (2006). 'Smeared crack approach: back to the original track'. *International Journal for Numerical and Analytical Methods in Geomechanics* 30.12, pp. 1173–1199.

Cervera, Miguel and Jian-Ying Wu (2015). 'On the conformity of strong, regularized, embedded and smeared discontinuity approaches for the modeling of localized failure in solids'. *International Journal of Solids and Structures* 71, pp. 19–38.

Chen, L et al. (2012). 'Extended finite element method with edge-based strain smoothing (ESm-XFEM) for linear elastic crack growth'. *Computer Methods in Applied Mechanics and Engineering* 209, pp. 250–265.

Christ, NH, R Friedberg and TD Lee (1982). 'Weights of links and plaquettes in a random lattice'. *Nuclear Physics B* 210.3, pp. 337–346.

Cornelissen, H, D Hordijk and H Reinhardt (1986). 'Experimental determination of crack softening characteristics of normalweight and lightweight'. *Heron* 31.2, pp. 45–46.

Coutinho, ALGA et al. (2003). 'Simple zero thickness kinematically consistent interface elements'. *Computers and Geotechnics* 30.5, pp. 347–374.

Csati, Zoltan, Nicolas Moës and Thierry J Massart (2020). 'A stable extended/generalized finite element method with Lagrange multipliers and explicit damage update for distributed cracking in cohesive materials'. *Computer Methods in Applied Mechanics and Engineering* 369, p. 113173.

Day, RA and DM Potts (1994). 'Zero thickness interface elements—numerical stability and application'. *International Journal for numerical and analytical methods in geomechanics* 18.10, pp. 689–708.

De Borst, R and P Nauta (1985). 'Non-orthogonal cracks in a smeared finite element model'. *Engineering Computations* 2.3, pp. 35–46.

Dias-da-Costa, D, V Cervenka and R Graça-e-Costa (2018). 'Model uncertainty in discrete and smeared crack prediction in RC beams under flexural loads'. *Engineering Fracture Mechanics* 199, pp. 532–543.

Dias-da-Costa, D et al. (2009). 'A discrete strong discontinuity approach'. *Engineering Fracture Mechanics* 76.9, pp. 1176–1201.

Dias-da-Costa, D et al. (2010). 'A comparative study on the modelling of discontinuous fracture by means of enriched nodal and element techniques and interface elements'. *International Journal of Fracture* 161.1, p. 97.

Duarte, C Armando, Ivo Babuska and J Tinsley Oden (2000). 'Generalized finite element methods for three-dimensional structural mechanics problems'. *Computers & Structures* 77.2, pp. 215–232.

Duarte, C Armando and D-J Kim (2008). 'Analysis and applications of a generalized finite element method with global–local enrichment functions'. *Computer Methods in Applied Mechanics and Engineering* 197.6-8, pp. 487–504.

Duarte, C Armando and J Tinsley Oden (1996a). 'An hp adaptive method using clouds'. *Computer methods in applied mechanics and engineering* 139.1-4, pp. 237–262.

Duarte, C Armando and J Tinsley Oden (1996b). 'H-p clouds—an h-p meshless method'. *Numerical Methods for Partial Differential Equations: An International Journal* 12.6, pp. 673–705.

Dugdale, Donald S (1960). 'Yielding of steel sheets containing slits'. *Journal of the Mechanics and Physics of Solids* 8.2, pp. 100–104.

Dvorkin, Eduardo N, Alberto M Cuitiño and Gustavo Gioia (1990). 'Finite elements with displacement interpolated embedded localization lines insensitive to mesh size and distortions'. *International journal for numerical methods in engineering* 30.3, pp. 541–564.

Fix, George J, Sandeep Gulati and GI Wakoff (1973). 'On the use of singular functions with finite element approximations'. *Journal of Computational Physics* 13.2, pp. 209–228.

Fries, Thomas-Peter (2008). 'A corrected XFEM approximation without problems in blending elements'. *International Journal for Numerical Methods in Engineering* 75.5, pp. 503–532.

Fries, Thomas-Peter and Ted Belytschko (2006). 'The intrinsic XFEM: a method for arbitrary discontinuities without additional unknowns'. *International journal for numerical methods in engineering* 68.13, pp. 1358–1385.

Fries, Thomas-Peter and Ted Belytschko (2010). 'The extended/generalized finite element method: an overview of the method and its applications'. *International journal for numerical methods in engineering* 84.3, pp. 253–304.

Gálvez, JC et al. (1998). 'Mixed mode fracture of concrete under proportional and nonproportional loading'. *International Journal of Fracture* 94.3, pp. 267–284.

Gálvez, JC et al. (2002). 'A discrete crack approach to normal/shear cracking of concrete'. *Cement and concrete research* 32.10, pp. 1567–1585.

Gasser, Thomas C and Gerhard A Holzapfel (2006). '3d crack propagation in unreinforced concrete.: A two-step algorithm for tracking 3d crack paths'. *Computer Methods in Applied Mechanics and Engineering* 195.37-40, pp. 5198–5219.

Gentle, James E (2007). 'Matrix algebra'. *Springer texts in statistics, Springer, New York, NY, doi* 10, pp. 978–.

Goodman, Richard E, Robert L Taylor and Tor L Brekke (1968). 'A model for the mechanics of jointed rock'. *Journal of Soil Mechanics & Foundations Div*.

Gopalaratnam, VS and Surendra P Shah (1985). 'Softening response of plain concrete in direct tension'. In: *Journal Proceedings*. Vol. 82. 3, pp. 310–323.

Griffith, Alan Arnold (1921). 'VI. The phenomena of rupture and flow in solids'. *Philosophical transactions of the royal society of london. Series A, containing papers of a mathematical or physical character* 221.582-593, pp. 163–198.

Gupta, Ajaya K and Habibollah Akbar (1984). 'Cracking in reinforced concrete analysis'. *Journal of Structural Engineering* 110.8, pp. 1735–1746.

Hillerborg, Arne, Mats Modéer and P-E Petersson (1976). 'Analysis of crack formation and crack growth in concrete by means of fracture mechanics and finite elements'. *Cement and concrete research* 6.6, pp. 773–781.

Hiyoshi, Hisamoto and Kokichi Sugihara (1999). 'Two generalizations of an interpolant based on Voronoi diagrams'. *International journal of shape modeling* 5.02, pp. 219–231.

Hughes, Thomas JR (2012). *The finite element method: linear static and dynamic finite element analysis*. Courier Corporation.

Ingraffea, Anthony R and Victor Saouma (1985). 'Numerical modeling of discrete crack propagation in reinforced and plain concrete'. In: *Fracture mechanics of concrete: structural application and numerical calculation*. Springer, pp. 171–225.

Ingraffea, Anthony R et al. (1984). 'Fracture mechanics of bond in reinforced concrete'. *Journal of Structural Engineering* 110.4, pp. 871–890.

Irwin, George R (1997). 'Analysis of stresses and strains near the end of a crack traversing a plate'.

Jendele, L et al. (2001). 'On the choice between discrete or smeared approach in practical structural FE analyses of concrete structures'. In: *Fourth International Conference on Analysis of Discontinuous Deformation Glasgow, Scotland UK*.

Jin, Tao et al. (2019). 'Three-dimensional explicit finite element formulation for shear localization with global tracking of embedded weak discontinuities'. *Computer Methods in Applied Mechanics and Engineering* 353, pp. 416–447.

Jirásek, Milan and Ted Belytschko (2002). 'Computational resolution of strong discontinuities'. In: *Proceedings of fifth world congress on computational mechanics, WCCM V, Vienna University of Technology, Austria*.

Jirásek, Milan and Thomas Zimmermann (2001). 'Embedded crack model. Part II: Combination with smeared cracks'. *International Journal for Numerical Methods in Engineering* 50.6, pp. 1291–1305.

John, Reji and Surendra P. Shah (1990). 'Mixed-Mode Fracture of Concrete Subjected to Impact Loading'. *Journal of Structural Engineering* 116.3, pp. 585–602.

Kaliakin, VN and J Li (1995). 'Insight into deficiencies associated with commonly used zero-thickness interface elements'. *Computers and Geotechnics* 17.2, pp. 225–252.

Keer, Leon M, J Dundurs and K Kiattikomol (1973). 'Separation of a smooth circular inclusion from a matrix'. *International Journal of Engineering Science* 11.11, pp. 1221–1233.

Khoei, Amir R (2014). *Extended finite element method: theory and applications*. John Wiley & Sons.

Kikuchi, Noboru and John Tinsley Oden (1988). *Contact problems in elasticity: a study of variational inequalities and finite element methods*. SIAM.

Kim, D-J, JP Pereira and CA Duarte (2010). 'Analysis of three-dimensional fracture mechanics problems: A two-scale approach using coarse-generalized FEM meshes'. *International journal for numerical methods in engineering* 81.3, pp. 335–365.

Klisinski, Marek, Kenneth Runesson and Stein Sture (1991). 'Finite element with inner softening band'. *Journal of engineering mechanics* 117.3, pp. 575–587.

Kraus, JK (2006). 'Algebraic multilevel preconditioning of finite element matrices using local Schur complements'. *Numerical linear algebra with applications* 13.1, pp. 49–70.

Larsson, Ragnar and Kenneth Runesson (1996). 'Element-embedded localization band based on regularized displacement discontinuity'. *Journal of Engineering Mechanics* 122.5, pp. 402–411.

Lertsrisakulrat, Torsak et al. (2001). 'Experimental study on parameters in localization of concrete subjected to compression'. *Doboku Gakkai Ronbunshu* 2001.669, pp. 309–321.

Linder, C. and F. Armero (2007a). 'Finite elements with embedded strong discontinuities for the modeling of failure in solids'. *International Journal for Numerical Methods in Engineering* 72.12. doi: 10.1002/nme.2042, pp. 1391–1433.

Linder, Christian and Francisco Armero (2007b). 'Finite elements with embedded strong discontinuities for the modeling of failure in solids'. *International Journal for Numerical Methods in Engineering* 72.12, pp. 1391–1433.

Liu, Wing Kam, Sukky Jun and Yi Fei Zhang (1995). 'Reproducing kernel particle methods'. *International journal for numerical methods in fluids* 20.8-9, pp. 1081–1106.

Loehnert, Stefan (2014). 'A stabilization technique for the regularization of nearly singular extended finite elements'. *Computational Mechanics* 54.2, pp. 523–533.

Lofti, HR and PB Shing (1994). 'Analysis of concrete fracture with an embedded crack approach'. *Computational Modelling of Concrete Structures, Pineridge, Swansea*, pp. 343–352.

Lotfi, Hamid R and P Benson Shing (1995). 'Embedded representation of fracture in concrete with mixed finite elements'. *International journal for numerical methods in engineering* 38.8, pp. 1307–1325.

Lucy, Leon B (1977). 'A numerical approach to the testing of the fission hypothesis'. *The astronomical journal* 82, pp. 1013–1024.

Ma, Fashang et al. (1999). 'A CTOD-based mixed-mode fracture criterion'. In: *Mixed-mode crack behavior*. ASTM International.

Malvern, Lawrence E (1969). *Introduction to the Mechanics of a Continuous Medium*. Monograph.

Manzoli, OL and PB Shing (2006). 'A general technique to embed non-uniform discontinuities into standard solid finite elements'. *Computers & Structures* 84.10-11, pp. 742–757.

Mariani, Stefano and Umberto Perego (2003). 'Extended finite element method for quasi-brittle fracture'. *International Journal for Numerical Methods in Engineering* 58.1, pp. 103–126.

Melenk, Jens M and Ivo Babuška (1996). 'The partition of unity finite element method: basic theory and applications'. In: *Research Report/Seminar für Angewandte Mathematik*. Vol. 1996. 01. Eidgenössische Technische Hochschule, Seminar für Angewandte Mathematik.

Menk, Alexander and Stéphane PA Bordas (2011). 'A robust preconditioning technique for the extended finite element method'. *International Journal for Numerical Methods in Engineering* 85.13, pp. 1609–1632.

Mergheim, J (2009). 'A variational multiscale method to model crack propagation at finite strains'. *International journal for numerical methods in engineering* 80.3, pp. 269–289.

Meschke, Gunther and Peter Dumstorff (2007). 'Energy-based modeling of cohesive and cohesionless cracks via X-FEM'. *Computer methods in applied mechanics and engineering* 196.21-24, pp. 2338–2357.

Meyer, Mark et al. (2002). 'Generalized barycentric coordinates on irregular polygons'. *Journal of graphics tools* 7.1, pp. 13–22.

Moës, Nicolas, John Dolbow and Ted Belytschko (1999). 'A finite element method for crack growth without remeshing'. *International journal for numerical methods in engineering* 46.1, pp. 131–150.

Moorthy, Suresh and Somnath Ghosh (2000). 'Adaptivity and convergence in the Voronoi cell finite element model for analyzing heterogeneous materials'. *Computer Methods in Applied Mechanics and Engineering* 185.1, pp. 37–74.

Mousavi, SE, H Xiao and N26543611183 Sukumar (2010). 'Generalized Gaussian quadrature rules on arbitrary polygons'. *International Journal for Numerical Methods in Engineering* 82.1, pp. 99–113.

Natarajan, Sundararajan, Stéphane Bordas and D Roy Mahapatra (2009). 'Numerical integration over arbitrary polygonal domains based on Schwarz–Christoffel conformal mapping'. *International Journal for Numerical Methods in Engineering* 80.1, pp. 103–134.

Ngo, D_ and Alex C Scordelis (1967). 'Finite element analysis of reinforced concrete beams'. In: *Journal Proceedings*. Vol. 64. 3, pp. 152–163.

Nguyen, Vinh Phu et al. (2008). 'Meshless methods: a review and computer implementation aspects'. *Mathematics and computers in simulation* 79.3, pp. 763–813.

Nikolić, Mijo et al. (2018). 'Crack propagation in dynamics by embedded strong discontinuity approach: Enhanced solid versus discrete lattice model'. *Computer Methods in Applied Mechanics and Engineering* 340, pp. 480–499.

Nooru, MB-Mohamed (1992). 'Mixed-mode fracture of concrete: an experimental approach'. PhD thesis. Delft University of Technology.

Oden, J Tinsley, CAM Duarte and Olek C Zienkiewicz (1998). 'A new cloud-based hp finite element method'. *Computer methods in applied mechanics and engineering* 153.1-2, pp. 117–126.

Ohlsson, Ulf and Thomas Olofsson (1997). 'Mixed-mode fracture and anchor bolts in concrete analysis with inner softening bands'. *Journal of engineering mechanics* 123.10, pp. 1027–1033.

Oliver, J. et al. (2004). 'Continuum approach to the numerical simulation of material failure in concrete'. *International Journal for Numerical and Analytical Methods in Geomechanics* 28.7-8, pp. 609–632.

Oliver, Javier (1996). 'Modelling strong discontinuities in solid mechanics via strain softening constitutive equations. Part 1: Fundamentals'. *International journal for numerical methods in engineering* 39.21, pp. 3575–3600.

Oliver, Javier, IF Dias and Alfredo Edmundo Huespe (2014). 'Crack-path field and strain-injection techniques in computational modeling of propagating material failure'. *Computer Methods in Applied Mechanics and Engineering* 274, pp. 289–348.

Oliver, Javier, AE Huespe and Esteban Samaniego (2003). 'A study on finite elements for capturing strong discontinuities'. *International journal for numerical methods in engineering* 56.14, pp. 2135–2161.

Oliver, Javier, Alfredo Edmundo Huespe and IF Dias (2012). 'Strain localization, strong discontinuities and material fracture: Matches and mismatches'. *Computer Methods in Applied Mechanics and Engineering* 241, pp. 323–336.

Ortiz, M and JJ Quigley Iv (1991). 'Adaptive mesh refinement in strain localization problems'. *Computer Methods in Applied Mechanics and Engineering* 90.1-3, pp. 781–804.

Ortiz, Michael, Yves Leroy and Alan Needleman (1987). 'A finite element method for localized failure analysis'. *Computer methods in applied mechanics and engineering* 61.2, pp. 189–214.

Park, Kyoungsoo et al. (2009). 'Integration of singular enrichment functions in the generalized/extended finite element method for three-dimensional problems'. *International Journal for Numerical Methods in Engineering* 78.10, pp. 1220–1257.

Pereira, JPA, D-J Kim and Carlos Armando Duarte (2012). 'A two-scale approach for the analysis of propagating three-dimensional fractures'. *Computational Mechanics* 49.1, pp. 99–121.

Pin, Tong and Theodore HH Pian (1973). 'On the convergence of the finite element method for problems with singularity'. *International Journal of solids and Structures* 9.3, pp. 313–321.

Pivonka, Peter et al. (2004). 'Comparative studies of 3D-constitutive models for concrete: application to mixed-mode fracture'. *International journal for numerical methods in engineering* 60.2, pp. 549–570.

Pommier, Sylvie et al. (2011). *Extended finite element method for crack propagation*. Wiley Online Library.

Pourmodheji, R and M Mashayekhi (2012). 'Improvement of the extended finite element method for ductile crack growth'. *Materials Science and Engineering: A* 551, pp. 255–271.

Rabczuk, Timon, PMA Areias and T Belytschko (2007a). 'A meshfree thin shell method for non-linear dynamic fracture'. *International journal for numerical methods in engineering* 72.5, pp. 524–548.

Rabczuk, Timon, PMA Areias and Ted Belytschko (2007b). 'A simplified mesh-free method for shear bands with cohesive surfaces'. *International Journal for Numerical Methods in Engineering* 69.5, pp. 993–1021.

Rabczuk, Timon and T Belytschko (2004). 'Cracking particles: a simplified meshfree method for arbitrary evolving cracks'. *International Journal for Numerical Methods in Engineering* 61.13, pp. 2316–2343.

Rabczuk, Timon et al. (2019). *Extended finite element and meshfree methods*. Academic Press.

Raina, Arun and Christian Linder (2015). 'A micromechanical model with strong discontinuities for failure in nonwovens at finite deformations'. *International Journal of Solids and Structures* 75, pp. 247–259.

Rashid, MM and PM Gullett (2000). 'On a finite element method with variable element topology'. *Computer Methods in Applied Mechanics and Engineering* 190.11-12, pp. 1509–1527.

Rashid, YR (1968). 'Ultimate strength analysis of prestressed concrete pressure vessels'. *Nuclear engineering and design* 7.4, pp. 334–344.

Remmers, Joris JC, Rene de Borst and Alan Needleman (2003). 'A cohesive segments method for the simulation of crack growth'. *Computational mechanics* 31.1-2, pp. 69–77.

Remmers, Joris JC, René de Borst and Alan Needleman (2008). 'The simulation of dynamic crack propagation using the cohesive segments method'. *Journal of the Mechanics and Physics of Solids* 56.1, pp. 70–92.

Remmers, Joris JC, Garth Wells and René De Borst (2001). 'Analysis of delamination growth with discontinuous finite elements'.

Rots, Jan Gerrit (1988). 'Computational modeling of concrete fracture'.

Rots, Jan G et al. (1985). 'Smeared crack approach and fracture localization in concrete'. *HERON, 30 (1), 1985*.

Saloustros, Savvas, Luca Pelà and Miguel Cervera (2015). 'A crack-tracking technique for localized cohesive–frictional damage'. *Engineering Fracture Mechanics* 150, pp. 96–114.

Saouma, VE, E Bruhwiler and HL Boggs (1990). 'A review of fracture mechanics applied to concrete dams'. *Dam Engineering* 1.1, pp. 41–57.

Schellekens, JCJ and René De Borst (1993). 'On the numerical integration of interface elements'. *International Journal for Numerical Methods in Engineering* 36.1, pp. 43–66.

Schlangen, H.E.J.G. (1993). 'Experimental and numerical analysis of fracture processes in concrete'. PhD thesis. Delft University of Technology.

Siavelis, Maximilien et al. (2013). 'Large sliding contact along branched discontinuities with X-FEM'. *Computational mechanics* 52.1, pp. 201–219.

Sibson, Robin (1980). 'A vector identity for the Dirichlet tessellation'. In: *Mathematical Proceedings of the Cambridge Philosophical Society*. Vol. 87. 1. Cambridge University Press, pp. 151–155.

Simo, JUAN CARLOS, JAVIER Oliver and Francisco Armero (1993). 'An analysis of strong discontinuities induced by strain-softening in rate-independent inelastic solids'. *Computational mechanics* 12.5, pp. 277–296.

Simone, A (2004). 'Partition of unity-based discontinuous elements for interface phenomena: computational issues'. *Communications in Numerical Methods in Engineering* 20.6, pp. 465–478.

Simone, Angelo, Garth N Wells and Lambertus J Sluys (2003). 'From continuous to discontinuous failure in a gradient-enhanced continuum damage model'. *Computer Methods in Applied Mechanics and Engineering* 192.41-42, pp. 4581–4607.

Sluys, LJ and AH Berends (1998). 'Discontinuous failure analysis for mode-I and mode-II localization problems'. *International Journal of Solids and Structures* 35.31-32, pp. 4257–4274.

Soghrati, Soheil and Bowen Liang (2016). 'Automated analysis of microstructural effects on the failure response of heterogeneous adhesives'. *International Journal of Solids and Structures* 81, pp. 250–261.

Strang, Gilbert and George J Fix (1973). 'An analysis of the finite element method'.

Strouboulis, Theofanis, Ivo Babuška and Kevin Copps (2000). 'The design and analysis of the generalized finite element method'. *Computer methods in applied mechanics and engineering* 181.1-3, pp. 43–69.

Sukumar, N and EA Malsch (2006). 'Recent advances in the construction of polygonal finite element interpolants'. *Archives of Computational Methods in Engineering* 13.1, p. 129.

Sukumar, Natarajan and Alireza Tabarraei (2004). 'Conforming polygonal finite elements'. *International Journal for Numerical Methods in Engineering* 61.12, pp. 2045–2066.

Surendran, M et al. (2017). 'Linear smoothed extended finite element method'. *International Journal for Numerical Methods in Engineering* 112.12, pp. 1733–1749.

Tiwary, Abhijeet, Chao Hu and Somnath Ghosh (2007). 'Numerical conformal mapping method based Voronoi cell finite element model for analyzing microstructures with irregular heterogeneities'. *Finite elements in analysis and design* 43.6-7, pp. 504–520.

Van Geel, Erik (1998). *Concrete behaviour in multiaxial compression: experimental research*. Technische Universiteit Eindhoven, Faculteit Bouwkunde Eindhoven.

Ventura, Giulio (2006). 'On the elimination of quadrature subcells for discontinuous functions in the extended finite-element method'. *International Journal for Numerical Methods in Engineering* 66.5, pp. 761–795.

Wachspress, Eugene L (1971). 'A rational basis for function approximation'. In: *Conference on Applications of Numerical Analysis*. Springer, pp. 223–252.

Wang, EZ and NG Shrive (1995). 'Brittle fracture in compression: mechanisms, models and criteria'. *Engineering fracture mechanics* 52.6, pp. 1107–1126.

Warren, Joe et al. (2007). 'Barycentric coordinates for convex sets'. *Advances in computational mathematics* 27.3, pp. 319–338.

Washizu, Kyuichiro (1975). *Variational methods in elasticity and plasticity*. Vol. 3. Pergamon press Oxford.

Wells, Garth N, Lambertus J Sluys and René de Borst (2002). 'Simulating the propagation of displacement discontinuities in a regularized strain-softening medium'. *International Journal for Numerical Methods in Engineering* 53.5, pp. 1235–1256.

Wells, Garth N and LJ Sluys (2001a). 'A new method for modelling cohesive cracks using finite elements'. *International Journal for Numerical Methods in Engineering* 50.12, pp. 2667–2682.

Wells, GN and LJ Sluys (2001b). 'Analysis of slip planes in three-dimensional solids'. *Computer Methods in Applied Mechanics and Engineering* 190.28, pp. 3591–3606.

Wells, GN and LJ Sluys (2001c). 'Three-dimensional embedded discontinuity model for brittle fracture'. *International Journal of Solids and Structures* 38.5, pp. 897–913.

Winkler, Bernhard Josef (2001). *Traglastuntersuchungen von unbewehrten und bewehrten Betonstrukturen auf der Grundlage eines objektiven Werkstoffgesetzes für Beton*. Innsbruck University Press.

Wu, S and S Fang (2009). 'Modeling cohesive cracks with meshless method'. *International journal of damage mechanics* 18.8, pp. 721–737.

Yazid, Abdelaziz, Nabbou Abdelkader and Hamouine Abdelmadjid (2009). 'A state-of-the-art review of the X-FEM for computational fracture mechanics'. *Applied Mathematical Modelling* 33.12, pp. 4269–4282.

Zhang, Yiming et al. (2020). 'On the crack opening and energy dissipation in a continuum based disconnected crack model'. *Finite Elements in Analysis and Design* 170, p. 103333.

Zhu, Qi-Zhi (2012). 'On enrichment functions in the extended finite element method'. *International journal for numerical methods in engineering* 91.2, pp. 186–217.

Zi, Goangseup and Ted Belytschko (2003). 'New crack-tip elements for XFEM and applications to cohesive cracks'. *International Journal for Numerical Methods in Engineering* 57.15, pp. 2221–2240.